To the Graduate Council:

I am submitting herewith a thesis written by John H. Respess entitled "Edge-defined, Film-fed Growth: A Process Evaluation." I recommend that it be accepted in partial fulfillment of the requirements for the degree of Master of Science, with a major in Metallurgical Engineering.

Ben F. Oliver, Major Professor

We have read this thesis
and recommend its acceptance:

Accepted for the Council:

Vice Chancellor
Graduate Studies and Research

EDGE-DEFINED, FILM-FED GROWTH: A PROCESS EVALUATION

A Thesis

Presented for the

Master of Science

Degree

The University of Tennessee, Knoxville

John H. Respess

August 1976

1288040

ACKNOWLEDGMENTS

The author would like to express his sincere thanks and appreciation to Dr. B. F. Oliver who has guided this research program and who obtained the author's appointment as a Graduate Assistant at The University of Tennessee. In addition to guiding the author through a program of studies providing an excellent and varied education in metallurgical engineering, Dr. Oliver has allowed the author the luxury of freedom in making his own mistakes and overcoming his own problems.

A large amount of time was utilized in design and construction of the experimental equipment. The author's thanks are extended to the staff of the Chemical and Metallurgical Engineering machine shop and especially to Mr. H. B. Thompson and Mr. Robert Love for their tremendous assistance.

The author would like to thank Mr. T. A. Long and Mr. A. J. Beal of the Chemical and Metallurgical Engineering electronics shop. Their aid in providing precision controls and instrumentation for the experimental equipment proved invaluable in carrying out the work involved in this project.

Finally, the author would like to thank Mr. J. D. Holder and Dr. Cabel-Finch of ORNL for their generous donation of

material and information which was essential for the completion of this work.

ABSTRACT

The Edge-defined, Film-fed Growth (EFG) process is a relatively new solidification process which shows considerable promise in producing shaped materials directly from the melt. In order to utilize it to the maximum, it is necessary to explore the limits of the process controlling parameters. The following areas were explored in an effort to locate and characterize some of the important process parameters.

1. Materials exhibiting various types of solidification modes were grown via EFG to study the effect of faceting and nonfaceting behavior. V_2O_5, a faceting material, and LiF, a relatively nonfaceting material, were grown by the EFG process for this end.

2. The extent of shape producing capabilities of the process was explored by attempting to grow crystals in the form of thin ribbons, round tubes, square channels and airfoils. Dies of these configurations were constructed for this purpose.

3. A LiF/CaF_2 eutectic composition crystal was grown to study the growth interface characteristics and to explore the use of EFG in the production of aligned coupled eutectic materials.

4. Factors associated with EFG in general such as fluid flow, heat flow, wetting and spreading of the meniscus film

on the die, die temperature, growth velocities, etc., are discussed and pertinent observations made in these areas during the growth experiments are given.

It was found that faceted growth upon solidification can limit the spreading and edge definition of the growing crystal. Some orientations of facets show enhanced stability with respect to increasing growth velocities than do others.

The ability of the process to generate desired cross-sectional shapes appears excellent. Samples with flat surfaces, curved surfaces, inside and outside square corners, and hollow shapes were all successfully produced.

Aligned, coupled eutectic structures were obtained up to growth velocities of 10.00 cm/hr. Observations were made of lamellar to cellular transformations at the outer surface of the LiF/CaF_2 eutectic crystal grown. These areas of transformation occur at curved growth interfaces. Lamellar structure was unexpectedly found at the outer surface. Tentative mechanisms involving interfacial energies and fluid flow are proposed to explain the structure.

Control of the heat flow at the solid-liquid interface appears to be the most important process stability parameter in general.

TABLE OF CONTENTS

SECTION		PAGE
I.	INTRODUCTION	1
II.	THEORETICAL CONSIDERATIONS	14
	Fluid Statics	14
	Fluid Dynamics	19
	Heat Flow	31
	Meniscus Film Considerations	40
III.	EXPERIMENTAL SETUP	46
	Power Source and Controls	46
	The Containment Chamber	50
	The Support Structure	56
IV.	CRUCIBLE AND DIE DESIGNS	60
V.	WETTABILITY OBSERVATIONS	78
VI.	RESULTS	83
	V_2O_5 Ribbon Shaped Crystals	83
	LiF Shaped Crystals	96
	LiF/CaF_2 Airfoil Shaped Crystal	114
VII.	DISCUSSION OF RESULTS	141
LIST OF REFERENCES		145
VITA		149

LIST OF TABLES

TABLE		PAGE
I.	Summary of Crucible/Die/Melt Setups Utilized in Study	61
II.	Results of Wettability Experiments	82
III.	Some Physical and Thermodynamic Properties of V_2O_5	85
IV.	Correlation of the Denoted Regions of V_2O_5 Sample 108 Shown in Figure 40 with the Growth Velocities and Distances Grown in Those Sections	88
V.	Correlation of the Denoted Regions of V_2O_5 Sample 146 Shown in Figure 42 with the Growth Velocities and Distances Grown in Those Sections	92
VI.	Correlation of the Denoted Regions of V_2O_5 Sample 151 Shown in Figure 45 with the Growth Velocities and Distances Grown in Those Sections	95
VII.	Some Physical and Thermodynamic Properties of LiF	98
VIII.	Correlation of the Denoted Regions of LiF Tube Shaped Sample 182 Shown in Figure 46 with the Growth Velocities and Distances Grown in Those Sections	99
IX.	Correlation of the Denoted Regions of the LiF Tube Shaped Sample 204 Shown in Figure 49 with the Growth Velocities and Distances Grown in Those Sections	104
X.	Correlation of Denoted Regions of LiF Channel Shaped Sample 246 Shown in Figure 52 with the Growth Velocities and Distances Grown in Those Sections	109

TABLE PAGE

XI. Correlation of the Denoted Regions of LiF/CaF_2 Eutectic Sample 233 Shown in Figure 58 with the Growth Velocities and Distances Grown in Those Sections 118

XII. Correlation of Growth Velocity and Lamellar Spacing 124

XIII. Results of Width Measurements of Cellular and Lamellar Areas in Sample 233. 131

LIST OF FIGURES

FIGURE		PAGE
1.	Schematic Diagram of Floating Die Used in Growing Shaped Crystals by the Stepanov Method	3
2.	Sequence of Events, (a) to (c), Showing Seeding, Spreading and Growing of a Shaped Crystal by the EFG Process.	6
3.	Schematic Diagram of an EFG System and the Change of Shape of the Meniscus Film when the Crystal Is Moved Upwards a Distance Δz	7
4.	Representation of the Temperature Profile in the Die and Crystal During EFG	9
5.	Sequential Seeding and Spreading Operation which Takes Place in EFG	11
6.	Schematic Diagram of the Growth of a Shaped Crystal with a Hollow Cross Section by EFG . .	13
7.	Solid-Liquid-Vapor Intersection of a Liquid Drop Resting on a Solid Substrate	15
8.	Schematic Diagram of Liquid Rising in a Capillary.	17
9.	Schematic Diagram of a Crystal Growing Via the EFG Process.	18
10.	Fluid Flow in a Capillary Tube	21
11.	Fluid Flow in a Capillary Slit	24
12.	Fluid Flow in an Annular Capillary	26
13.	Fluid Flow in the Meniscus Film.	29
14.	Schematic Diagram of the Heat Flow Conditions During Edge-Defined, Film-Fed Growth of a Ribbon Shaped Crystal.	32
15.	Schematic Diagram of a Small Diameter Filament Crystal Growing by the EFG Process	39

FIGURE PAGE

16. Schematic Illustration of the Solid-Liquid-Vapor Interface of a Crystal Growing from the Melt . 44

17. The Complete EFG Crystal Growth System 47

18. The Containment Chamber Portion of the Crystal Growth Unit. 51

19. Schematic Diagram of the Containment Chamber . . 52

20. End of Draw Rod with Typical Seed Assembly Mounted in Place 54

21. View of the Crucible/Die Setup as Seen Through the Window in the Copper Cooling Jacket. . . . 55

22. Furnace Containing Copper Wool Which Was Used to Reduce the Oxygen Content in the Inert Atmosphere Tank Gases. 58

23. Schematic Diagram of Platinum Thin Ribbon Shape Die. 62

24. Schematic Diagram of Thin Ribbon Shape Die and Crucible Assembly. 64

25. Crucible/Die Setup of the Platinum Thin Ribbon Shape Die and Platinum Crucible. 65

26. Schematic Diagram of Nickel Circular Tube Shape Die. 67

27. Schematic Diagram of Nickel Crucible Used in Conjunction with the Nickel Tube Shape Die . . 68

28. Crucible/Die Setup of the Nickel Circular Tube Shape Die and Nickel Crucible. 69

29. Schematic Diagram of Nickel U-Shape Channel Die. 71

30. Crucible/Die Setup of Nickel U-Shape Die and Nickel Crucible. 72

31. Schematic Diagram of Nickel Airfoil Shape Die. . 74

32. Schematic Diagram of Nickel Crucible Used in Conjunction with the Nickel Airfoil Shape Die. 75

FIGURE PAGE

33. Crucible/Die Setup of the Nickel Airfoil Shape Die and Nickel Crucible. 76

34. Schematic Diagram of the Refractory Containers Used to House and Insulate the Crucible/Die Setups During the Growth Runs. 77

35. Schematic Diagram of Experimental Setup for Measuring Wetting Angles of Molten Fluorides in Nickel. 79

36. Molten LiF on Nickel Surface 79

37. Molten LiF/CaF_2 Droplets on Nickel Surface . . . 81

38. Molten $LiF/CaF_2/SrF_2$ Droplets on Nickel Surface. 81

39. Molten V_2O_5 on a Platinum Surface. 82

40. V_2O_5 Sample 108, Side View 87

41. V_2O_5 Sample 108, Edge View 87

42. V_2O_5 Sample 146, Side View A 91

43. V_2O_5 Sample 146, Side View B 91

44. Schematic Diagram of Faceted Surface of Crystal Growing Adjacent to Die Edge 93

45. V_2O_5 Sample 151, Side View 95

46. Lithium Fluoride Tube Shaped Sample 182. 99

47. Spreading of the Sample 182 Around the Circumference of the Tube Shape Die. 101

48. End Section of LiF Tube Shaped Sample 182 Showing Loss of Stability 103

49. LiF Tube Shaped Sample 204 103

50. Area of LiF Sample 204 Showing Massive Instability. 106

51. End Section of LiF Tube Shaped Sample 204 Showing Loss of Stability. 106

FIGURE		PAGE
52.	LiF Channel Shaped Sample 246, Full Length View.	108
53.	LiF Channel Shaped Sample 246, Perspective View.	108
54.	Loss of Stability at End Section of LiF Channel Shaped Sample 246.	111
55.	Schematic Diagram of Channel Shaped Sample Cross Section.	111
56.	Full Length View of LiF Channel Shaped Sample 256.	112
57.	Perspective View of LiF Channel Shaped Sample 256.	112
58.	Full Length Side View of LiF/CaF_2 Eutectic Sample 233	115
59.	Full Length Edge View of LiF/CaF_2 Eutectic Sample 233	115
60.	LiF/CaF_2 Eutectic Sample 233 Microstructure, Section B.	120
61.	LiF/CaF_2 Eutectic Sample 233 Microstructure, Section C.	121
62.	LiF/CaF_2 Eutectic Sample 233 Microstructure, Section D.	122
63.	LiF/CaF_2 Eutectic Sample 233 Microstructure, Section E.	123
64.	Longitudinal View of Section G Showing Growth Direction of Lamellae in Outer Band of Microstructure	125
65.	Longitudinal View of Section A/B Showing Shape of Solid-Liquid Interface Through Striations in the Microstructure.	126
66.	Schematic Diagram of a LiF/CaF_2 Eutectic Crystal Growing by EFG from an Airfoil Shape Die . . .	128
67.	Longitudinal View of Section B Showing Cellular Structure Existing at Curved Interface	130

FIGURE PAGE

68. Longitudinal View of Section A/B Showing Lamellar Structure at Flat Interface 130

69. Schematic Diagram of Solid-Liquid-Vapor Junction of a Crystal Growing from a Film Resting on a Die. 135

70. Microstructure of Sample 233 at Growth Velocity Change of 5.00 cm/hr to 10.00 cm/hr. 138

71. Lamella to Rod Transformation in Section B of Sample 233 139

I. INTRODUCTION

The production of materials in useful shapes and sizes has long been an area of great interest in metallurgy. It is desirable from the standpoint of present-day economic values to maximize the generation of such products with a minimum expenditure of energy, time and money. In accordance with these desires, there has for some time been considerable interest in the field of crystal growth and solidification in directly producing finished or nearly finished products from the melt. Past work in this area has shown that pulling shaped crystals from the melt offers, in some cases, advantages over more conventional production methods. In general these advantages are as follows:

1. Some materials because of their inherent mechanical properties do not lend themselves to being shaped by deformation forming processes (e.g., refractory oxides). Pulling such materials in desired shapes (e.g., tube, rod, sheet, etc.) directly from the melt offers a viable method for their production.

2. The total time and energy consumption in producing nearly finished products directly from the melt is less than that required to reach an equivalent stage of production in a casting/deformation forming/machining type operation.[1]

3. The pulling of shaped crystals directly from the melt lends itself well to being a continuous process[2] which is an economically advantageous mode of production.

4. Certain properties of the material pulled directly from the melt may be controlled by controlling the solid-liquid growth interface.

5. Only a small amount of the material involved in a continuous growth from the melt process ends up as scrap.

The study of growing shaped cyrstals directly from the melt is by no means a recent undertaking. E. von Gomperz[3] in 1921 succeeded in growing crystals through holes cut in a mica sheet which floated on top of the melt. The materials he worked with were all low melting point pure metals which when grown through holes cut in the mica sheet had cross-sectional shapes like those of the holes.

A. V. Stepanov[2] began his work on growing shaped crystals from the melt in 1938. In the Stepanov method a floating piece containing an outlet hole of some desired shape is partially immersed into the melt; see Figure 1. Liquid in the melt is forced into this outlet by the hydrostatic pressure difference of the liquid levels present in the crucible. A seed crystal is brought into contact with the liquid which has risen into the outlet opening. The temperature is controlled in such a manner that as the seed is drawn upwards, the liquid clinging to it by capillary

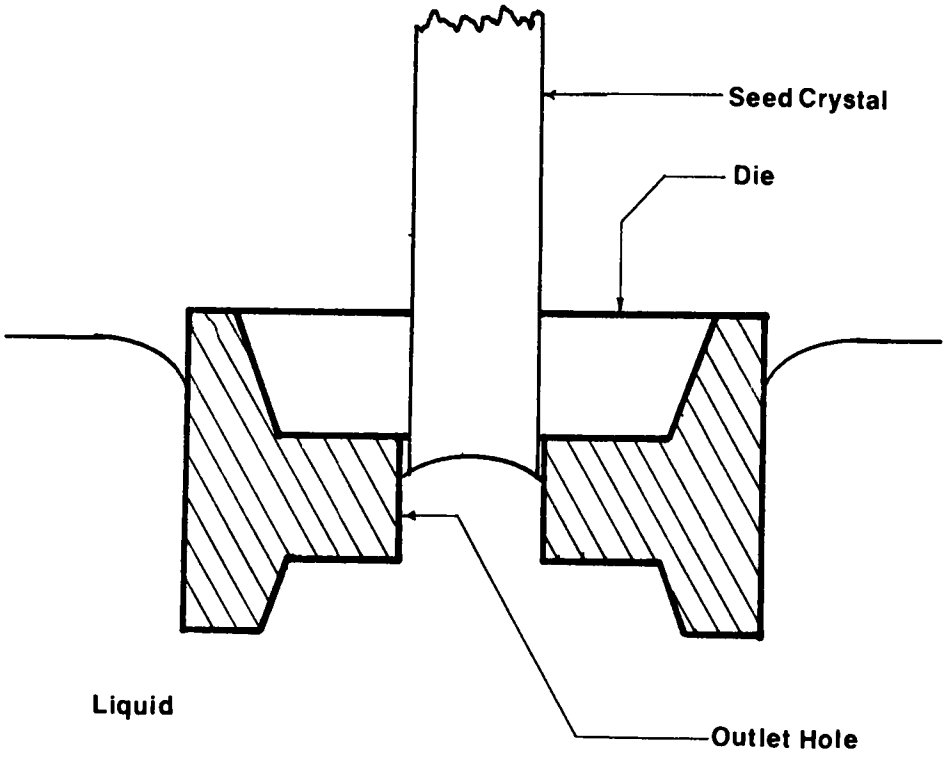


Figure 1. Schematic diagram of floating die used in growing shaped crystals by the Stepanov[2] method.

attraction is frozen as it is pulled above the level of the outlet opening. Subsequent liquid which feeds through the outlet freezes on that portion of the crystal already solidified. In this manner a crystal is grown which has a shape like that of the outlet hole. Quite complex shapes[4] have been grown by this method.

Brissot and Raynaud[5] have used a method almost identical to that of Stepanov to grow germanium single crystals in ribbon form. It was found that the crystallographic orientation of these germanium ribbons could be controlled by controlling the orientation of the seed crystal. Similar results were achieved around the same time by Tsivinski and Stepanov[6] who used the Stepanov method.

A method in which a crystal in sheet form is grown horizontally off of the melt surface has been described by Bleil.[7] Heat is removed from the growing crystal at right angles to the direction of growth by means of a heat sink. The thickness dimension of the ribbon is controlled by manipulating the rate of heat removal by the heat sink.

A process for growing Al_2O_3 crystals using a molybdenum die was first described by H. E. LaBelle, Jr., and A. I. Mlavsky[8] in 1971. This method utilizes a die equipped with a capillary hole and a melt which wets the die material. The die is first inserted into the melt surface, liquid rises up the capillary hole and is then induced by a seed crystal

to rise out of the capillary and spread across the top surface of the die; see Figure 2. The film located between the die and the crystal supplies the crystal with material for growth. The film itself is replenished by liquid feeding through the capillary as the crystal is pulled upwards. The shape of the crystal is determined by the outside edge of the die top surface. This process has been named, Edge-defined, Film-fed Growth (EFG) by H. E. LaBelle, Jr.[9]

It is the purpose of this investigation to provide a process evaluation of EFG. As a beginning point, a detailed disucssion of the overall process is now undertaken in the following.

Illustrated in Figure 3a is a system that consists of a vessel containing a reservoir of liquid, a vertically mounted capillary tube in the liquid, a thin film of liquid on the top surface of the capillary tube, and a crystal in contact with the top surface of the liquid film. A necessary condition for an operational system is that the liquid wet both the capillary die material and the crystal.[9] The pressure in the film is given by Laplace's equation,[10]

$$\Delta P = p_1 - p_2 = \gamma \left(\frac{1}{r_1} + \frac{1}{r_2}\right) \qquad (1)$$

where γ is the surface tension in dynes/cm^2, and r_1 and r_2 are the principal radii of curvature in cm. The film

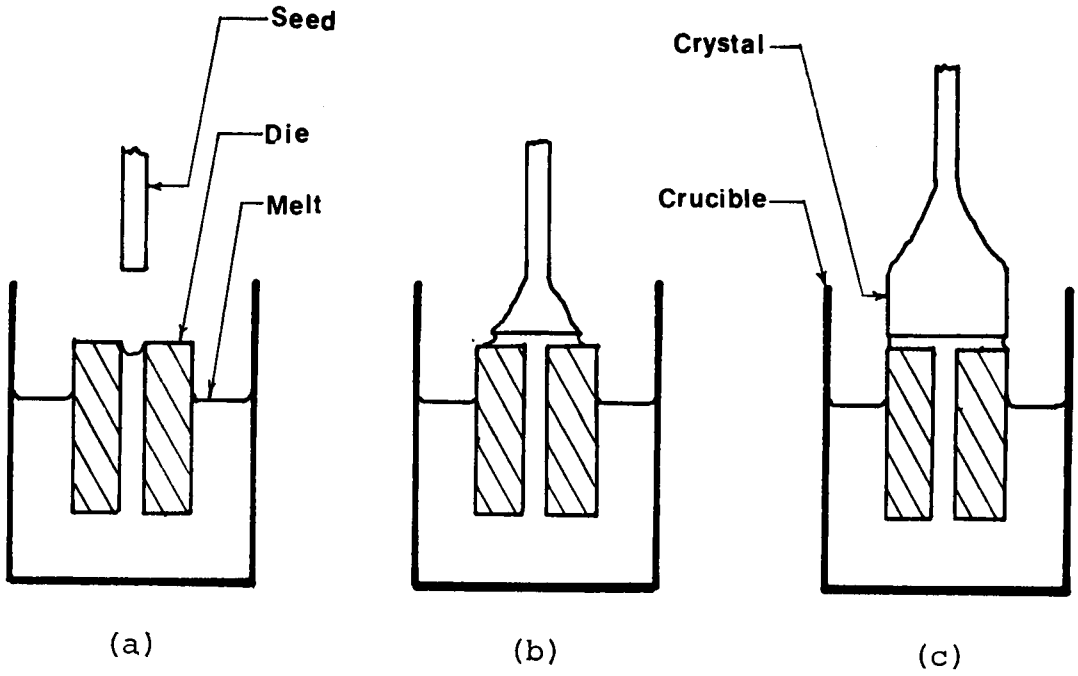
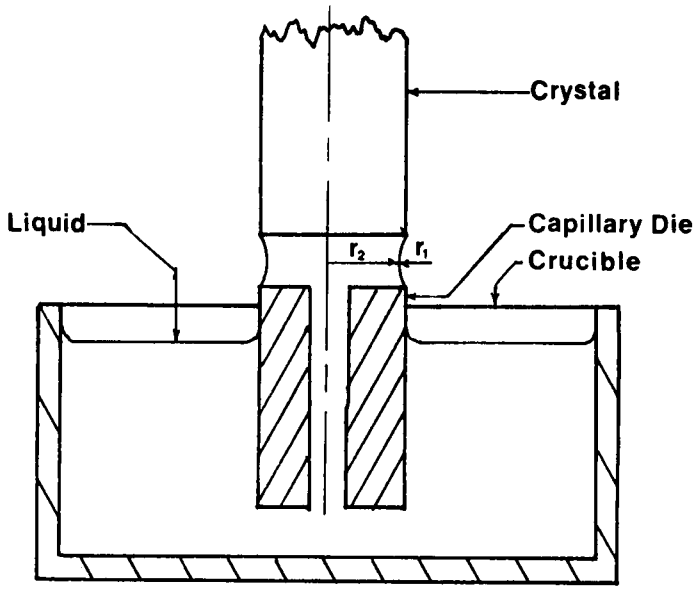
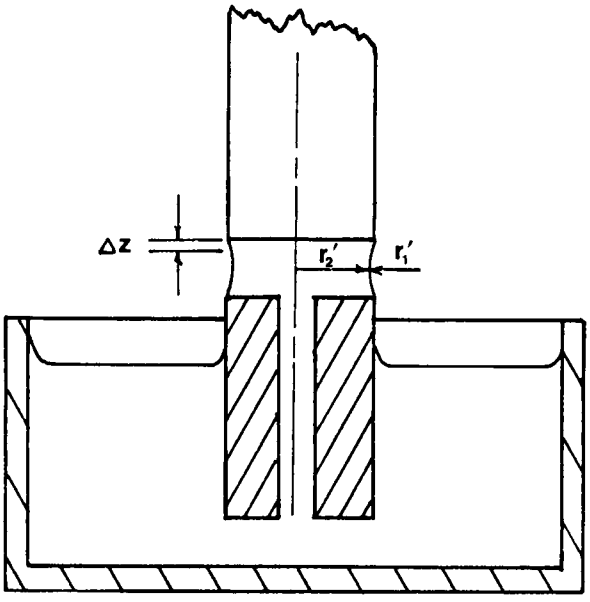


Figure 2. Sequence of events, (a) to (c), showing seeding, spreading and growing of a shaped crystal by the EFG process.



(a)



(b)

Figure 3. Schematic diagram of an EFG system and the change of shape of the meniscus film when the crystal is moved upwards a distance Δz.

pressure differs from the atmospheric pressure by the hydrostatic pressure head of the liquid in the capillary. If the crystal is moved upwards instantaneously, as in Figure 3b, by an amount Δz, the film dimensions change as a result of the conservation of mass.[9] Thus, r_1 becomes r_1', and r_2 becomes r_2', and the pressure in the film becomes

$$\Delta P' = p_1' - p_2' = \gamma\left(\frac{1}{r_1'} + \frac{1}{r_2'}\right) . \qquad (2)$$

This pressure is lower than the original pressure, ΔP. As a consequence, liquid is pulled up through the capillary into the film volume. Consider the system of a pure substance with a temperature profile such as that shown in Figure 4. Then as the crystal is moved upwards a distance Δz, reducing the pressure inside the film causing liquid to rise up the capillary into the film, the crystal grows downward an equal distance Δz back to the original interface position. If the constant velocity of the crystal upwards, V_p, equals the constant growth velocity, V_g, of the solid-liquid interface downwards, then a steady-state growth condition exists. Crystal growth into the meniscus film over the die is possible at steady-state once $V_g = V_p$. This assumes that the other factors effecting changes in V_g and V_p, such as heat flow, fluid motion, and wetting angles, are at steady-state values.

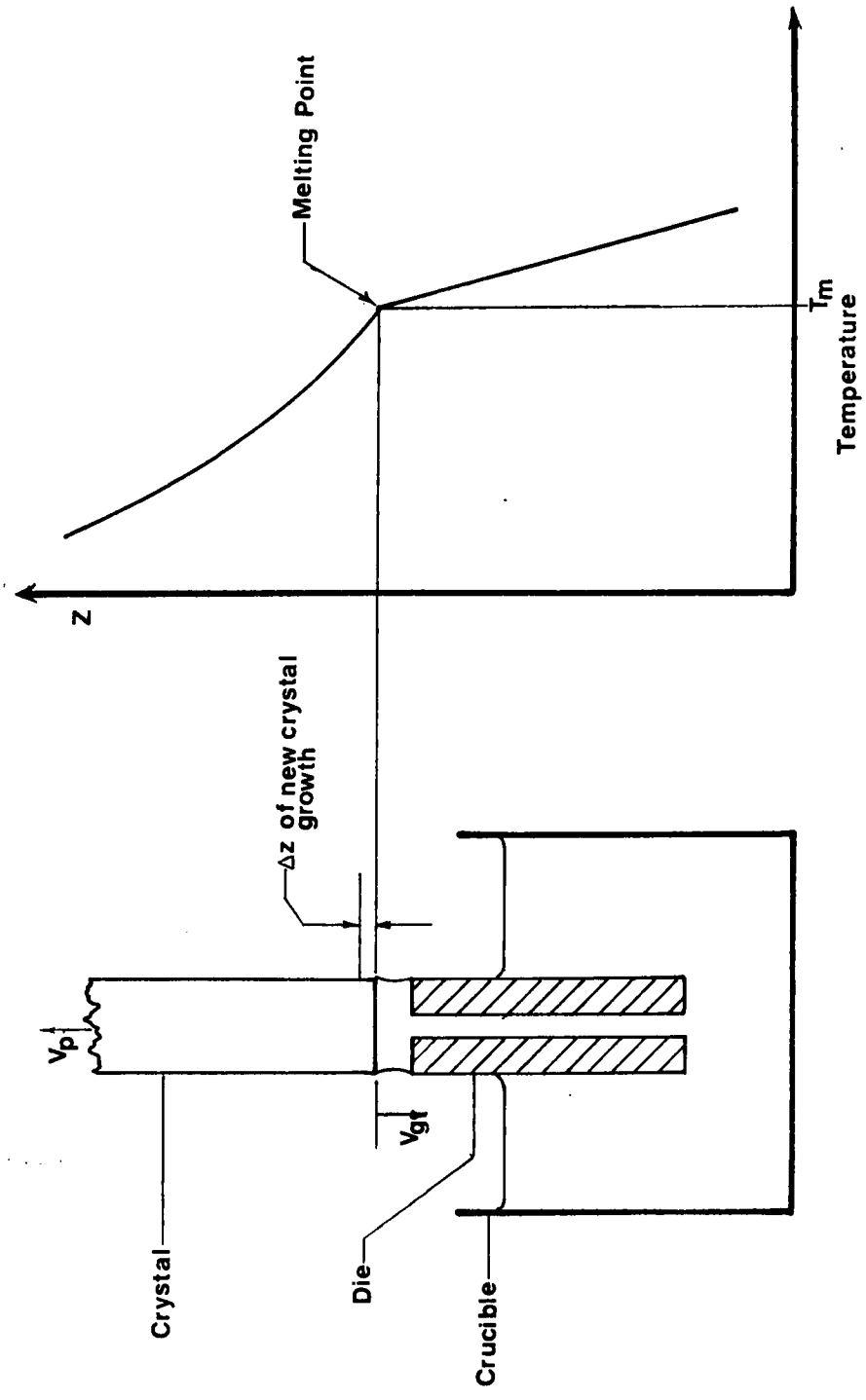


Figure 4. Representation of the temperature profile in the die and crystal during EFG.

The situation shown in Figure 3, page 7, is arrived at by a seeding and spreading operation[9] as shown sequentially in Figure 5. First, a seed is brought into contact with the liquid at the top of the capillary. The temperature is controlled such that liquid freezes to the seed, and the seed is slowly withdrawn pulling liquid out onto the die surface over which the liquid spreads. As the crystal advances upward, the film is constantly replenished by liquid flowing up the capillary and moves further across the top surface of the die as more of the liquid in the film becomes solid crystal. This increases the amount of top surface covered by solid crystal above the die. The liquid continues to spread until the edge of the die top surface is reached where the liquid stops. Hence, the cross-sectional shape of the growing crystal is now determined by the outer edge of the capillary piece. The capillary cross-sectional shape determines the crystal shape, and thus the capillary acts as a die to the growing crystal. Because the crystal growth process described utilizes the edge of the capillary die to define the cross-sectional shape of the growing crystal, and the crystal actually grows into a thin, continuously maintained film of liquid, it has been termed Edge-defined, Film-fed Growth.

Since the liquid film does not differentiate between the outside and the inside edges of a die surface, a blank

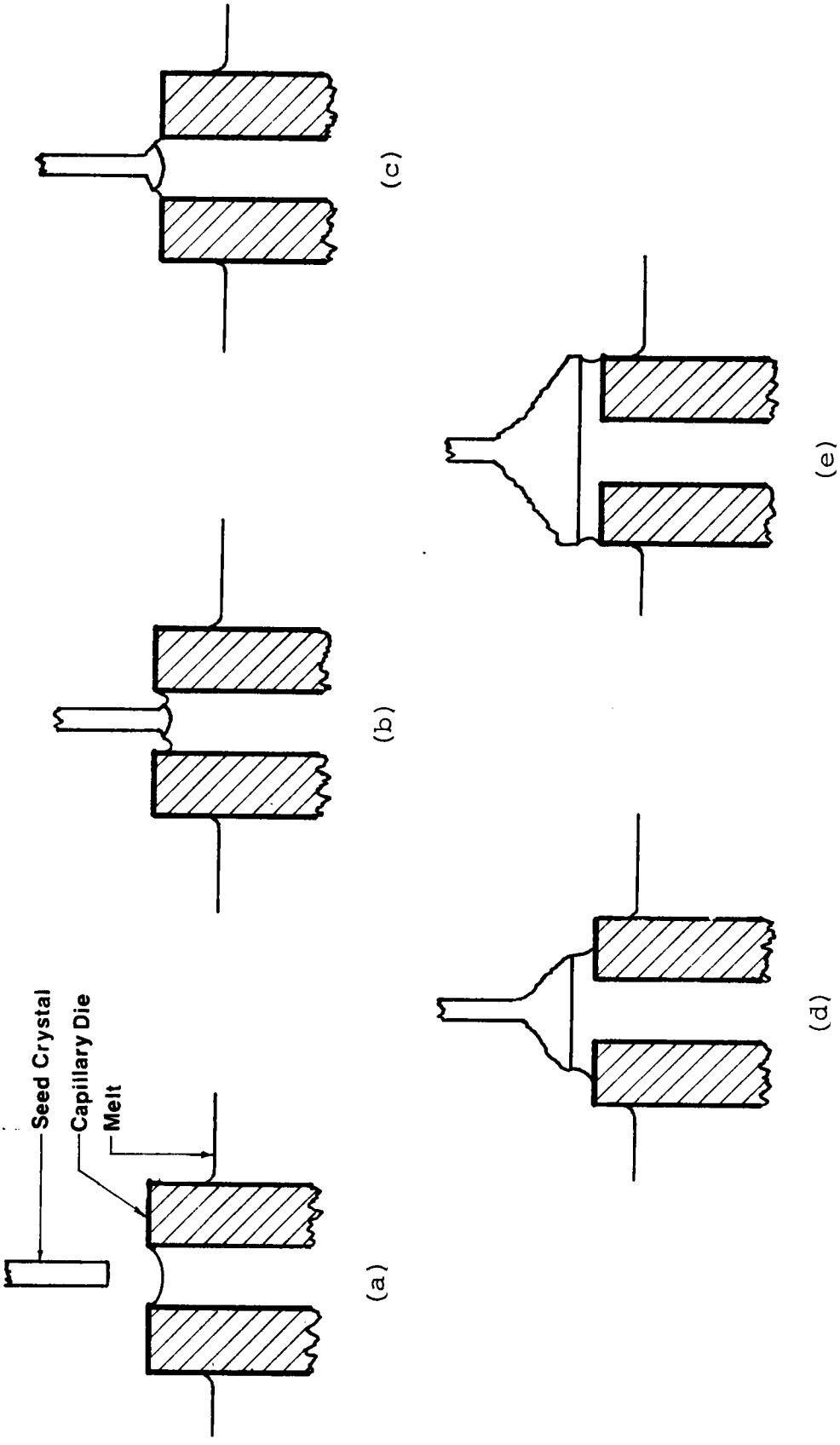


Figure 5. Sequential seeding and spreading operation which takes place in EFG.

depression or hole with vertical walls and defined edge may be placed in the die surface and the liquid film will stop at this edge and spread around it; see Figure 6. In this manner tubular cross sections may be obtained directly from the melt even for brittle materials. However, a minimum hole size exists, depending upon the surface tension of the liquid, below which the film around the hole will fill in over the hole.[9]

Current applications of Edge-defined, Film-fed Growth include the production of various cross-sectional shapes of sapphire (Al_2O_3) and ruby crystals such as filaments, rods, tubes and ribbons.[8] The production of silicon single crystal in ribbon form for use in the conversion of solar energy into useful power,[11] and the growth under high temperature gradients of directional in situ composite eutectics for use in high temperature jet engine type of materials applications are other current potential uses for the process.[12,13]

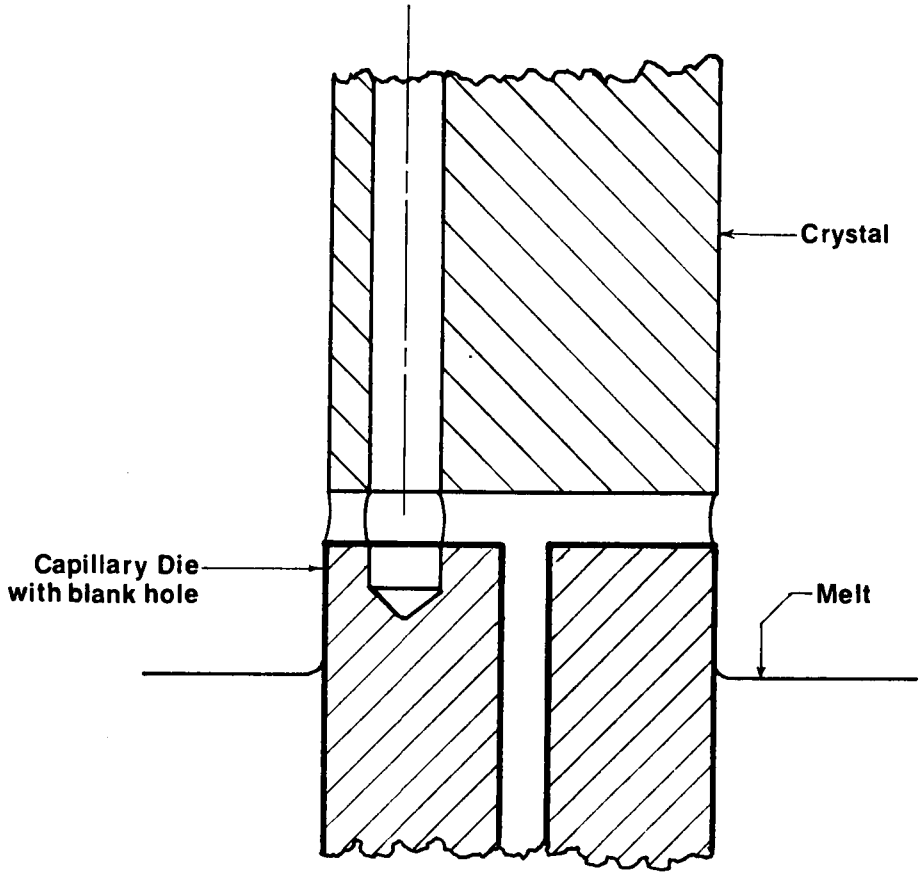


Figure 6. Schematic diagram of the growth of a shaped crystal with a hollow cross section by EFG.

II. THEORETICAL CONSIDERATIONS

In this section theoretical models are formulated to describe the conditions under which steady-state Edge-defined, Film-fed Growth can be achieved. For completeness, a short review of fluid statics will be undertaken followed by discussions of fluid flow and heat transfer problems pertinent to the EFG process and a discussion about the meniscus film.

Fluid Statics

Consider a liquid drop in contact with a flat, planar, homogeneous, nondeformable solid surface. The drop will assume a shape such that the free energy of the system is minimized. Thomas Young[10] showed that the conditions for equilibrium in this case result in equation (3) for the solid-liquid intersection.

$$\gamma_{sg} - \gamma_{sl} = \gamma_{lg} \cos \Phi_d^* \qquad (3)$$

where γ is a surface tension, subscripts lg, sg and sl refer to liquid-vapor, solid-vapor, and solid-liquid interfaces respectively. Φ_d^* in equation (3) is the equilibrium wetting angle; see Figure 7. When Φ_d^* is less than 90, then the liquid is said to wet the solid. When $\Phi_d^* = 0$, wetting is complete. When Φ_d^* is greater than 90, the liquid is nonwetting with respect to the solid, and when $\Phi_d^* = 180$, this is termed complete nonwetting.

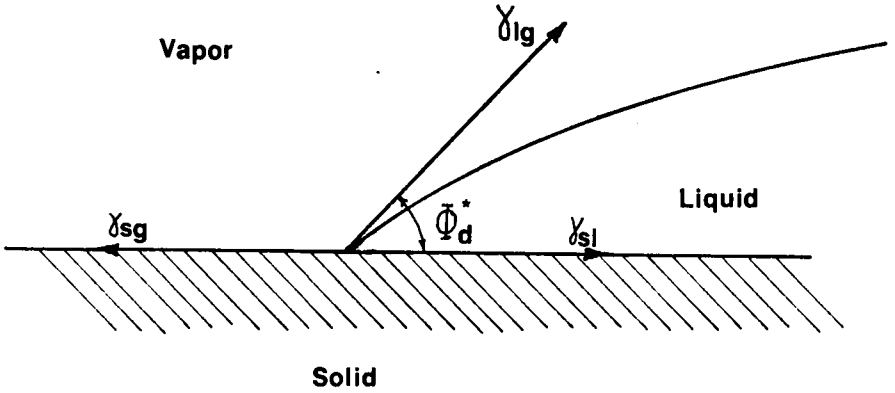


Figure 7. Solid-liquid-vapor intersection of a liquid drop resting on a solid substrate.

The height to which a liquid will rise in a capillary is determined by the balance of forces of the surface tension of the liquid and gravity acting on the column of liquid. For a small diameter capillary such as that shown in Figure 8a, the relationship is expressed approximately as

$$\Delta P_l = \rho g h_o = \frac{2\gamma \cos \Phi_d^*}{r_o} . \qquad (4)$$

Here, ΔP_l is the pressure head of the column of liquid, ρ is the fluid density, g is the gravitational constant, h_o is the height of the liquid column above the liquid level in the reservoir, γ is the surface tension of the liquid, and r_o is the radius of the capillary hole. Equation (4) may be rearranged to give a direct expression for the column height, h_o, as is done in equation (5),

$$h_o = \frac{2\gamma \cos \Phi_d^*}{g V_o \rho} . \qquad (5)$$

For a capillary formed between two parallel flat plates $r_o = \frac{t}{2}$, where t is the spacing between the plates; see Figure 8b.

In EFG, the capillary rise situation is somewhat different from that of the basic static capillary rise case just discussed. Referring to Figure 9 we see that the height of the fluid column during EFG extends to the solid-liquid

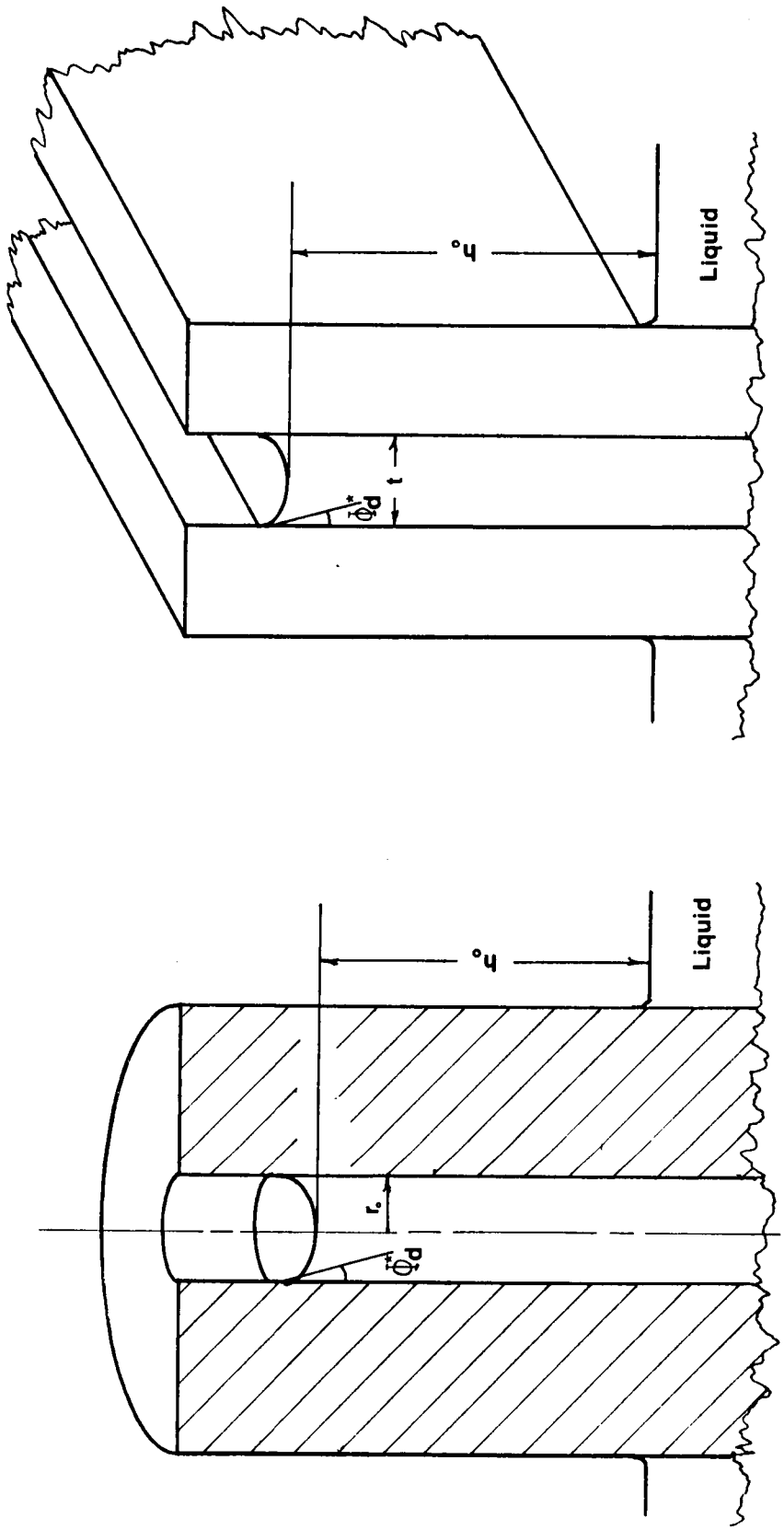


Figure 8. Schematic diagram of liquid rising in a capillary.

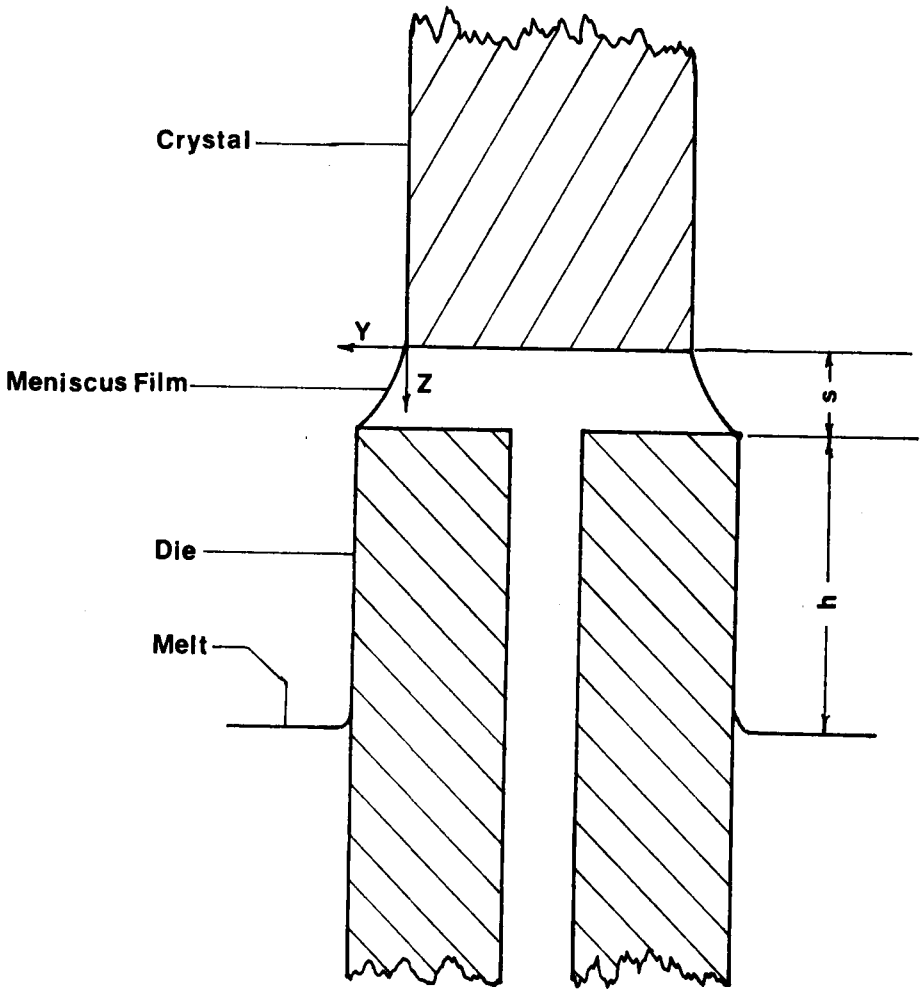


Figure 9. Schematic diagram of a crystal growing via the EFG process.

growth interface above the top of the die. Not only is there a pressure difference required to raise the fluid in the capillary, but also the pressure difference required to maintain viscous flow through the capillary and in the meniscus film. Thus, there are three distinct yet related pressure terms. Δp_1 is the hydrostatic head due to the height of the fluid column which extends from the bulk liquid level to the solid-liquid growth interface. Δp_2 is the pressure difference required to maintain viscous flow in the capillary, and Δp_3 is a pressure difference required to maintain viscous flow in the meniscus film layer. The two pressure terms for viscous flow can, under steady-state conditions, be expressed as a pressure head. This is done in equation (6) below.

$$\Delta p_v = \rho g h_v \tag{6}$$

where h_v is the apparent height due to pressure drops causing viscous flow. For any given point on the meniscus surface in Figure 9 the pressure is expressed by

$$\Delta p = \rho g(h + s - Z) + p_v \ . \tag{7}$$

Fluid Dynamics

Turning directly to the fluid flow aspect of EFG, two separate regions of fluid flow are apparent. The first is

fluid flow in the capillary, and the second is fluid flow in the meniscus film.

Considering fluid flow in the capillary first, three specific cases of interest arise: (i) fluid flow in a capillary of circular cross section, (ii) fluid flow in a capillary slot between two flat plates, and (iii) fluid flow in an annular capillary formed by concentric tubes of circular cross section. Each case is taken in turn.

Case (i): laminar flow in a capillary of circular cross section. Taking the flow in the capillary to be laminar and at steady-state, it then follows that $\frac{dp}{dz}$ = constant; see Figure 10. The expression for fluid velocity in the z-direction[14] is

$$V_z = \frac{r_o^2 - r^2}{4\mu} \frac{dp}{dz} , \tag{8}$$

where r_o is the radius of the capillary, r is any given radius less than r_o and μ is the dynamic viscosity of the fluid. Using equation (8) the volumetric flow rate is computed,

$$Q = \int_{tube} VdA = \frac{p_1 - p_2}{\Delta z} \frac{\pi}{\mu} \frac{r_o^4}{8} . \tag{9}$$

The average velocity, $\bar{V}_1$, is then given by

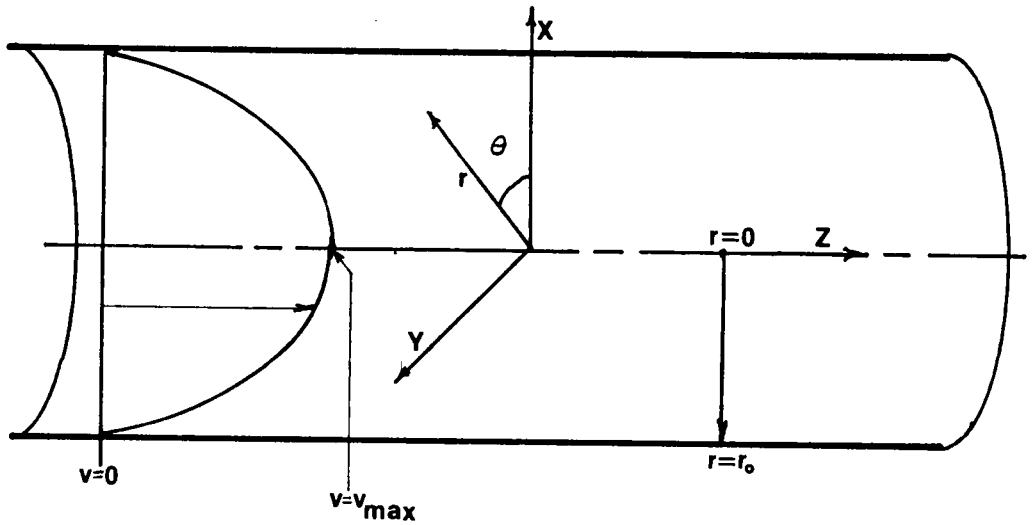


Figure 10. Fluid flow in a capillary tube.

$$\bar{V}_1 = \frac{Q}{\pi r_o^2} = \frac{\Delta p}{\Delta z} \frac{r_o^2}{8\mu} . \tag{10}$$

Letting $L = \Delta z$, substituting L into equation (10) and then rearranging the equation yields

$$\Delta p_2 = \frac{\bar{V}_1 L 8\mu}{r_o^2} \tag{11}$$

an expression for the viscous pressure drop, Δp_2, over a distance L of capillary. Now consider the case where a solid rod crystal of radius r_1 is growing at a velocity V_g off a die with a capillary of radius r_o. The condition for mass conservation becomes

$$\pi r_1^2 \rho_s V_g = \pi r_o^2 \rho_\ell \bar{V}_1, \tag{12}$$

where ρ_s is the density of the solid and ρ_ℓ is the density of the liquid. Solving for $\bar{V}_1$ in equation (12) and reentering the result into equation (11) leads to

$$\Delta p_2 = \frac{8\mu L r_1^2 \rho_s V_g}{r_o^2 \rho_\ell} . \tag{13}$$

Equation (13) is the expression for the pressure required to maintain liquid flowing through a capillary tube of radius r_o and length L at the rate required to maintain a crystal of radius r_1 growing at velocity V_g.

Case (ii): laminar flow in a narrow slit capillary. The flow between the flat, parallel plates separated by a distance 2B is taken as laminar and steady-state for which $\frac{dp}{dz}$ = constant; see Figure 11. Flow occurs in the z-direction only. The expression for the velocity[15] is

$$V_z = \frac{(p_o - p_L)B^2}{2\mu}\left[1 - \left(\frac{x}{B}\right)^2\right] . \qquad (14)$$

Here, B is one half the spacing between the plates, p_0 is the pressure at z = 0, p_L is the pressure at z = L, and the section of length L is assumed to be far away from any end effects. The average fluid velocity is found to be

$$\bar{V}_z = \frac{\Delta p}{L} \cdot \frac{1}{3\mu} B^2 . \qquad (15)$$

From equation (15), the pressure drop over the length L of capillary, Δp, can be expressed as

$$\Delta p_2 = \frac{\bar{V}_z L 3\mu}{B^2} . \qquad (16)$$

To obtain an expression for the pressure drop causing viscous flow in a narrow slit capillary during edge-defined, film-fed growth of a ribbon shaped crystal, assume that a crystal of dimensions w_c by t_c is growing at a rate V_g from a die having a capillary slot of cross section t by w. The conservation of mass requires that

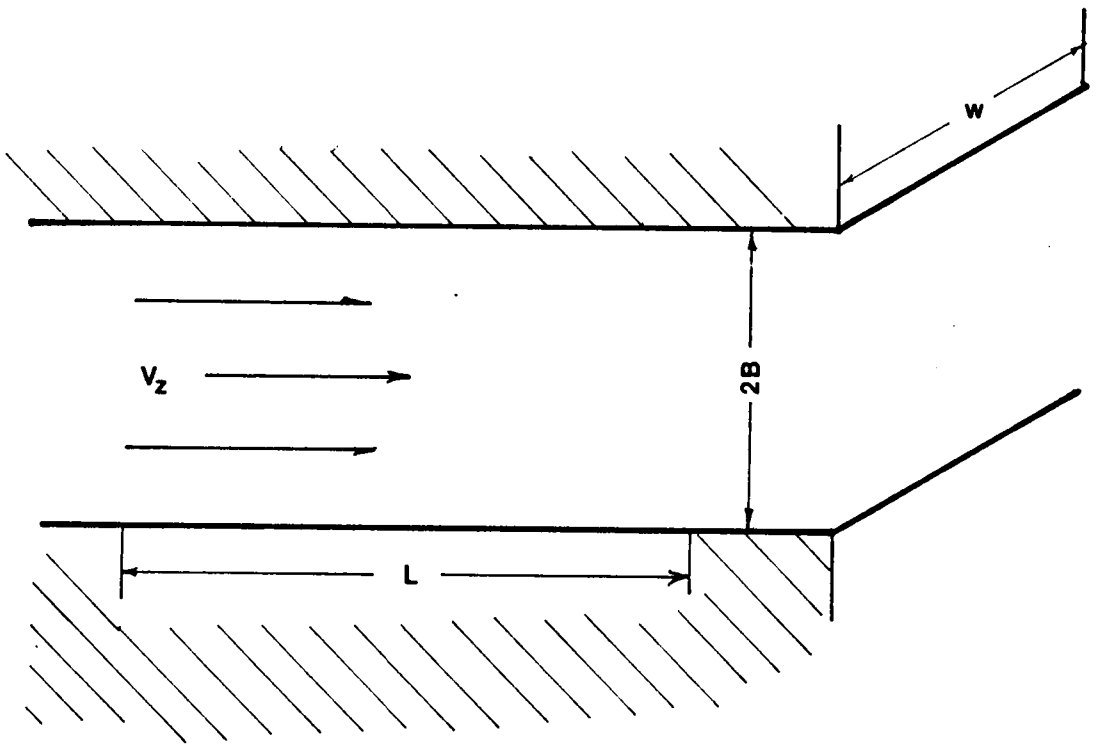


Figure 11. Fluid flow in a capillary slit.

$$w_c\, t_c\, V_g\, \rho_s = t\, w\, \bar{V}_z\, \rho_\ell \qquad (17)$$

holds true. Solving equation (17) for $\bar{V}_z$, substituting that expression back into equation (16), and letting B = t/2 yields

$$\Delta p_2 = \frac{12 w_c\, t_c\, V_g\, \rho_s\, \mu\, L}{t^3\, w\, \rho_\ell} \,. \qquad (18)$$

Equation (18) is an expression for the pressure required to maintain flow through a capillary of dimensions w by t to feed a crystal of dimensions w_c by t_c growing at a velocity, Vg.

Case (iii): laminar flow in an annular capillary. An incompressible fluid is flowing at steady-state in the laminar mode through the annular region between two coaxial cylinders of radii kR and R_c; shown in Figure 12. The velocity distribution for steady-state flow[15] is

$$V_z = \frac{(p_o - p_L)}{4\mu L} R^2 \left[1 - \left(\frac{r}{R}\right)^2 + \left(\frac{1 - k^2}{\ell n \left|\frac{1}{k}\right|}\right) \ell n \left(\frac{r_c}{R}\right)\right] . \qquad (19)$$

From (19) the average velocity is found to be

$$\bar{V}_z = \frac{(p_o - p_L)\, R^2}{8\mu L} \left(\frac{1 - k^4}{1 - k^2} - \frac{1 - k^2}{\ell n \left(\frac{1}{k}\right)}\right) . \qquad (20)$$

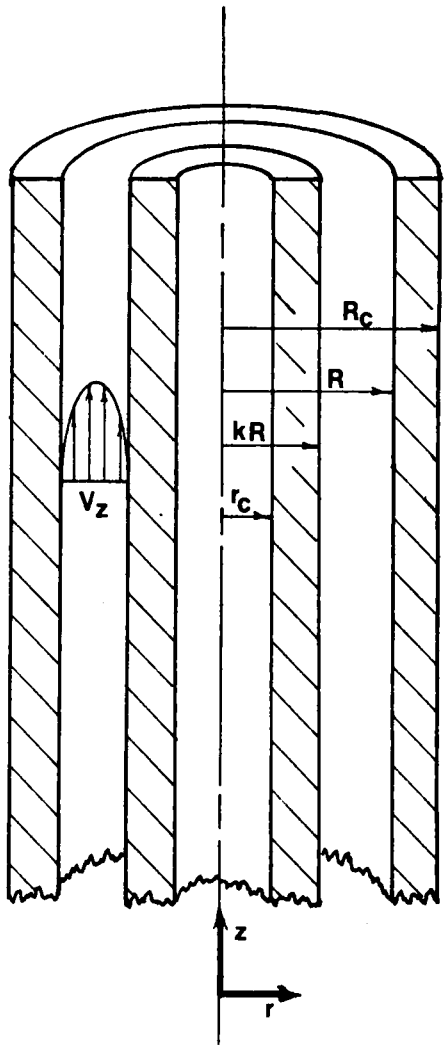


Figure 12. Fluid flow in an annular capillary.

Once again, consider a crystal of tubular cross section growing at velocity V_g from a circular die; see Figure 12. The outside diameter, R_c, inside diameter, r_c, and the length is L. The outside diameter of the annular capillary slot is R and the inside diameter, kR. By the conservation of mass,

$$(\pi R_c^2 - \pi r_c^2) V_g \rho_s = [R^2 - (kR)^2]\pi V_z \rho_\ell \ . \qquad (21)$$

Solving equation (21) for V_z and substituting it into equation (20) yields

$$\Delta p_2 = \frac{8 \mu L V_g \rho_s}{[R^2 - (kR)^2] R^2 \rho_\ell} \cdot \left| \frac{1 - k^4}{1 - k^2} - \frac{1 - k^2}{\ell n \frac{1}{k}} \right]^{-1} \ . \qquad (22)$$

Equation (22) is the expression for the pressure required to maintain flow through the annular capillary in sufficient quantity to maintain a tubular cross section crystal growing at velocity V_g.

Now focus on the problem of viscous flow in the meniscus film[16] which is located between the top surface of the capillary die and the solid-liquid growth interface of the crystal above the die. The pressure drop causing flow in the film is described by equation (18), which is an expression for the pressure drop in a liquid flowing between two flat parallel plates. In obtaining expressions for the pressure drop in the meniscus film, two cases of interest will be considered.

Case (i) is that of a solid circular rod of radius r_1 growing off a die fed by a single circular capillary hole of radius r_o positioned in the center of the die; see Figure 13a. Case (ii) is that of a ribbon shaped crystal of rectangular cross section w by t growing off a die formed by two flat, parallel plates closely spaced to form a capillary slit between them of width t_c; see Figure 13b. These cases will be considered in turn.

Case (i). The fluid flows up the capillary and radially outwards onto the top surface spreading to the edge of the die. Letting V be the average fluid velocity in the film, located midway between $r = r_o$, which is the location of V_{max}, and $r = R$, at which point $V = 0$, the mass conservation expression becomes

$$\pi(R^2 - r_o^2)V_g \rho_s = 2\pi s\left(\frac{R + r_o}{2}\right)\bar{V}\rho_\ell \quad . \tag{23}$$

Rearranging,

$$\bar{V} = \frac{(R^2 - r_o^2)V_g \rho_s}{s(R + r_o)\rho_\ell} \tag{24}$$

and then substituting $\bar{V}$ into equation (16) with $R - r_o = L$ and $(s/2) = B$ yields

$$\Delta p_3 = \frac{12\mu(R - r_o)^2 V_g \rho_s}{s^3 \rho_\ell} \tag{25}$$

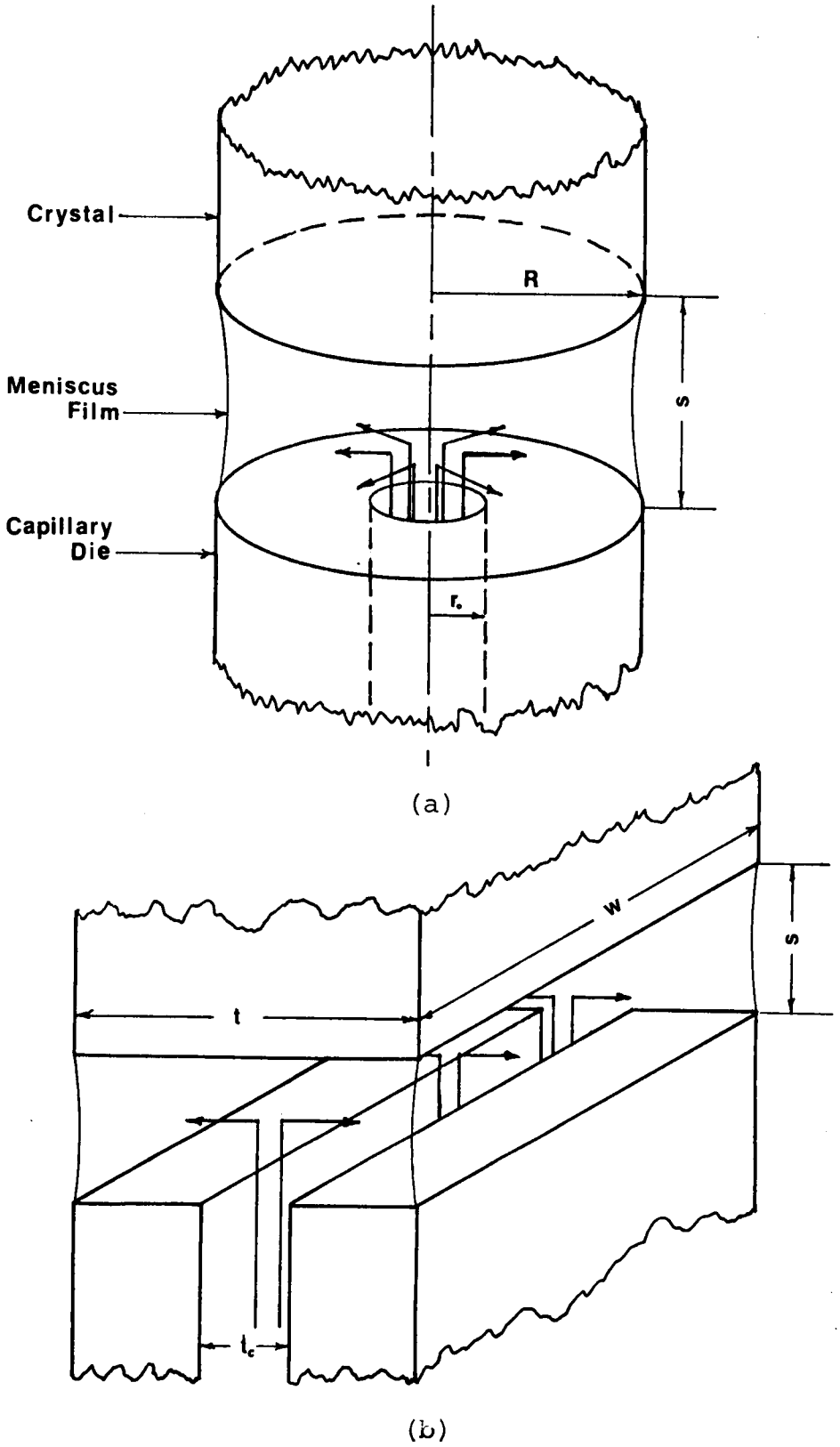


Figure 13. Fluid flow in the meniscus film.

which is the pressure required to maintain flow in the menicus film of case (i).

Case (ii). Figure 13b schematically represents case (ii), that of a ribbon shaped crystal growing off a rectangular die. Fluid moves up the capillary slot to spread over the surface of the die. Taking the average velocity, $\bar{V}$, between $x = (t_c/2)$ and $x = (t/2)$ for a unit width of crystal, the mass conservation equation is

$$2\left\{\frac{t - t_c}{2}\right\} V_g \rho_s = \frac{1}{2}\bar{V}\, s\, \rho_\ell \,. \tag{26}$$

Solving for $\bar{V}$ yields,

$$\bar{V} = \frac{2(t - t_c)\, V_g\, \rho_s}{s\, \rho_\ell} \,. \tag{27}$$

Substituting this result into equation (16) and letting $B = (s/2)$ and $L = (t - t_c)/2$ results in

$$\Delta p_3 = \frac{12\mu (t - t_c)^2\, V_g\, \rho_s}{s^3\, \rho_\ell} \,. \tag{28}$$

Equation (28) is the expression for the pressure necessary to maintain the flow in the meniscus required to adequately feed a crystal growing under the conditions of case (ii).

Heat Flow

Let us examine an approximate analysis of steady-state heat flow conditions found in edge-defined, film-fed growth. This treatment is similar in nature to that done by Chalmers et al.[17] Consider a ribbon shaped crystal of rectangular cross section growing into a thin film on a rectangular shaped die; see Figure 14. The width of the crystal, w_c, is taken to be much greater than the thickness, t_c. The solid-liquid interface is at the point $x = 0$, $z = 0$, and lies in the x-y plane. All temperature gradients are assumed to be in the z-direction. Thus, heat flow by conduction through the ribbon and radiation from the sides of the ribbon determine the temperature profiles found in the ribbon. For the volume element $w_c\, t_c\, \Delta z$ shown in Figure 14, the steady-state heat flow is described by the equation

$$q_1 - q_2 = q_r \tag{29}$$

where

$$q_1 = -k_s\, t_c\, w_c \left(\frac{dT}{dz}\right)_z \tag{30}$$

$$q_2 = -k_s\, t_c\, w_c \left(\frac{dT}{dz}\right)_{z+\Delta z} \tag{31}$$

and

$$q_r = 2(t_c + w_c)\Delta z\, \sigma\, \varepsilon (T^4 - T_1{}^4). \tag{32}$$

In equations (29) through (31) k_s is the thermal conductivity of the solid, $\left(\frac{dT}{dz}\right)_z$ and $\left(\frac{dT}{dz}\right)_{z+\Delta z}$ are the thermal gradients

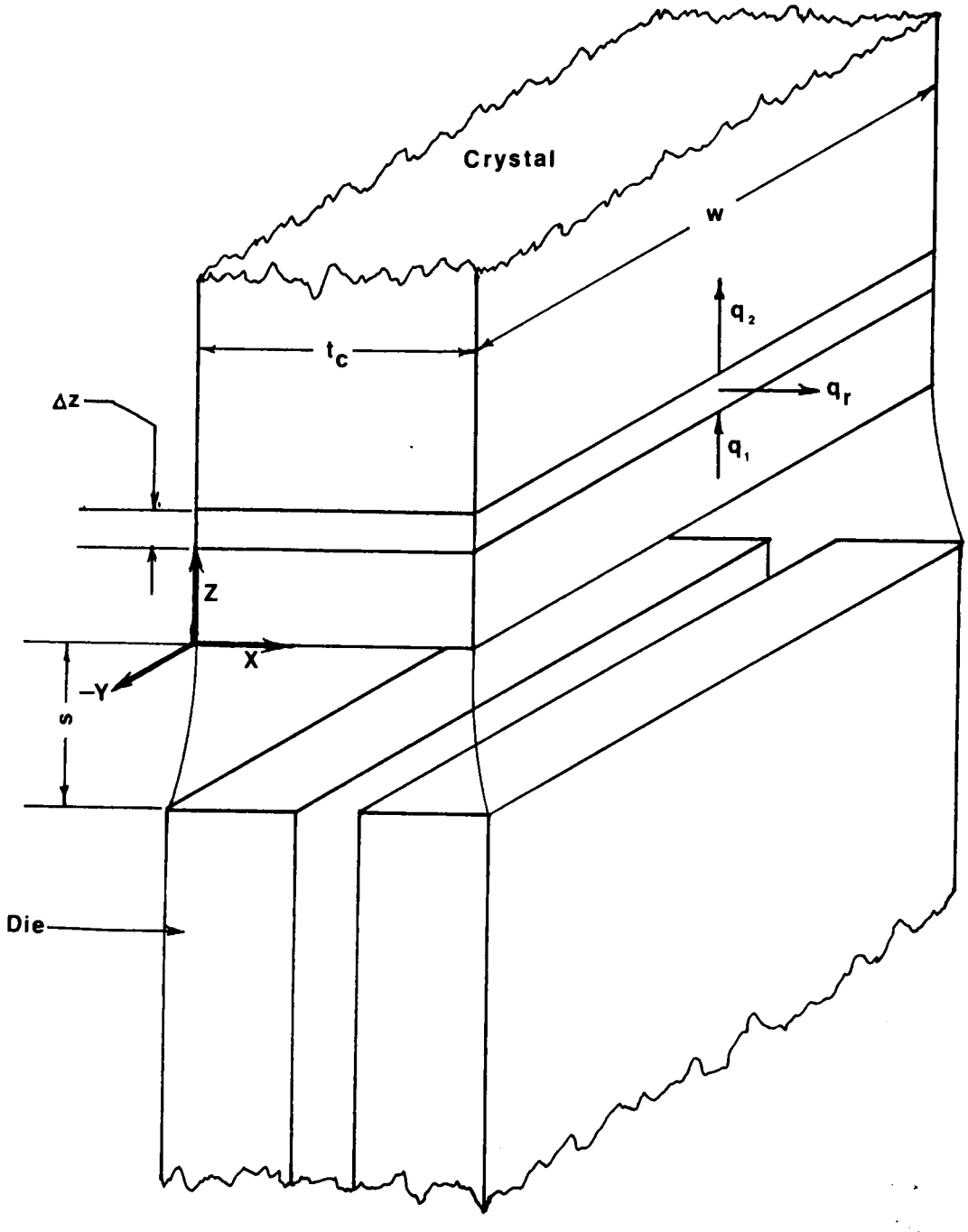


Figure 14. Schematic diagram of the heat flow conditions during edge-defined, film-fed growth of a ribbon shaped crystal.

at the positions z and z + Δz respectively, σ is the Stephan-Boltzman constant, ϵ is the emissivity of the material, T_l is the temperature of the environment, and T is the temperature at $\frac{z + (z + \Delta z)}{2}$. Rearranging equation (29) yields

$$\frac{\left[\left(\frac{dT}{dz}\right)_{z+\Delta z} - \left(\frac{dT}{dz}\right)_{z}\right]}{\Delta z} = \frac{2(w_c + t_c)}{k_s t_c w_c} \sigma \epsilon (T^4 - T_l^4) . \quad (33)$$

The limit as Δz approaches 0, of equation (33) is by definition the second derivitive, $\frac{d^2T}{dz^2}$. Thus equation (33) becomes

$$\frac{d^2T}{dz^2} = \frac{2(w_c + t_c)}{k_s t_c w_c} . \sigma \epsilon (T^4 - T_l^4) . \quad (34)$$

To evaluate equation (34) at the solid-liquid interface the term k_m, the thermal conductivity of the material at the melting point, T_m, must be introduced. The thermal conductivity of the solid is in general inversely proportional to the temperature, T, and is in this case taken as

$$k_s = \frac{T_m k_m}{T} . \quad (35)$$

Substituting the expression for k_s from equation (35) into equation (34) and then integrating[18] under the conditions that $\frac{dT}{dz} = 0$ at $T = T_l$ yields

$$\frac{dT}{dz} = \left[\frac{2(w_c + t_c)\sigma\varepsilon}{3w_c t_c k_m T_m}\right]^{\frac{1}{2}} \cdot \left[T^6 - T_1{}^6 - 3T_1{}^4(T^2 - T_1{}^2)\right]^{\frac{1}{2}} . \qquad (36)$$

Of particular interest is the heat loss, q_I, at the freezing interface. For a unit area of solid-liquid interface the heat loss per unit time is found by evaluating equation (36) at T_m. Using the simplifying assumptions that $T_1 = 0$ and $\frac{w_c + t_c}{w_c t_c} \simeq \frac{1}{t_c}$, evaluation at T_m of equation (36) yields

$$q_I = k_m \frac{dT}{dz}\bigg|_{T_m} = \frac{2}{3}\left[\frac{\sigma \varepsilon k_m T_m{}^5}{t}\right]^{\frac{1}{2}} . \qquad (37)$$

At steady-state q_I must equal the latent heat of solidification, q_L, generated at the interface and the heat, q_F, arriving at the interface by conduction across the meniscus film. For a unit area of interface the latent heat term is

$$q_L = LV_g \rho_s , \qquad (38)$$

where L is the latent heat of fusion, cal/gm, ρ_s is the density of the solid, gm/cc, and V_g is the growth velocity of the solid-liquid interface, cm/sec. The meniscus film term is

$$q_F = k_l(\Delta T/s) , \qquad (39)$$

where s is the film thickness, cm, T is the temperature difference across the film, °C, and k_1 is the thermal conductivity, $\frac{\text{cal}}{\text{gm}\cdot\text{sec}\cdot{}^\circ\text{C}}$, of the liquid. The temperature gradient, $\Delta T/s$, across the film is assumed to be constant. Thus, the equation approximating the steady-state heat balance is

$$\left[\frac{2}{3}\frac{\sigma \varepsilon k_m T_m^5}{t_c}\right]^{\frac{1}{2}} - k_\ell \frac{\Delta T}{s} = L V_g \rho_s \,. \tag{40}$$

Now let us enter into a qualitative analysis of equation (40) for different values of the temperature gradient in the liquid. The point of such a discussion is to determine under what heat flow conditions a stable solid-liquid interface is attainable. This can be done by considering three cases of interest:

Case (i) $(\Delta T/s) = 0$

Case (ii) $(\Delta T/s) > 0$

Case (iii) $(\Delta T/s) < 0$.

Case (i). When $(\Delta T/s) = 0$, this means that in the meniscus liquid there is heat flow neither towards nor away from the solid-liquid interface. The heat balance equation (40), becomes

$$\left[\frac{2}{3}\frac{\sigma \varepsilon k_m T_m^5}{t_c}\right]^{\frac{1}{2}} = L V_g \rho_s \,. \tag{41}$$

Equation (41) is rearranged to yield an expression for the growth velocity,

$$V_g = \left[\frac{2}{3}\,\frac{\sigma\,\varepsilon\,k_m\,T_m}{t_c}\right]^{\frac{1}{2}} \cdot (L\rho_s)^{-1} \quad . \tag{42}$$

Case (ii). A positive temperature gradient in the meniscus film means that heat is flowing towards the freezing interface. Such a temperature gradient at the interface resists the formation of cellular and dendritic growth modes, tending the system towards a planar solid-liquid interface. Assuming that the meniscus film is rectangular in shape and the capillary die is at constant temperature, equation (40) describes the heat flow during steady-state growth.

From equation (38) it may be observed that for a given value of V_g there is a single value of q_L. In equation (40) when V_g is fixed, remembering that T is constant, a unique value of s is implied. If s is made greater than the required equilibrium steady-state value, the difference in heat leaving the interface, q_I, and heat arriving at the interface by conduction across the meniscus film, q_F, increases. This increase in $q_I - q_F$ results in an increase in velocity of growth, V_g, moving the solid-liquid interface back towards the steady-state equilibrium position. If s is made less than its equilibrium value, then $q_I - q_F$

decreases resulting in a decrease in V_g which causes the solid-liquid interface to move towards the steady-state equilibrium position. From this example, it is evident that the system is self-stabilizing with regard to fluctuations in film thickness, s. Also the system is self-stabilizing to a certain extent with respect to variations in the velocity of pull, V_p. This "certain extent" is the limit imposed by the ability of the solid-liquid interface to respond to a change in pull velocity, ΔV_p, coupled with the mechanical integrity of the meniscus film. A sudden increase in V_p results in an enlargement of the meniscus thickness s, which as just discussed, causes an increase in V_g moving the freezing interface towards the steady-state equilibrium position. The reverse of this case, V_p suddenly decreased, also results in a self-stabilizing condition.

Case (iii). If the conditions are such that $(\Delta T/s) < 0$, then heat is flowing through the meniscus film away from the solid-liquid interface. This condition allows high rates of crystal growth to be achieved because heat is removed from the freezing interface both through the growing crystal by radiation and conduction, and through the meniscus film by conduction. The heat going into the meniscus is then transferred to the die or radiated from the surface of the film. Note that here the undercooled film must not be at a low enough temperature to permit nucleation of new crystals

to occur. In this mode of growth, the interface position is not stable because an increase is s would decrease q_F. This would mean that $q_I - q_F$ decreases which, from equation (40), implies a decrease in V_g. Thus, the interface has no tendency to move back to its equilibrium steady-state position. The conditions under which the above statement about stability in Case (iii) is true are (a) that radiation from the meniscus is so small as to be neglected, (b) that the cross section dimensions of the crystal do not depend on the value of s, and (c) that fluctuations in die temperature are ignored.

For example, consider the case of a small rod of radius R growing from a cylindrical film. For this case the surface area of the meniscus film, $2\pi Rs$, is large in comparison to the area of the solid-liquid interface, taken to be approximately πR^2. Hence an increase in s causes a significant heat loss through radiation from the meniscus film surface; see Figure 15. This radiant heat loss leads to an increase in V_g tending to return the interface to its original steady-state position. If s is decreased, then likewise V_g decreases as a result of the lower rate of heat loss from the film surface. When the crystal radius, R, decreases with increasing s, which occurs when $s < R_1$, the growth rate, V_g, increases in porportion to R_1^2/R^2 for a constant volumetric solidification rate. Once again, increasing s results in a self-stabilizing effect changing s towards its steady-state value. However, if $s > R_1$ then an increase in s results in

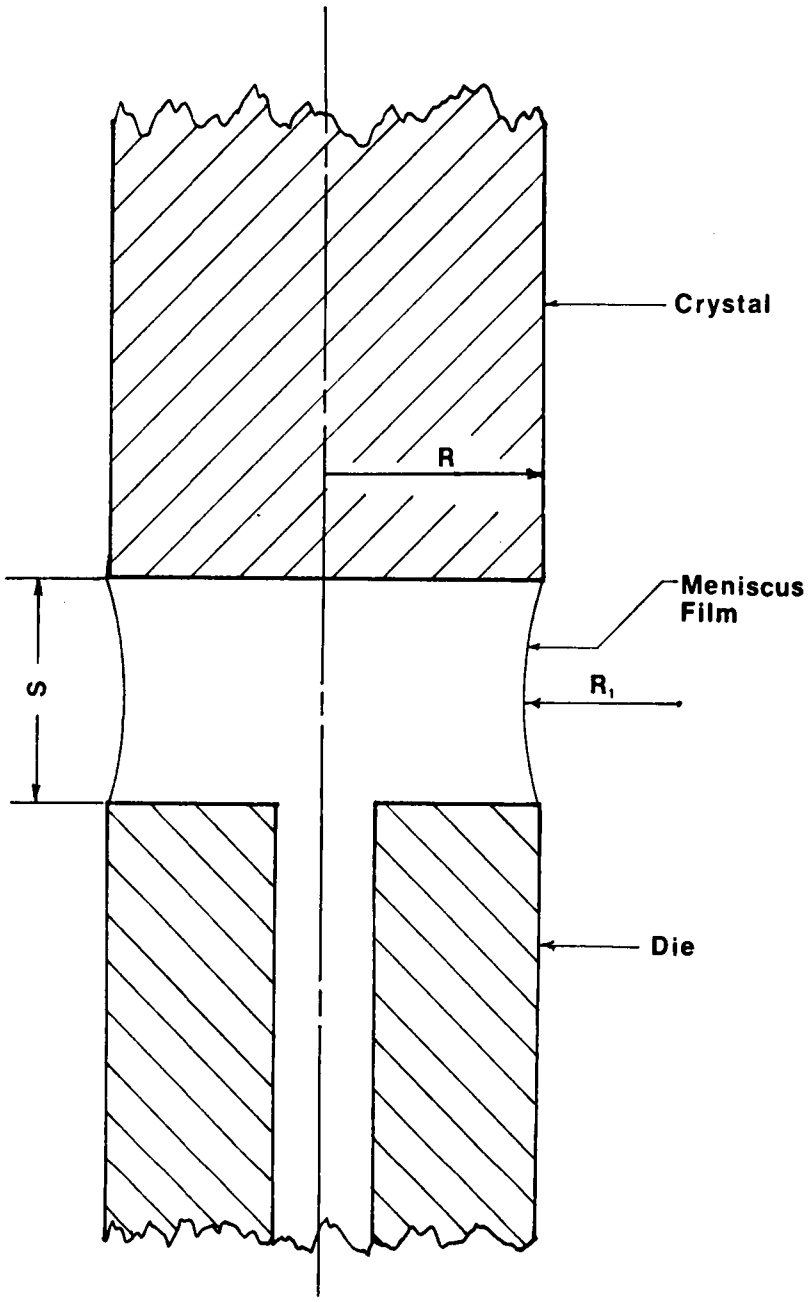


Figure 15. Schematic diagram of a small diameter filament crystal growing by the EFG process.

a larger value of R and a decrease in V_g which is an unstable situation. Therefore, for interface stability it is necessary that $s < R_1$. Also for stability it is necessary that that R be small so that the area of the meniscus surface, $2\pi Rs$, be large in comparison to the area of the freezing interface, πR^2. Chalmers[17] notes that the mode of growth when $(\Delta T/S) < 0$ is stable only for the growth of filaments where R_1 is not appreciably larger than R (e.g., Al_2O_3 filaments of radius 0.01 cm, $V_{g,max} = 0.2$ cm/sec). While for crystals of larger size, he states that stable growth occurs only when $(\Delta T/s) > 0$ and at relatively low velocities (e.g., for Al_2O_3 filaments greater than 0.01 cm radius, $V_{g,max} = 0.04$ cm/sec for $(\Delta T/s) > 0$).

Meniscus Film Considerations

As mentioned in the introduction, it is necessary in an EFG process system that the melt wet the die material. This wetting criterion is required in order to utilize capillary action to provide liquid feed to the meniscus film and to assist the film to spread over the top surface of the die. The conditions of wetting angle which induce the film to spread across the die are of interest and will now be considered. In a situation such as shown in Figure 7, page 15, a drop of liquid rests upon a solid substrate. An equilibrium wetting angle, Φ_d^*, is established at the

solid-liquid-vapor junction. As long as the wetting angle, Φ_d, is at the equilibrium value, the size and position of the drop will remain constant (i.e., no spreading or contraction). In order to induce the liquid to spread over the solid substrate it is necessary to make Φ_d greater than Φ_d^*. When this is accomplished, the liquid will spread across the solid attempting to find a position where it can reestablish the equilibrium wetting angle, Φ_d^*. In a like manner, if Φ_d is made less than Φ_d^*, then the drop's solid-liquid-vapor junction perimeter recedes until the equilibrium wetting angle is again established. In the EFG case, one desires the film to spread completely to all edges of the die top surface and remain there during growth so that the crystal growing will have the cross-sectional shape of the die. This means that the meniscus film must take on a shape such as to make Φ_d be greater than Φ_d^* during the spreading stage. Further, the film must induce Φ_d to be greater than or equal to Φ_d^* when complete wetting is achieved in order to maintain a growing crystal with desired cross-sectional dimensions. This is important because it is the ability of EFG to produce a crystal within desired dimensional tolerances that is basically the criterion for stability of the process.

Because EFG is a meniscus film controlled process there has been interest in determining the shape and stable limits

of the meniscus film. Chalmers, et al.[19] discusses stability using a very simple model of the meniscus film surface. The film surface is assumed to have circular shape of radius r_1. From this model is developed a criterion of stability for a cylindrical crystal of radius r_3 growing off of a die of radius R_d such that stable growth is maintained as long as the radius of the crystal is between the limits $R_d \pm r_1$. The limiting cases occur when the meniscus thickness, s, equals r_1.

Chalmers, Surek et al.[16] use a much more sophisticated and accordingly more complex model to study meniscus film shape in EFG. By employing modified models of liquid capillary rise against vertically oriented plates and rods, simplifying assumptions about contact angles and the use of numerical methods to solve the equations generated, they are able to characterize the shape and mechanical limitations of the meniscus film in EFG. However, it is important to note here that the case just described is limited in two important respects. First, it describes the meniscus film while in a static mode (i.e., no steady-state growth taking place). Secondly, it is not confirmed by careful, quantitative experimental observation. This lack of precise experimental observation of the meniscus film is primarily due to the extremely small thickness of the film, usually less than 0.5 mm, making it most difficult to observe with accuracy. One of the shortcomings of the apparatus used

in the present study is that inadequate provision was made for observing the meniscus film from a directly horizontal vantage point.

Recently Surek and Chalmers[20] have described a method for studying the relationship between the growth direction of a crystal surface and the meniscus angle at the solid-liquid-vapor junction. They utilize an angle, δ, as a parameter to characterize the relation between the growth direction of the crystal surface and the liquid-vapor interface at the solid-liquid-vapor junction. In Figure 16, the relationship between the direction of growth of the crystal surface and the meniscus film at the solid-liquid-vapor interface is schematically shown. B is the direction of growth of the crystal surface, A is the direction of crystal pull or growth axis, θ is the angle between A and B, and Φ is the angle between the meniscus and growth axis. During growth of a crystal of constant cross section, $\theta = 0$ and $\delta = \Phi$. When a crystal is growing with steady-state cross section, Φ is designated Φ_o. Surek and Chalmers have determined Φ_o for silicon and found it to be $11° \pm 1°$.[20] In further studies[21] they determined Φ_o to be $13° \pm 1°$ for germanium, and their experiments also indicate that Φ_o is a material parameter not affected by growth rate and crystal dimension. The determination of Φ_o was carried out on samples of various size which were solidified at a number of

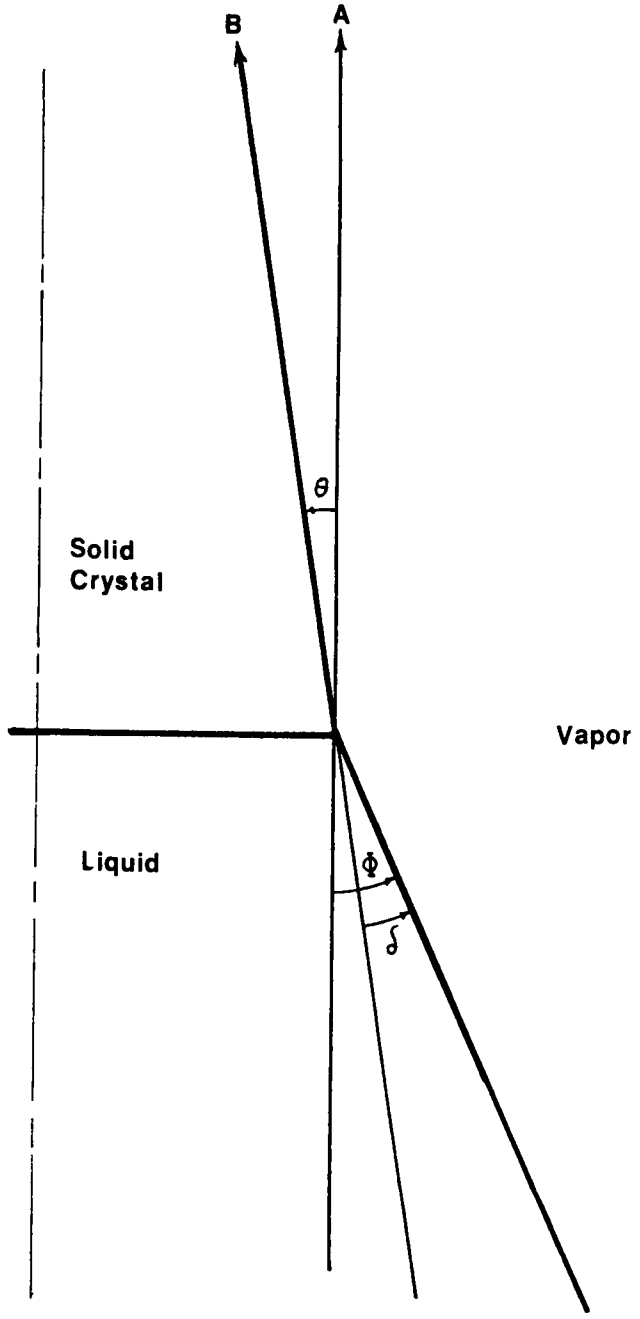


Figure 16. Schematic illustration of the solid-liquid-vapor interface of a crystal growing from the melt.

velocities. The angle Φ_o is an actual steady-state determined parameter and not a staticly determined quantity which makes it a quite useful parameter from a crystal growth point of view.

Surek[22] went further with the work just described and has outlined a theory of shape stability in crystal growth from the melt based on meniscus considerations. Stability is taken to mean the ability to grow crystals of a given cross section in a steady-state fashion. In particular, if one perturbs Φ such that $\Phi \neq \Phi_o$ and the crystal changes shape, stabilization is said to occur if the resultant change in crystal shape is such that Φ again approaches Φ_o thus establishing steady-state growth under the new conditions. When Surek applied his analysis to the EFG case, he found that the stability of the process from the point of view of the meniscus was at worst conditionally stable. Although Surek's analysis of shape stability is done for the dynamic case, it must be kept in mind that the analysis describes stability only in regards to the meniscus film configuration. All thermal gradients in the system have been assumed to remain constant. In a real system a change in the meniscus film and consequently the growing crystal will result in a change in the heat flow conditions. To date there has been no stability analysis made of the EFG process which takes into account the coupled nature of the heat flow and meniscus shape problem.

III. EXPERIMENTAL SETUP

The crystal growth unit used for the EFG work described in this paper was designed and built at the Chemical and Metallurgical Engineering Department of The University of Tennessee at Knoxville. For convenience the total system will be discussed as three separate component groups. These groups are: (1) power source and controls, (2) the containment chamber, and (3) the support structure including framework, drive train and controls, provisions for atmosphere control and vacuum pump. A picture of the component groups integrated into the complete crystal growth system is shown in Figure 17. The separate groups will now be discussed in order.

Power Source and Controls

The power source for the crystal growth system is a Lepel High Frequency Induction Heating Unit, Model T-15-3-KC-A-S. This model Lepel induction heating unit delivers up to 15 Kw of power. The power from the Lepel unit is transferred to the crucible/die setup by means of a water-cooled induction coil. The 15-turn coil is fabricated from 0.64 cm diameter copper tubing and measures 11.4 cm in height and 8.9 cm in inside diameter. The current frequency in this particular coil was measured and found to be 322 KHz. The

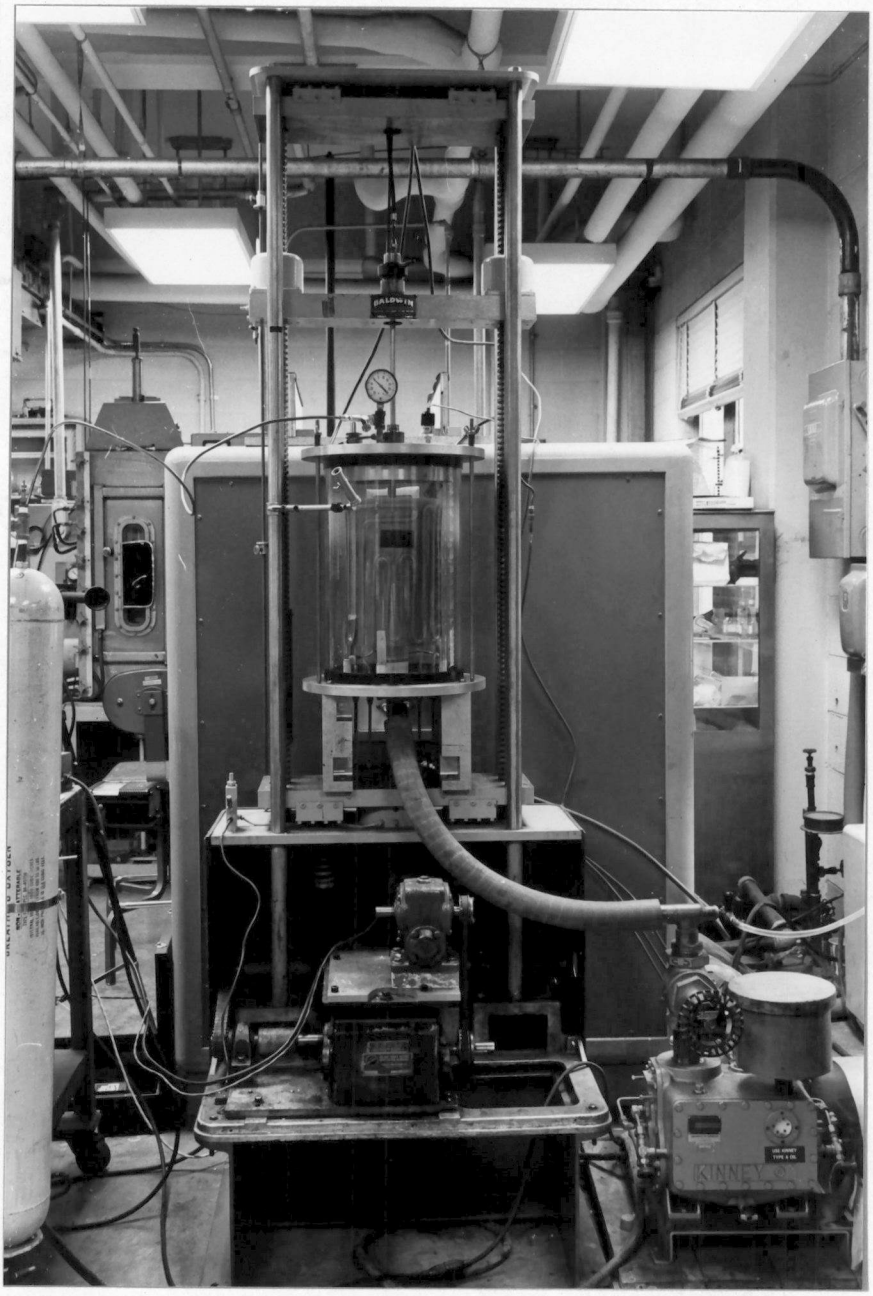


Figure 17. The complete EFG crystal growth system.

coil, which is located inside the containment chamber, is connected to a coaxial lead which passes through an electrically insulated O-ring seal in the aluminum bottom plate of the containment chamber assembly. The coaxial lead is connected on the outside to the output terminals of the Lepel unit by 0.64 cm copper tubing.

It was determined through repeated failures at the outset of the experimental work that the power control, which is standard equipment on the Lepel unit, is much too coarse a control to be used to obtain the precise temperature adjustments needed for stable crystal growth. For that reason a modification was made to the power output control system of the Lepel unit.

For a brief overview of the modification made, let us begin with the coil assembly. The coil itself receives its energy in the form of high frequency current that is generated by a power oscillator triode tube inside the Lepel unit. The amount of power sent to the coil depends directly on the value of the plate current in the power oscillator tube. That is to say, the power sent to the coil increases with increasing plate current. This plate in the power oscillator tube receives a three phase signal from the total output of three thyratron of rectifier tubes. The output of these rectifier tubes is such that it is necessary that both the voltage waveform of the plate and the voltage

waveform of the grid in each of these tubes be positive at the same time in order for the tube to be conducting and a signal be sent to the power oscillator tube. An electronic device was constructed which shifts the waveform of the rectifier tube grid voltage with respect to time over a short range and in very small increments. This "phase shifter" device was connected to the primary side of the control grid transformer, and actually acts as a fine vernier to the standard power rheostat control. By shifting the grid voltage waveform, the interval of time that the rectifier tubes are conducting is altered. Thus, the plate current of the oscillator power tube is altered thereby changing the current in the coil and the power received by the load. Since this variation in grid voltage waveform can be altered in very small increments, a fine degree of control is attainable over the power sent to the load. In the described manner a sensitive and reproducible temperature control of the crucible/die setup was achieved. Before the fine power control was added to the Lepel unit, the best control that could be achieved with the standard rheostat was in minimum increments of 0.25 amps triode tube plate current. The total range of interest of power settings for the experiments done covered only 0.00 to 3.00 amps plate current. Clearly the coarseness of control was a major difficulty. The fine power control, or phase shifter, employs a 15 turn precision

potentiometer which is used to alter the power output of the Lepel unit. This precision potentiometer allows one to obtain accurate and reproducible power settings in increments estimated to be 0.001 amperes triode tube plate current in the range of interest. This permits temperature control of crucible/die setups in increments estimated to be 0.5 centigrade degrees in the range of interest for the experiments herein discussed. This control is superimposed on the main rheostat power control which allows this precise control of power output to be obtained even at high plate current settings.

The Containment Chamber

The containment chamber consists of a cylindrical Pyrex tube 30.5 cm in diameter by 47.0 cm in height; see Figures 18 and 19. It is sealed with L-shaped rubber gaskets at both ends to aluminum end plates. The aluminum end plates measure 40.6 cm in diameter by 1.3 cm in thickness and have smooth circular channels of 1.8 cm width and 0.16 cm depth in their facing surfaces to accept the gaskets of the outer Pyrex tube. The bottom plate is firmly bolted to two rectangular magnesium blocks which measure 25.4 cm by 6.4 cm by 20.3 cm in size and are placed 19.1 cm apart on the support frame to create a space between the bottom end plate and the support frame. In this space the lower half of the coaxial lead,

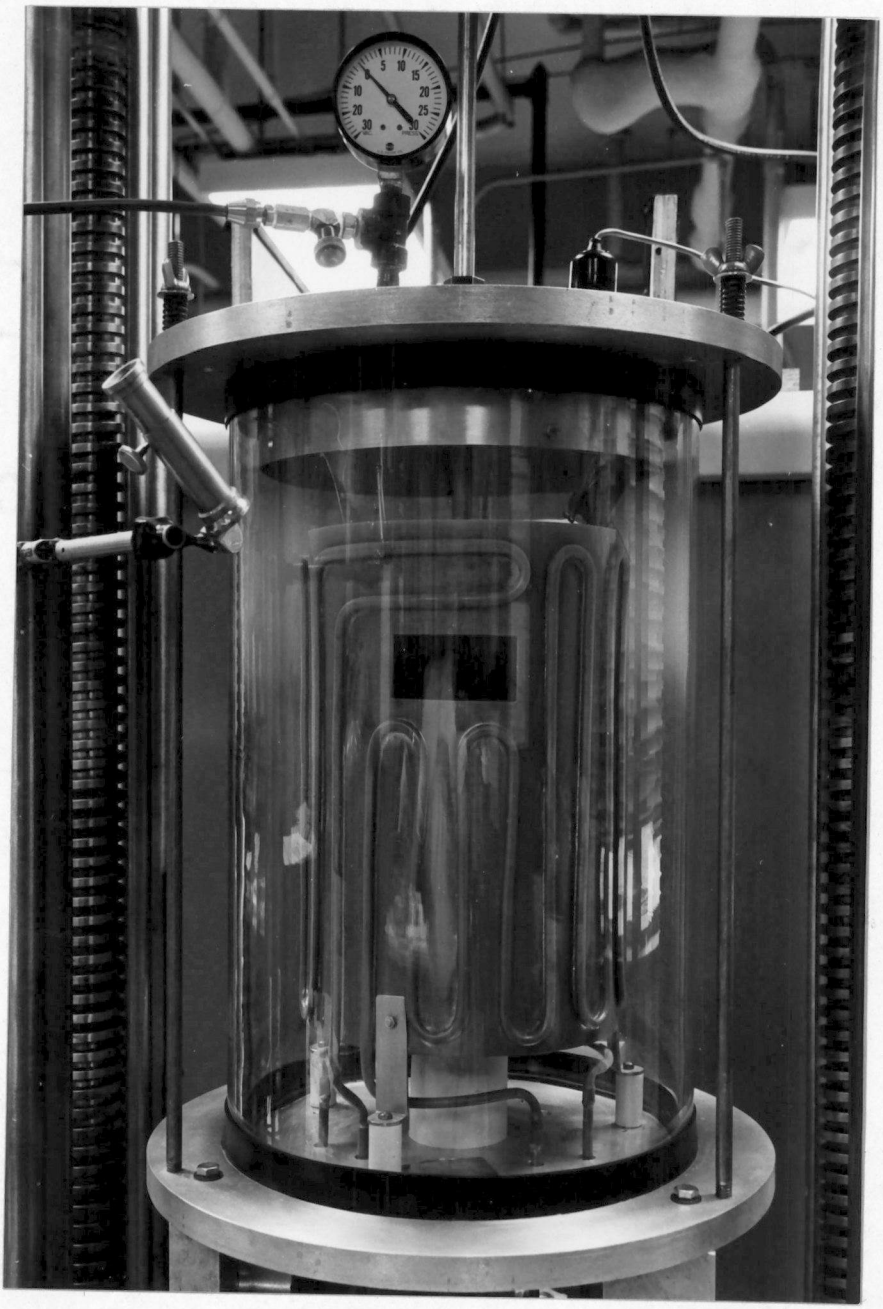


Figure 18. The containment chamber portion of the crystal growth unit.

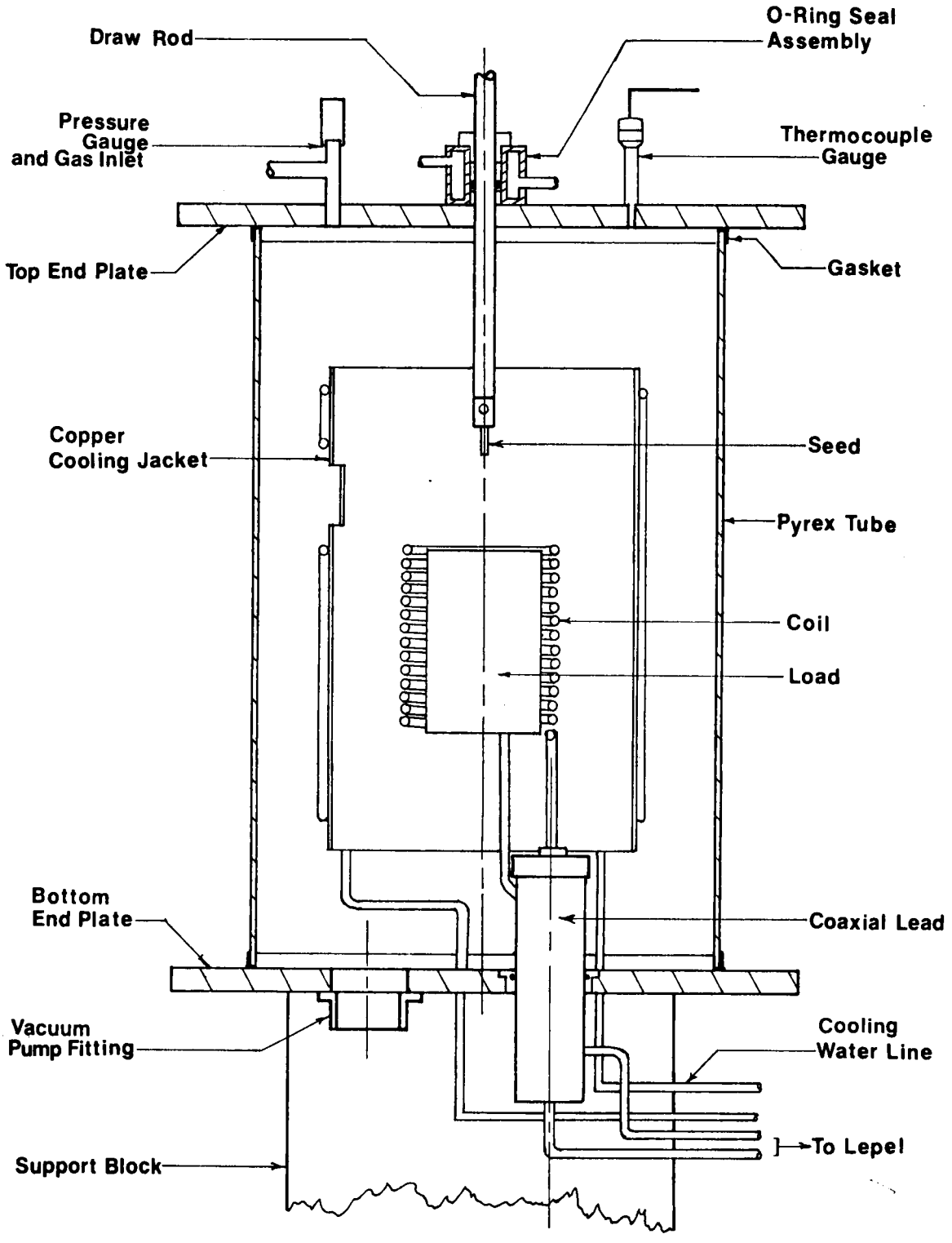


Figure 19. Schematic diagram of the containment chamber. Scale 1:4.

which passes through the bottom plate, is positioned along with four 0.64 cm copper water lines, which maintain cooling water to the inner copper cooling jacket, and a fitting that allows connection of the chamber to a mechanical vacuum pump. The top end plate has a water cooled sliding O-ring vacuum seal fitting mounted in its center. A 1.27 cm diameter water-cooled stainless steel rod passes through this seal. The end of the stainless steel rod inside the chamber is made to accept the seed crystal holder; see Figure 20. This rod provides the mechanical connection of the growing crystal to the moving crosshead which pulls the crystal upwards at a desired velocity. The top end plate also has fittings for controlled atmosphere gas inlet, an ultrahigh vacuum ionization pressure gage, a thermocouple pressure gage and a standard manometer type pressure gage.

Inside the chamber surrounding the induction coil is a water-cooled copper jacket (height = 30.5 cm, diameter = 20.3 cm). This jacket acts as a heat sink for escaping radiation from the load which prevents excessive heating of the outer Pyrex container and aluminum end plates. An opening of dimension 7.6 cm by 3.7 cm has been placed in this copper jacket to allow viewing of the crucible/die setup and growing crystal during a growth run; see Figure 21. A prism is mounted on the top edge of the jacket allowing a high angle view of the crystal and die while the crystal

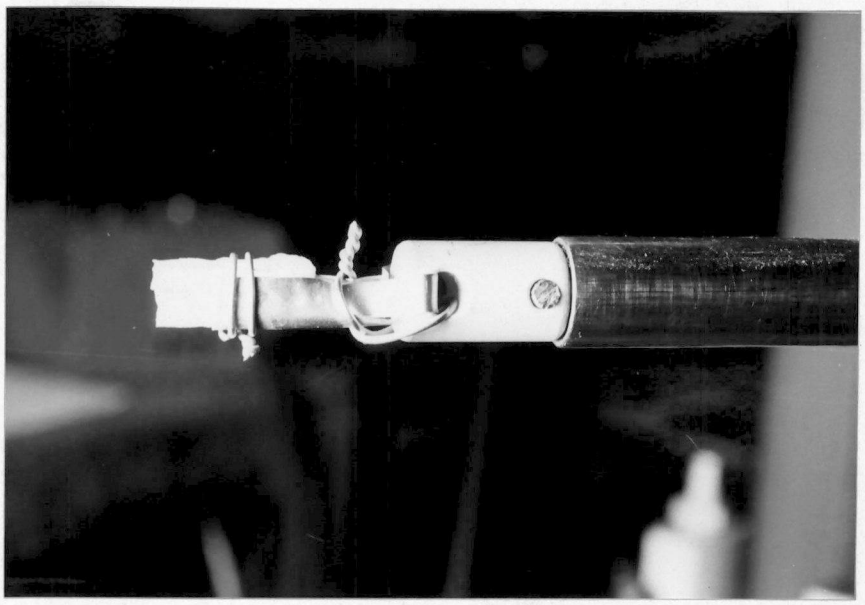


Figure 20. End of draw rod with typical seed assembly mounted in place.



Figure 21. View of the crucible/die setup as seen through the window in the copper cooling jacket.

growth process is in operation. To facilitate the view of the growing crystal and meniscus film, a small ophthalmic telescope has been attached to the framework outside the Pyrex container and is positioned to allow viewing through the cooling jacket window.

The Support Structure

The structure which supports the containment chamber assembly is a stripped down Baldwin long stroke mechanical tensile test machine. This tensile test machine provides a rigid, massive support framework which tends to minimize incoming mechanical vibrations that might perturb the growth interface. Also, the chamber assembly sits on an inner framework that "floats" on springs attached to the main chassis of the tensile test frame. This further aids in reducing mechanical vibrations entering the system. A crossbar mounted on two 2 in. diameter worm gears that are located on either side of the frame moves vertically up or down depending on the direction of rotation of the worm gears. This crossbar has the draw rod mounted in its center and acts to move this rod up and down through the water-cooled O-ring seal in the top end plate. By controlling the movement of this crossbar the seed crystal can be positioned on the die and the pull velocity, V_p, of the growing crystal controlled.

The original motor on the tensile test machine has been replaced by a one-quarter horsepower D. C. electric motor

capable of a maximum speed of 1725 r.p.m. in continuous service. This motor has been geared down through a multiple assembly gear train with two selectable ranges. One range gears the motor down 18,850:1 and by switching out a 10:1 reduction gear box, the second range is entered which gears down the motor 1885:1. At these gear reductions the motor smoothly drives the two worm gear shafts which move the crossbar. The worm gears have a pitch of 0.5 in. per revolution. This gear train arrangement permits a consistent velocity of pull anywhere in the range of 0.5 cm/hr to 70.7 cm/hr. The motor speed control unit has a 15 turn precision potentiometer control dial which allows pull velocities accurate to 0.1 percent in the range 0.5 cm/hr to 45.0 cm/hr.

The crystal growth unit may be operated in either vacuum, controlled gas atmosphere (e.g., H_2, N_2, Ar, CO/CO_2), or open air. For vacuum operation, a Kenny model KD-30 vacuum pump is attached to the chamber assembly through a fitting in the bottom end plate. Vacuums of 0.001 torr have been attained in the present setup using this pump. However, the pump's primary use to date has been to purge the chamber of air before backfilling with a selected gas atmosphere.

A special furnace was constructed to reduce the amount of oxygen in the inert atmosphere tank gases used in the crystal growth experiments; see Figure 22. This furnace consists of a 3.8 cm diameter, 61 cm long sealed

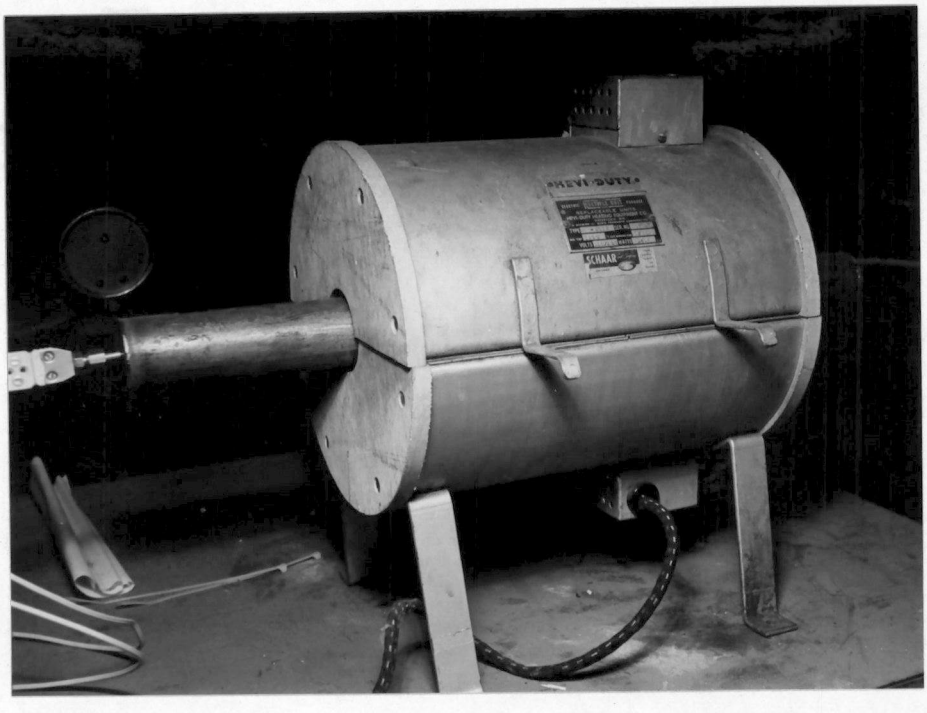


Figure 22. Furnace containing copper wool which was used to reduce the oxygen content in the inert atmosphere tank gases.

stainless steel tube packed with fine copper wool. This copper wool container is heated in a resistance type tube furnace to 350 degrees centigrade. The inert tank gases pass through this container on the way to the containment chamber. The copper reacts with the oxygen in the gases to form Cu_2O thus leaving the exiting gases lower in oxygen content than it was when it entered. The equilibrium P_{02} for the reaction $4Cu + O_2 = 2Cu_2O$ at 350 degrees centigrade is 10^{-21} atmospheres.

For an atmosphere with a specifically desired value of P_{02}, a special CO/CO_2 gas system was fabricated. It consists of two capillary/manometer flow meters linking the separate tanks of CO and CO_2 to a mixing tank which has suitable connections to the containment chamber. The flow from the tanks of CO and CO_2 is selected to give the proper CO/CO_2 ratio desired. The gases mix together in the mixing tank forming a homogeneous gas mixture. This mixture then flows into the containment chamber. In this manner the P_{02} of the gas over the melt is selected and controlled.

IV. CRUCIBLE AND DIE DESIGNS

Several dies with various configurations of growth surfaces were fabricated to investigate the EFG processes' shape producing capabilities. The dies were designed such that crystals of the following cross-sectional shapes could be grown; (1) thin ribbon shaped crystal, (2) circular tube shaped crystal, (3) square U-shaped channel crystal, and (4) airfoil shaped crystal. A complete overview showing which dies, crucibles, and melt materials were utilized in this study is given in Table I.

The thin ribbon shape die was fabricated and tested first because basic simplicity of shape was sought to minimize die shape problems associated with the actual growth of the crystal; see Figure 23. Also, the limited availability of platinum metal somewhat dictated that this die shape be chosen. The capillary die piece itself was fabricated by uniformly pressing a 4 cm long section of 0.64 cm platinum tube to a piece measuring 4 cm by 0.95 cm by 0.15 cm. This left a 0.81 cm by 0.06 cm capillary slot in the flattened tube which allows liquid to feed the 0.94 cm by 0.15 cm top surface of the die. The die top surface has the shape of a long rectangle with rounded ends attached to it. The surface is flat and polished down to a 1 micron alumina powder finish.

TABLE I

SUMMARY OF CRUCIBLE/DIE/MELT SETUPS UTILIZED IN STUDY

Crucible Material	Die Shape/Material	Melt Material
Nickel	Circular tube/ Nickel	LiF
Nickel	U-shape channel/ Nickel	LiF
Nickel	Airfoil shape/ Nickel	LiF/CaF_2 eutectic
Platinum	Thin ribbon/ Platinum	V_2O_5

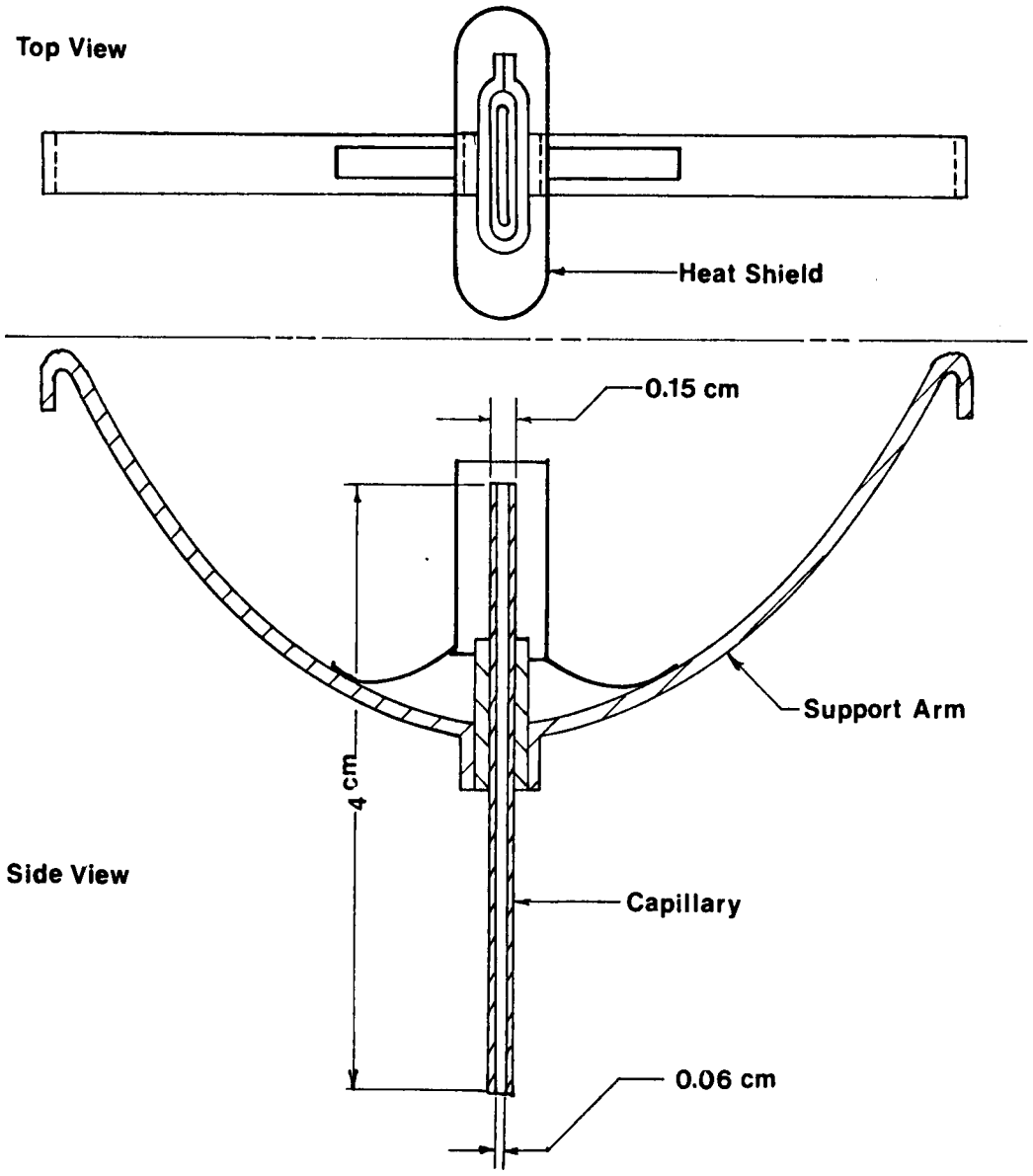


Figure 23. Schematic diagram of platinum thin ribbon shape die. Scale 2:1.

The crucible is covered with a 0.05 cm thick sheet of platinum metal which has a hole in its center to allow the die to be accessible to the seed crystal; see Figures 24 and 25. A slot 1.3 cm wide was cut into the cover to allow visual observation of the meniscus film during growth. This cover was added to help stabilize the melt temperature and make it less senstive to fluctuation in the power input. The die itself has a heat shield surrounding its uppermost portion. This small heat shield was introduced to even out and stabilize the temperature of the die top. No steady-state stable growth was achieved off of this particular die until the small heat shield surrounding the die top was added. The die is supported and held in position by two platinum metal arms which are spot welded to the die and hook over the top edge of the crucible. The arrangement of the supporting arms hooking over the top edge of the crucible is common to all the crucible/die setups and is employed for two reasons. The first reason is that any contact area between die assembly and crucible that may possibly weld together is easily accessible for repair, and the second is that any time the growing crystal freezes to the die, it may be quickly observed when the die support arms lift off of the crucible lip. Due to the very thin meniscus films involved during crystal growth, this method of determining when the crystal has frozen to the die is most useful.

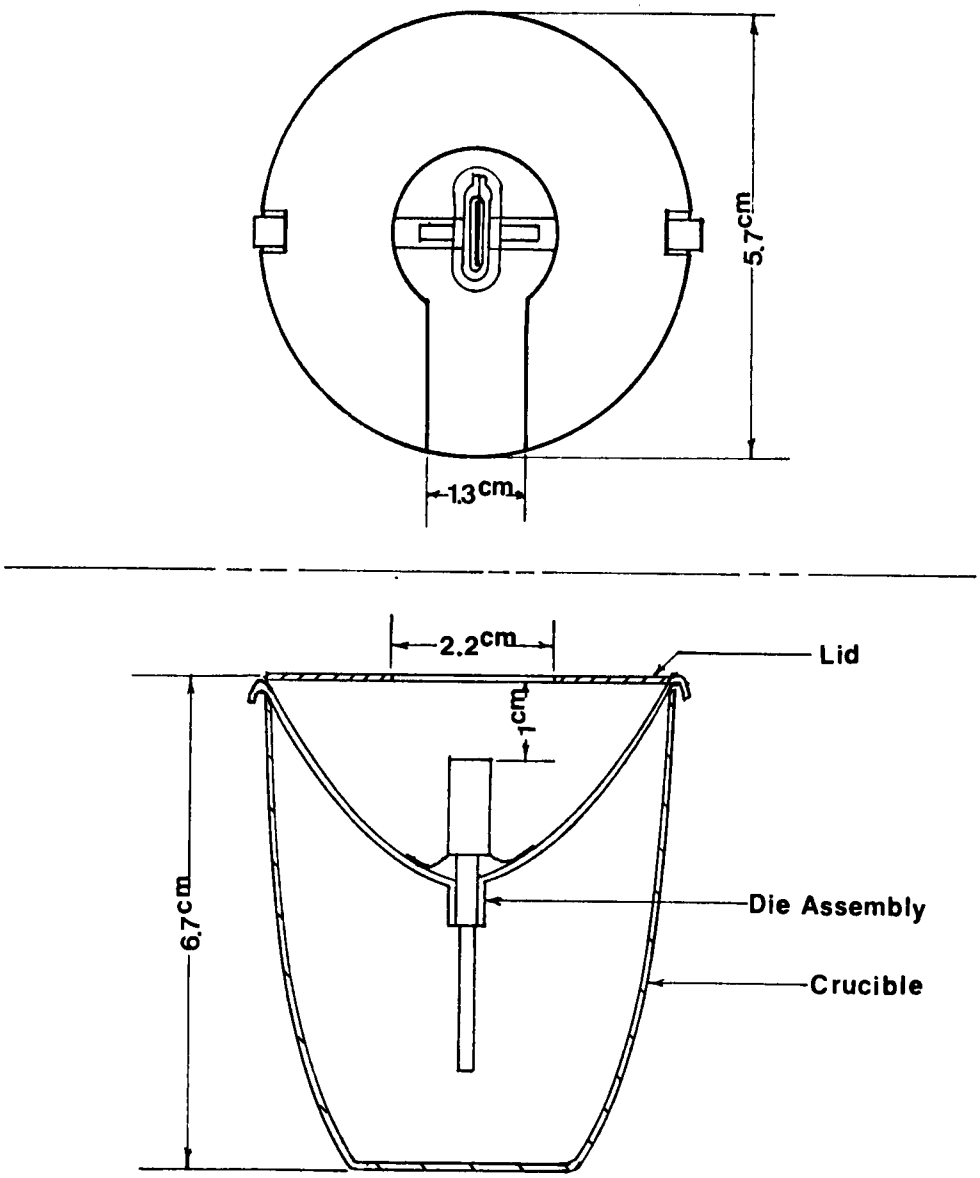


Figure 24. Schematic diagram of thin ribbon shape die and crucible assembly. Scale 1:1.



Figure 25. Crucible/die setup of the platinum thin ribbon shape die and platinum crucible.

The circular tube shape die was fabricated to demonstrate the EFG processes' capabilities in producing tubular crystals. The die itself consists of two concentric axially symmetric pieces fitted together to produce an annular capillary of 1 mm width that feeds a 3 mm wide 0.64 cm inside diameter growth surface; see Figure 26. The inner and outer growth surfaces are beveled downwards towards the annular capillary slot. The slope of this bevel is 30° from the horizontal and is present to enhance the spreading of the meniscus film out to the edges of the die surface. The nickel crucible used in conjunction with the circular tube shape die is shown schematically in Figure 27. The die assembly has a small heat shield surrounding its growth surface and there is no top cover piece on the crucible as was used in the previous ribbon shape crucible/die setup; see Figures 26 and 28. The thermal mass of the nickel crucible, circular tube shape die, and LiF melt in the present setup was found to be sufficiently great to damp out thermal fluctuations which tended to disrupt steady-state growth in the case of the thin ribbon shape die. It was also determined through an experimental malfunction that the heat shield around the top of the die was unnecessary. During one experimental run in which the melt level was excessively high, a portion of the growing crystal spread over the outside edge of the die and began growing off of the liquid that had risen up between the die and the heat

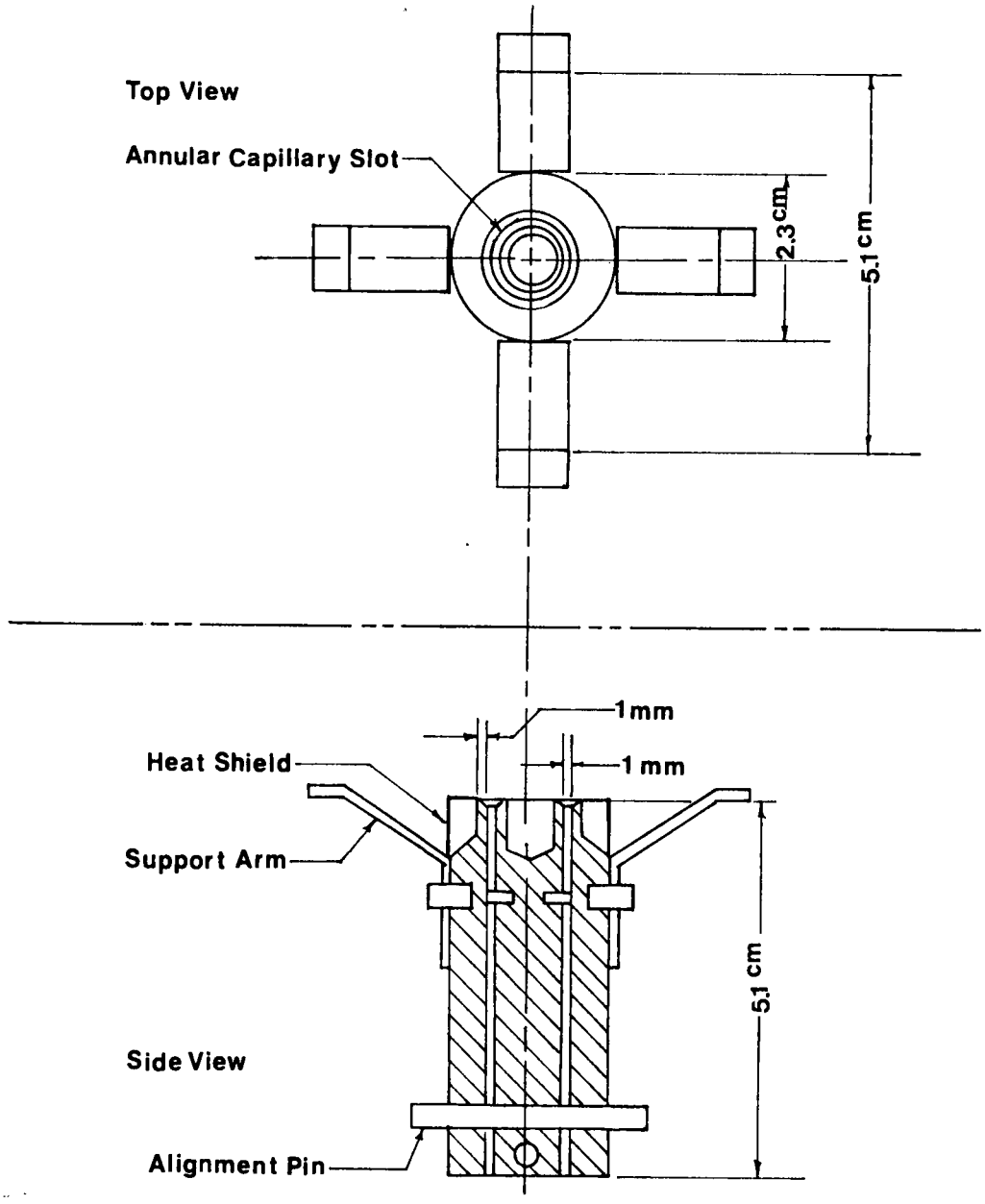


Figure 26. Schematic diagram of nickel circular tube shape die. Scale 1:1.

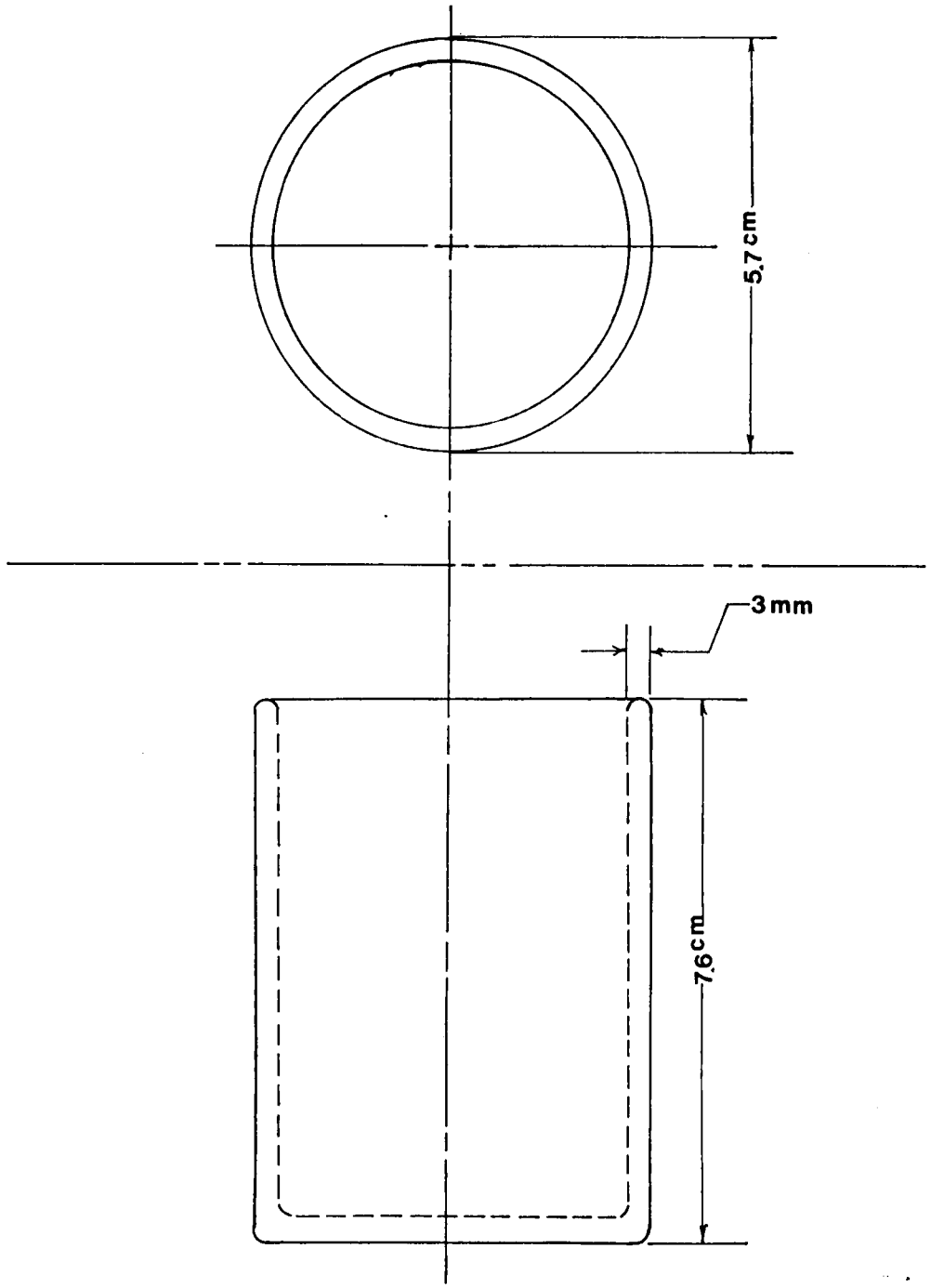


Figure 27. Schematic diagram of nickel crucible used in conjunction with the nickel tube shape die. Scale 1:1.



Figure 28. Crucible/die setup of the nickel circular tube shape die and nickel crucible.

shield. This part of the crystal continued to spread across the fluid separating the die and heat shield until it reached the heat shield. Upon reaching it, the crystal froze to the heat shield, and it was subsequently lifted completely free of the die assembly by the upward motion of the growing crystal. With some minor adjustments in power input, stable growth was maintained and the run completed successfully.

A U-shape die with square corners was designed and fabricated to study the effects of a nonuniform heat flow die and the ability to grow crystals with sharp right angle bends. The growth surface of the die is fed by a 0.05 cm wide capillary slot which extends across the front and down both sides of the die; see Figure 29. The area the film covers during fully wetted steady-state growth is 2.8 cm long by 0.15 cm wide. As in the circular tube shape crucible/die assembly, the U-shape channel die has a heat shield mounted on its uppermost portion; see Figure 30. The crucible/die setup is devoid of any crucible cover. The small heat shield proved to be superfluous in this case. It was also lifted from the die during a growth run and stable growth was maintained up to a 15.00 cm/hr pull rate. The inside and outside growth surfaces are beveled towards the capillary slot at an angle of 45°.

The airfoil shape die was fabricated for use in growing multiphase eutectic composition fluoride crystals. The shape

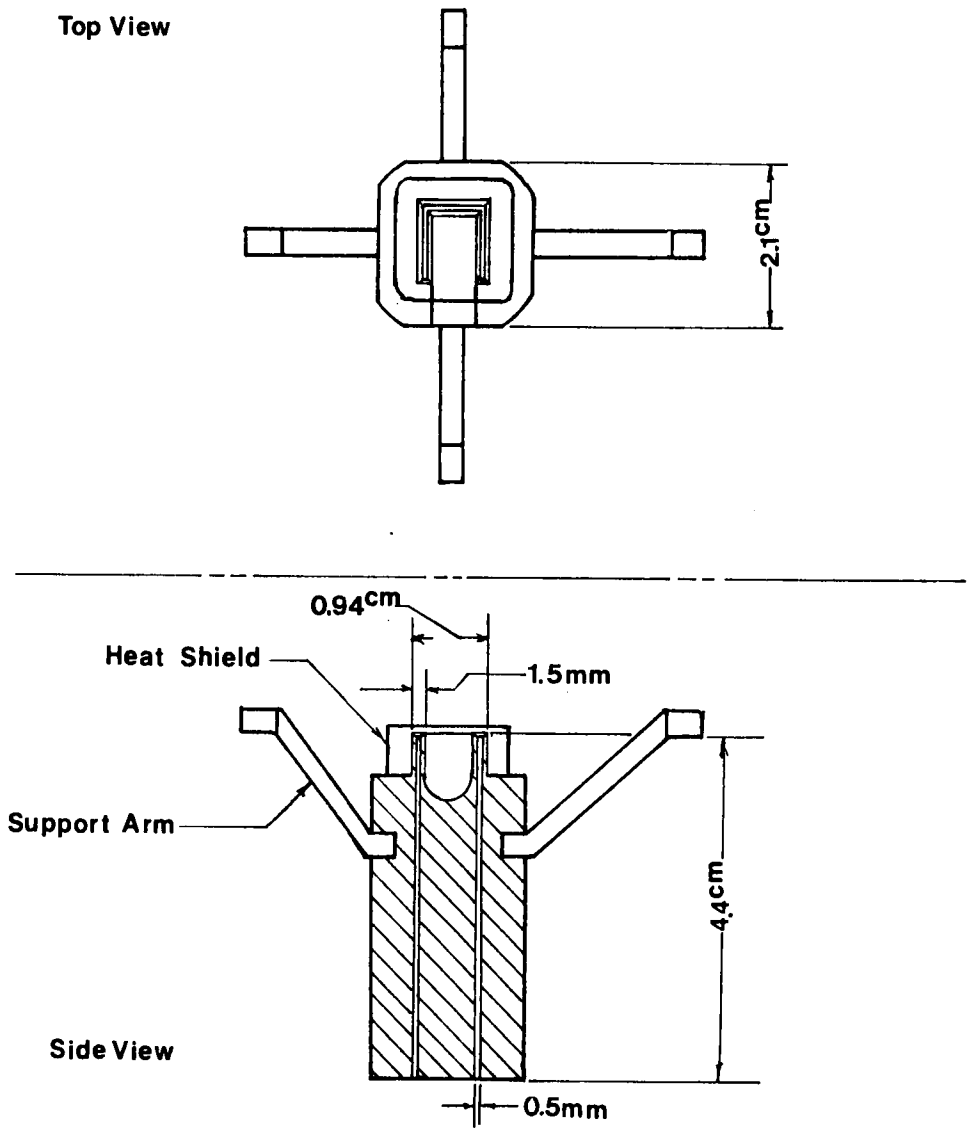


Figure 29. Schematic diagram of nickel U-shape channel die. Scale 1:1.

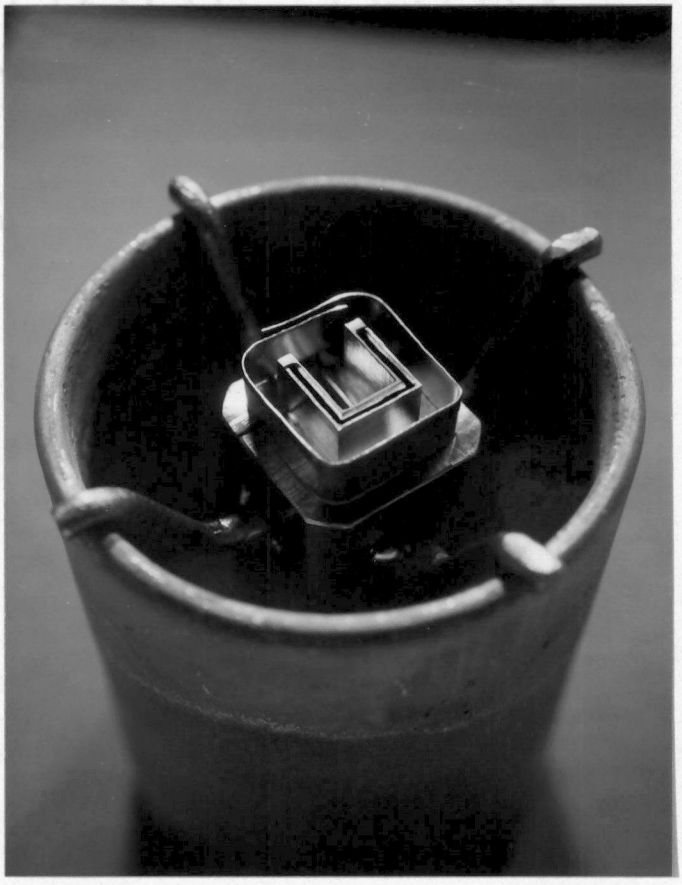


Figure 30. Crucible/die setup of nickel U-shape die and nickel crucible.

of the die itself provides for study of a practical engineering shape where varying curvature and die width are important factors. The capillary which allows fluid to feed the meniscus film on this die is a single 0.15 mm diameter hole in the die. It is placed 0.24 mm off center towards the leading edge of the airfoil shape; see Figure 31. This is a departure from the three previous dies discussed which had capillary slots rather than holes. Figure 32 is a schematic drawing of the nickel crucible used with the airfoil shape die and the LiF/CaF_2 eutectic composition melt. Figure 33 shows the airfoil shape die and crucible as they were during the growth run. The die top is surrounded by a heat shield and the crucible has no top cover. This crucible/die setup is smaller in size and thermal mass than two of the previous crucible/die setups, yet the lack of a top cover was not a hindrance in growing crystals. The top surface of the die has been ground flat and smooth. No beveling of the top surface towards the capillary hole has been employed here.

All of the crucible/die setups discussed are mounted in refractory crucibles before being placed in the EFG unit. Figure 34 shows a typical assembly of a silica outer beaker, a molybdenum heat shield, and an inner ZrO_2 or MgO crucible with various ZrO_2 spacer rings. The ZrO_2 fiber packing was utilized only with the airfoil shape die and crucible setup. In all other crucible/die setups an empty space exists where the ZrO_2 fiber packing is shown.

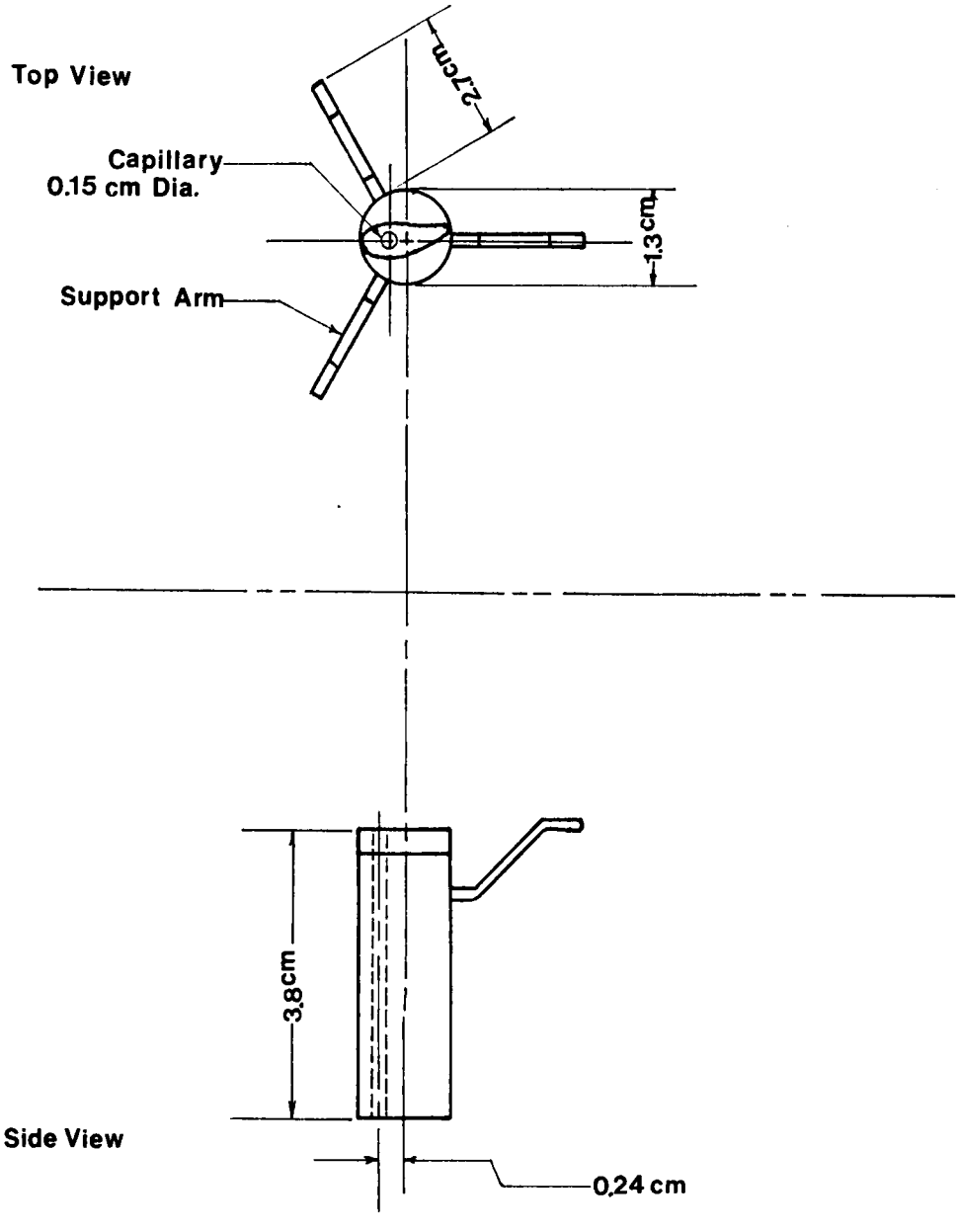


Figure 31. Schematic diagram of nickel airfoil shape die. Scale 1:1.

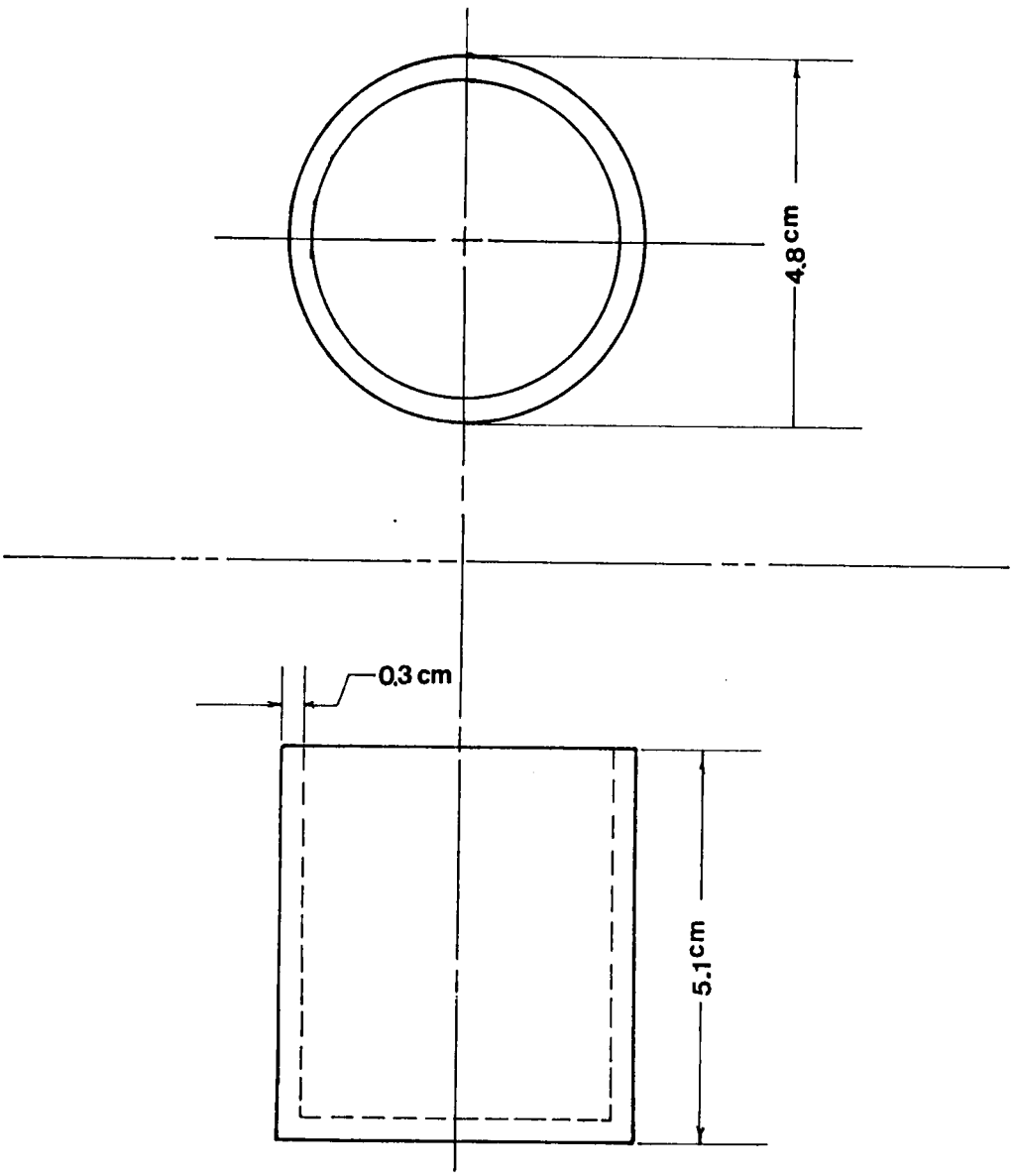


Figure 32. Schematic diagram of nickel crucible used in conjunction with the nickel airfoil shape die. Scale 1:1.



Figure 33. Crucible/die setup of the nickel airfoil shape die and nickel crucible.

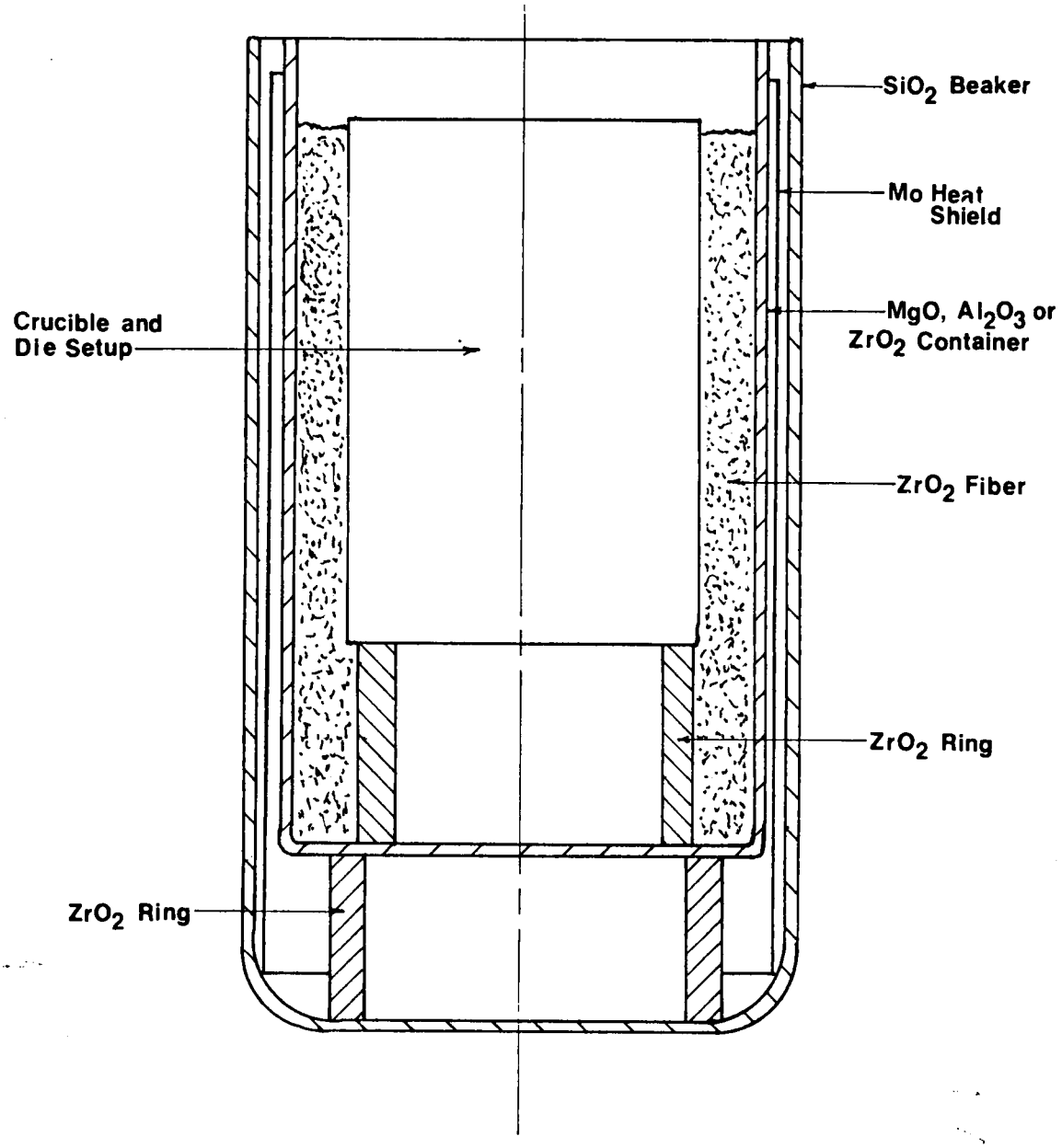


Figure 34. Schematic diagram of the refractory containers used to house and insulate the crucible/die setups during the growth runs. Scale 1:1.

V. WETTABILITY OBSERVATIONS

Observations were made of the wetting angles exhibited by all of the molten materials in contact with their respective die materials that were considered in this study. The wetting angles of the fluoride compounds were observed on a carefully polished surface of a 1 inch diameter nickel bar mounted in a levitation zone refiner. The bar was of the same composition as the nickel dies and the polished surface of roughness like that of the die top surfaces. The fluoride, initially a 5 gm̀ charge of powder, is placed on the end of the nickel bar. The bar is then inductively heated in an atmosphere of tank argon until the fluoride melts. After the temperature has stabilized and an optical temperature measurement made, a camera is moved into position in front of the viewing port of the zone melter. The camera was adjusted so that the line of sight of the lens is in the plane of the top surface of the nickel bar; see Figure 35. Pictures were then made of the fluoride droplets resting on the nickel surface. The film used was fine grained Panatomic-X so that high resolution enlargements of the solid-liquid-vapor junctions may be made and a good approximate wetting angle measurement taken.

The LiF droplet, see Figure 36, spread to the outer edge of the surface completely covering the end of the nickel bar. The LiF/CaF_2 eutectic formed many droplets on the surface;

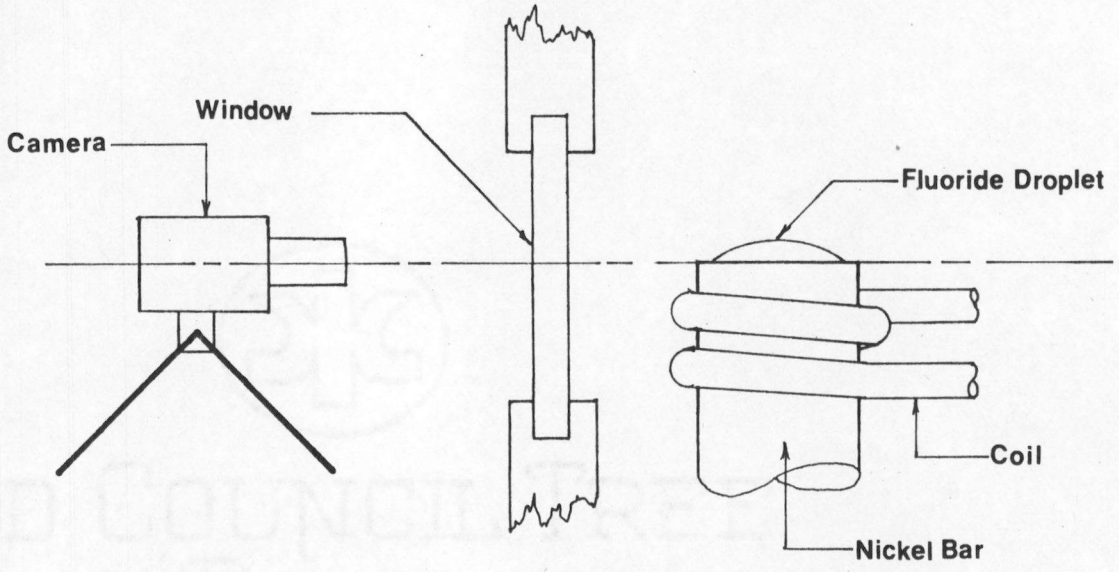


Figure 35. Schematic diagram of experimental setup for measuring wetting angles of molten fluorides on nickel.

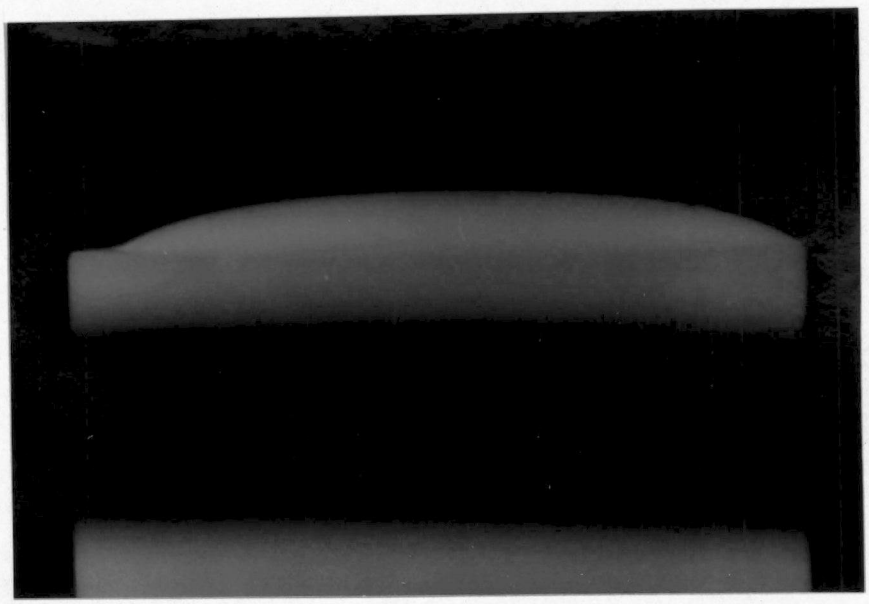


Figure 36. Molten LiF on nickel surface.

see Figure 37. Not all the nickel surface was covered by the eutectic droplets. It was noted that the wetting angle of this binary eutectic liquid decreased with time during the observation experiment. This decrease in wetting angle corresponded to the formation fo a light oxide film on the nickel bar. Apparently the LiF/CaF_2 eutectic can more readily wet an oxidized nickel surface than it can a clean nickel surface. The LiF/CaF_2 eutectic wetting angle recorded is that taken after oxidation occurred and the wetting angle of the droplets decreased.

The $LiF/CaF_2/SrF_2$ ternary eutectic liquid exhibited a wetting angle so large, see Figure 38, that it was dropped from consideration as a candidate material for EFG experiments. It was decided that the high wetting angle was an excessive inhibition to spreading and coverage of the die top surface.

The wetting angle of V_2O_5 on platinum was measured in air. An 8 gm quantity of V_2O_5 was placed on a flat, polished piece of platinum metal which was heated with a gas-oxygen torch above the melting point of V_2O_5. A camera was then introduced and a picture of the liquid droplet resting on the platinum was made; see Figure 39. The droplet of V_2O_5 spread completely over the platinum sheet stopping only when it reached an outside edge. The wetting angle was measured at the edge of the platinum piece.

The complete results of the wetting angle measurements for all the cases discussed above are given in Table II.

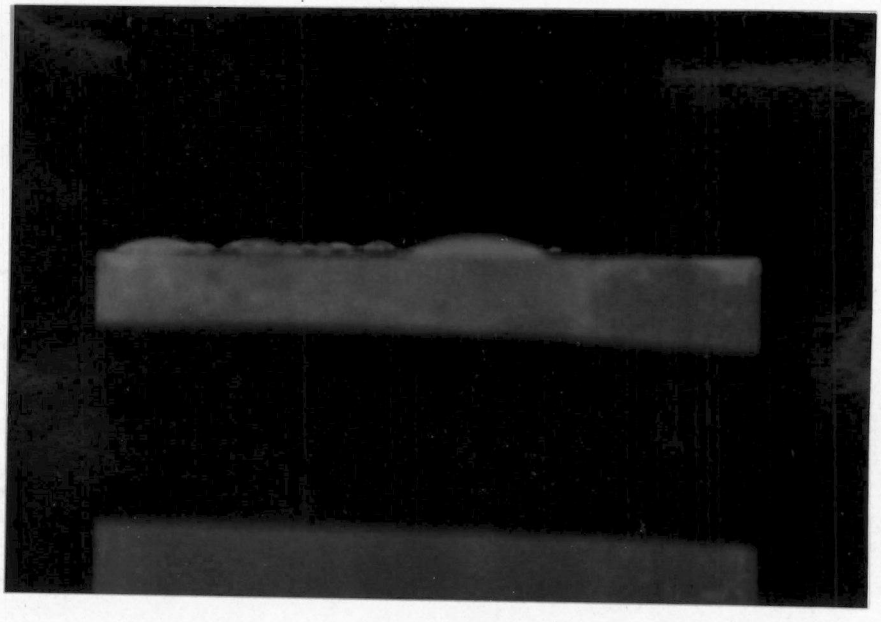


Figure 37. Molten LiF/CaF_2 droplets on nickel surface.

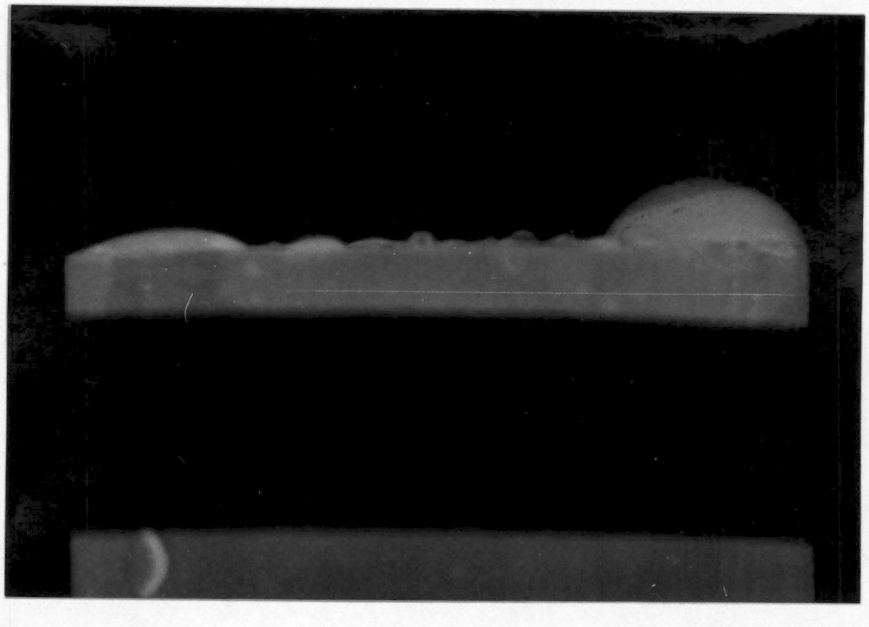


Figure 38. Molten $LiF/CaF_2/SrF_2$ droplets on nickel surface.



Figure 39. Molten V_2O_5 on a platinum surface.

TABLE II

RESULTS OF WETTABILITY EXPERIMENTS

Die Material	Melt Material	Temperature (°C)	Atmosphere	Wetting Angle
Nickel	LiF	860	Argon	≈18°
Nickel	LiF/CaF_2 eutectic	810	Argon	≈27°
Nickel	LiF/CaF_2/SrF_2 eutectic	790	Argon	≈70°
Platinum	V_2O_5	720	Air	≈ 8°

VI. RESULTS

In this section the results of all successful growth experiments are discussed. Shaped crystals of V_2O_5, LiF, and LiF/CaF_2 were grown using platinum and nickel dies respectively. Discussion of each will be taken in the order given above.

V_2O_5 Ribbon Shaped Crystals

Orthorhombic[23] V_2O_5 was chosen as a candidate for EFG for several reasons. First of all, it is a brittle material in the solid state and it was of interest to study the use of the EFG process in generating shaped brittle materials. It is an oxide which is of interest since oxides of higher melting point have considerable engineering applicability and thus it is worthwhile to determine how oxides behave during edge-defined, film-fed growth. V_2O_5 is a low melting point material which makes it convenient to grow and work with. It has an α-factor[24] in the range $4.1 \leq \alpha \leq 8.1$, indicating that it would exhibit faceted growth. It was of interest to observe the behavior of a material which solidifies in a faceted manner as it grows by the EFG process. V_2O_5 readily wets platinum metal and does not grossly react with it over the time spans involved in the crystal growth experiment. Therefore platinum could be used as a die material and the wettability and compatibility criterion are met. Some

physical constants of V_2O_5 that are of interest are listed in Table III.

All of the growth runs using V_2O_5 and a platinum crucible/die setup were performed in open air. The only shape grown was that of a thin ribbon measuring 0.95 cm by 0.15 cm in cross section with ends rounded to a 0.075 cm radius. The crucible/die setup was previously discussed in detail; see Figure 23, page 62, and Figure 25, page 65.

The seeding operation used in this study was somewhat different from the previously described method of using the seed crystal to draw the liquid out of the capillary and onto the die top surface as shown in Figure 5, page 11. The procedure used with the V_2O_5 crystal growth runs was to bring a V_2O_5 seed crystal, which had dimensions exceeding the width of the capillary slot, into direct contact with the top of the die. The temperature is adjusted so that a small portion of the end of the seed crystal touching the die melts and establishes intimate contact between the liquid in the capillary and the seed. The temperature is then adjusted to partially refreeze the molten drop until a thin film is established between the top of the die and the seed. Once the meniscus film has been established, upward pull is initiated on the seed crystal at a slow rate (0.5 cm/hr $\leq V_p \leq$ 2.0 cm/hr) until the film spreads completely over the top surface of the die. This method of establishing a

TABLE III

SOME PHYSICAL AND THERMODYNAMIC PROPERTIES OF V_2O_5

Property	Symbol	Value	Units	Reference
Density of Solid	ρ_s	3.357	g/cm^3	25
Density of Liquid	ρ_ℓ	2.58	g/cm^3	
Melting Point	T_m	690	°C	25
Heat of Fusion	ΔH_f	15,560	cal/g. mole	26
Spec. Vol. Increase upon Melting	$\Delta \bar{V}_f$	30	%	27
Linear Coeff. of Thermal Expansion	α	13.0×10^{-6}	$°C^{-1}$	28
Molecular Weight	M.W.	181.88	a.m.u.	25
Color		red		25

meniscus on top of the die and subsequently spreading it to the outer edges of the die was used in all of the crystal growth experiments in this investigation.

Once complete or nearly complete wetting is achieved, the establishment of steady-state growth at a particular velocity is strived for. After a given velocity of growth was maintained and a crystal grown at steady-state for a suitable time period, the velocity of growth was changed. Stable growth was then sought at the new growth velocity and, if achieved, another section of crystal was grown. This sequence of establishing steady-state growth at one growth velocity, then changing the growth velocity and reestablishing steady-state conditions was repeated until (1) the limit of the draw stroke of the crystal puller was reached, approximately 24 cm, or (2) steady-state conditions could not be maintained. The sequence described above is one common to all growth experiments herein discussed.

The first successful growth run on the EFG unit produced V_2O_5 ribbon shaped sample 108; see Figures 40 and 41. Each section denoted by a capital letter in Figures 40 and 41 indicates a region grown at a particular velocity, V_p. Each primed letter indicates a point where the sample froze to the die and it was necessary to stop the pull and reestablish a stable meniscus film. Table IV correlates the velocities of growth and distances grown with each of the

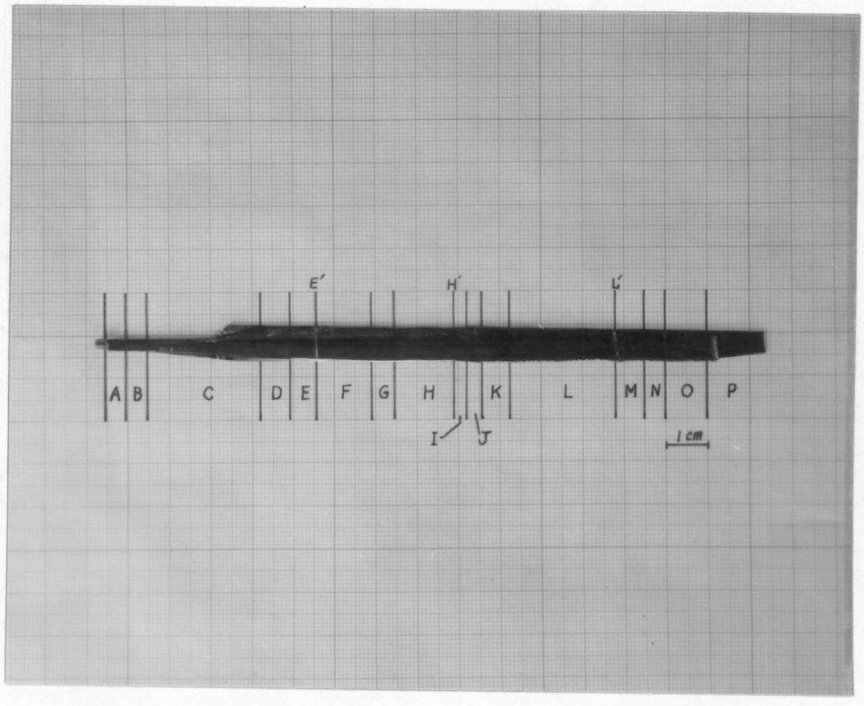


Figure 40. V_2O_5 sample 108, side view.

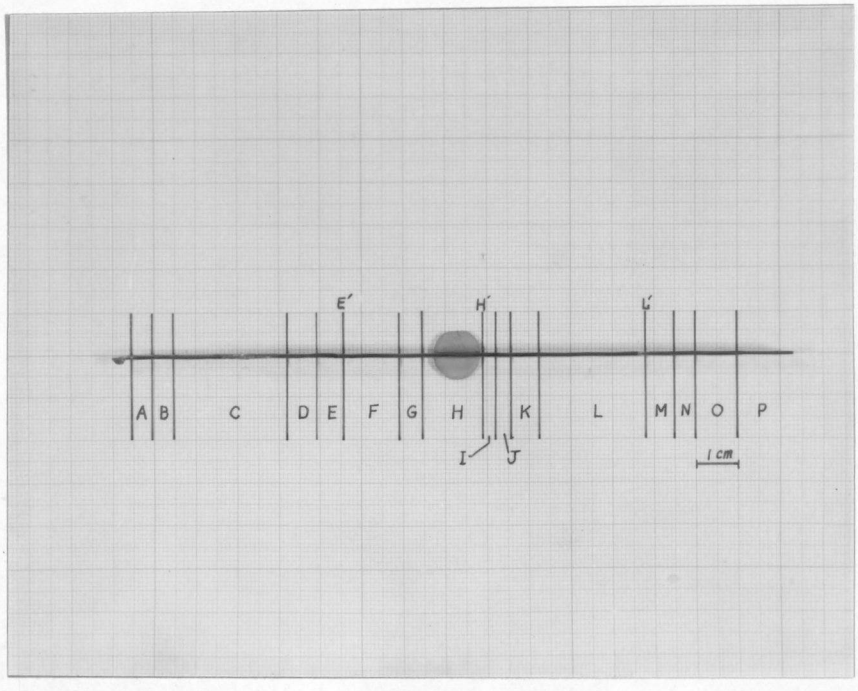


Figure 41. V_2O_5 sample 108, edge view.

TABLE IV

CORRELATION OF THE DENOTED REGIONS OF V_2O_5 SAMPLE 108 SHOWN IN FIGURE 40 WITH THE GROWTH VELOCITIES AND DISTANCES GROWN IN THOSE SECTIONS

Section	Growth Velocity (cm/hr)	Distance Grown (cm)
A	2.55	0.77
B	2.15	0.43
C	2.55	2.64
D	3.12	0.73
E	2.55	0.85
F	2.15	2.22
G	2.55	0.43
H	2.15	1.47
I	3.10	0.20
J	2.15	0.25
K	1.00	0.45
L	4.30	2.65
M	5.65	0.75
N	6.80	0.68
0	9.00	0.90
P	15.00	1.38

sections denoted in Figure 40, page 87. V_2O_5 sample 108 was the only successful growth run made prior to the installment of the fine power control on the Lepel unit. Control over the freezing interface was not very good as is evidenced by the repeated freezeups. The freezeups were quite detrimental in that during the necessary remelt and recontact procedure, the die was knocked loose from its support and tilted slightly. The angle of tilt becomes progressively worse with each freezeup. From the angle of the striations on the sides of V_2O_5 sample 108 relative to the pull direction, the angle of tilt was on the order of 10 to 12 degrees after the last freezeup at the point L', Figure 40, page 87.

V_2O_5 sample 108 consisted of 4 columnar grains, one of which is almost eliminated by competitive growth. These grains were oriented lengthwise in the growth direction of the crystal. The largest of these grains measures 3 mm in width. The grains growing at the edges of the ribbon sample clearly exhibit faceted surfaces which are evidently (010) planes. The sample was mechanically fractured and found to cleave quite easily on planes parallel to the faceted surfaces formed during growth. The (010) plane is reportedly[23] an easily cleaved plane in the orthorhombic V_2O_5 and it appears that this is also the plane exhibiting faceting during crystal growth. The faceted surfaces in

sample 108 are parallel to the growth direction and perpendicular to the sides of the crystal. This particular orientation of the faceted planes only slightly inhibited good edge definition at the rounded ends of the sample.

After the fine power control was installed, a new seed crystal was made and a second V_2O_5 sample, 146, was grown by the EFG process; see Figures 42 and 43. As before, the distances marked with capital letters refer to a velocity at which a particular section of sample was grown. The primed letters refer to a location where the sample froze to the die during the run. Table V correlates the growth velocities and distances grown to the respective areas denoted in Figure 42.

The orientation of the facet planes in sample 146 is parallel to the growth direction and at an approximate angle of 15 degrees to the side of the crystal. The entire surface of sample 146 exhibits a faceted morphology, not just at the ends as was the case in sample 108. The quality of the edge definition in sample 146 was limited by the abundant faceting of its surface. The sides of the sample would grow to the edge of the die yet the facets would retain their identity and only one corner of each facet ledge would maintain a position directly over the edge of the die; see Figure 44. Thus the outer edge of the crystal does not exactly conform to the die edge and is only a rough approximation of the die shape. The very faceted sample 146, did, however, exhibit greater

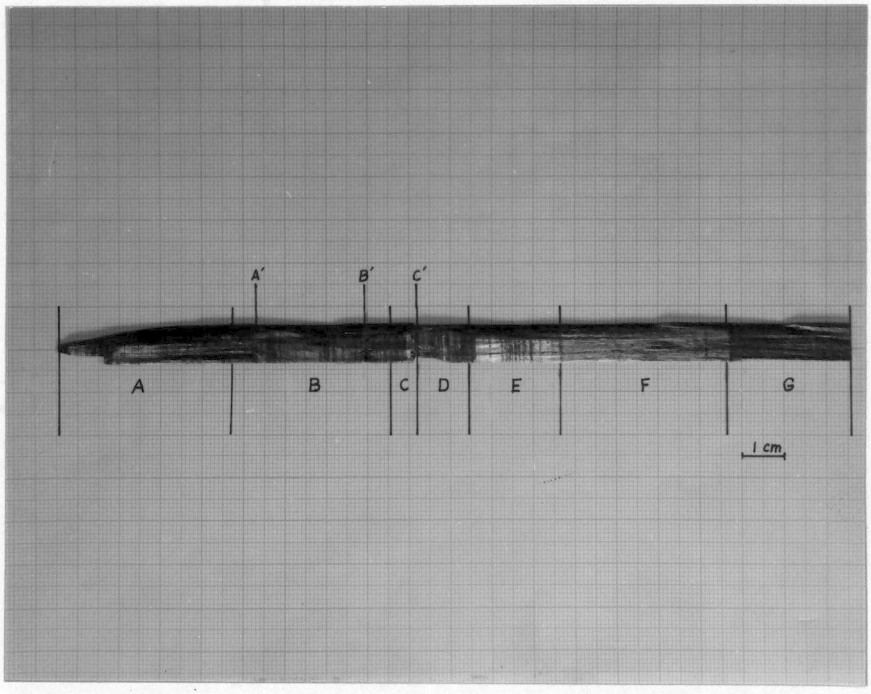


Figure 42. V_2O_5 sample 146, side view A.

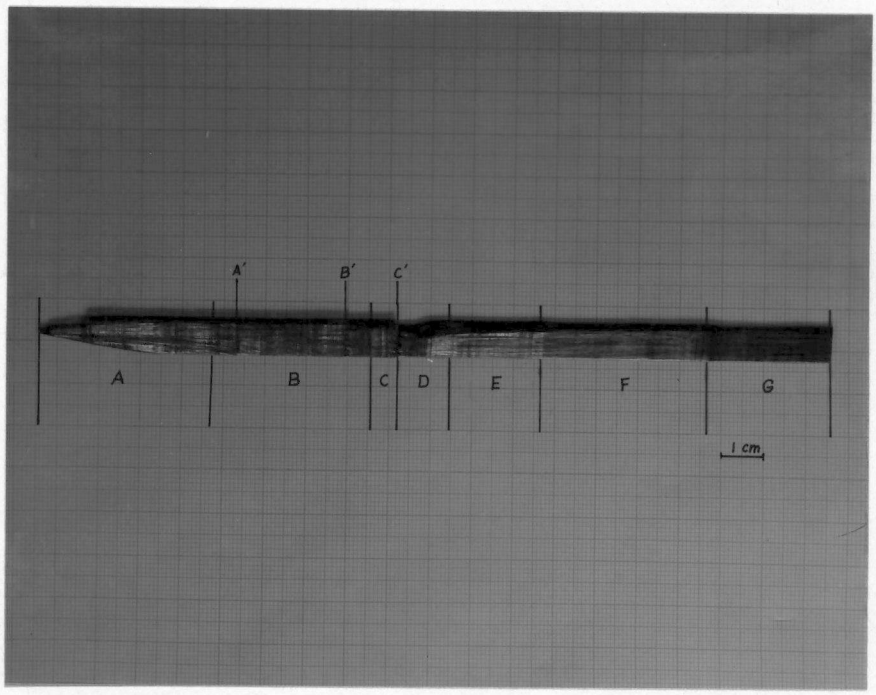


Figure 43. V_2O_5 sample 146, side view B.

TABLE V

CORRELATION OF THE DENOTED REGIONS OF V_2O_5 SAMPLE 146 SHOWN IN FIGURE 42 WITH THE GROWTH VELOCITIES AND DISTANCES GROWN IN THOSE SECTIONS

Section	Growth Velocity (cm/hr)	Distance Grown (cm)
A	2.00	4.00
B	3.00	3.90
C	5.00	1.10
D	3.00	1.50
E	5.00	2.15
F	10.00	4.05
G	15.00	3.00

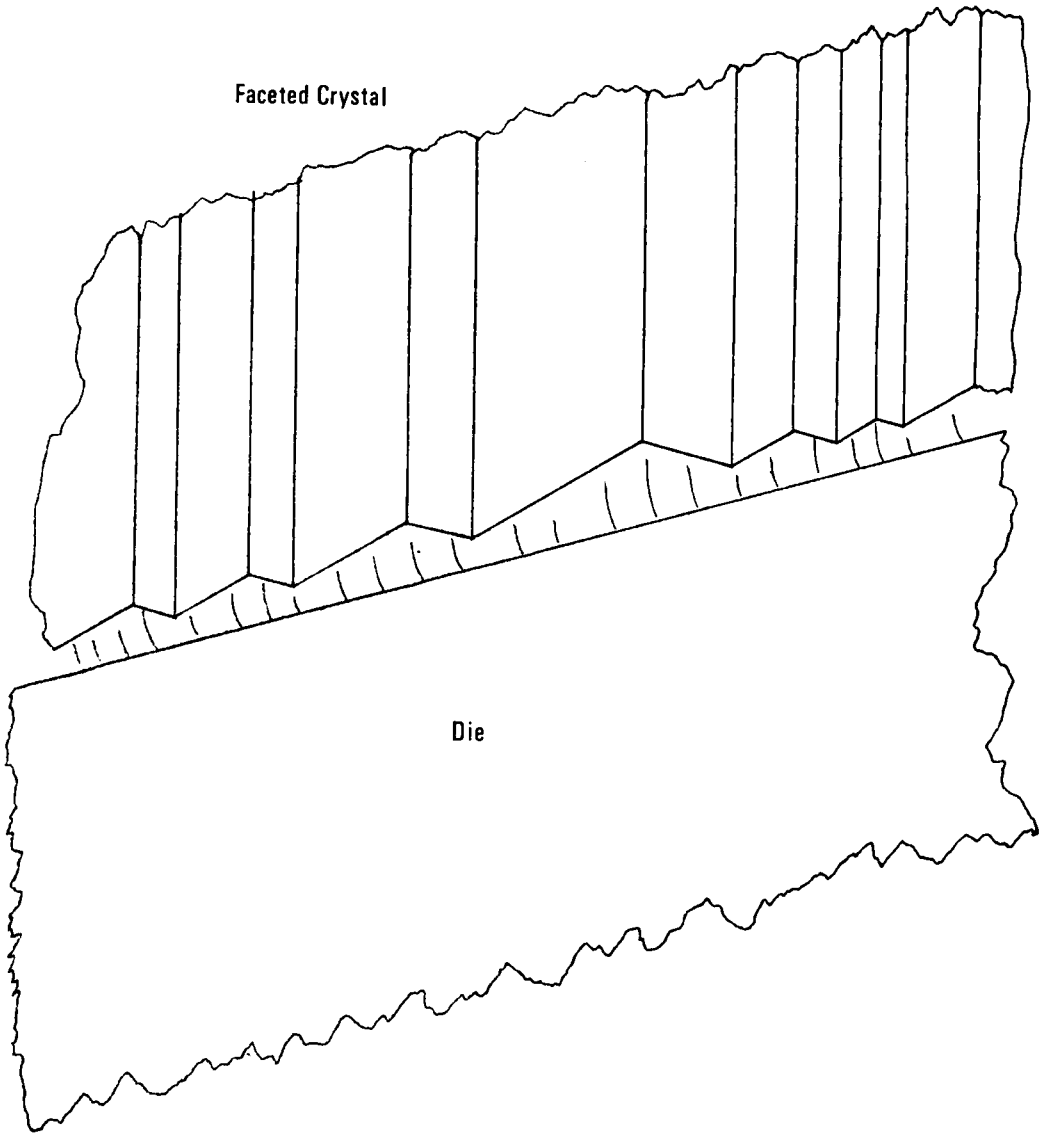


Figure 44. Schematic diagram of faceted surface of crystal growing adjacent to die edge.

shape stability than the other samples grown. As the pull velocity was increased to 15.00 cm/hr, sample 146 maintained nearly complete wetting of the die, did not recede from the die ends and did not undergo a reduction in the thickness dimension.

A third growth run emphasized growing the V_2O_5 crystal at the high end of the velocity growth range. The majority of V_2O_5 crystal 151 was grown at 10.00 and 15.00 cm/hr; see Figure 45. The capital letters denote regions grown at a certain velocity and the numbers refer to a point where the crystal froze to the die. Table VI correlates the designations in Figure 45 to the growth velocities and distances grown. Faceting during growth took place after the freezeup designated at point 3 in Figure 45. One end of the platinum die was completely wetted by the meniscus film. The other edge of the growing crystal was positioned approximately 65 percent of the total die width away from the first. This edge was composed of a facet surface parallel to the growth direction and at an angle of 30 degrees to the side of the crystal and die. This faceted surface is of particular interest because it maintained its position and identity from 0.5 cm down from the freezeup at point 3 until the end of the run. Despite attempts to induce the faceted surface to spread completely across the die by varying the die temperature, it persisted in growing in a steady-state

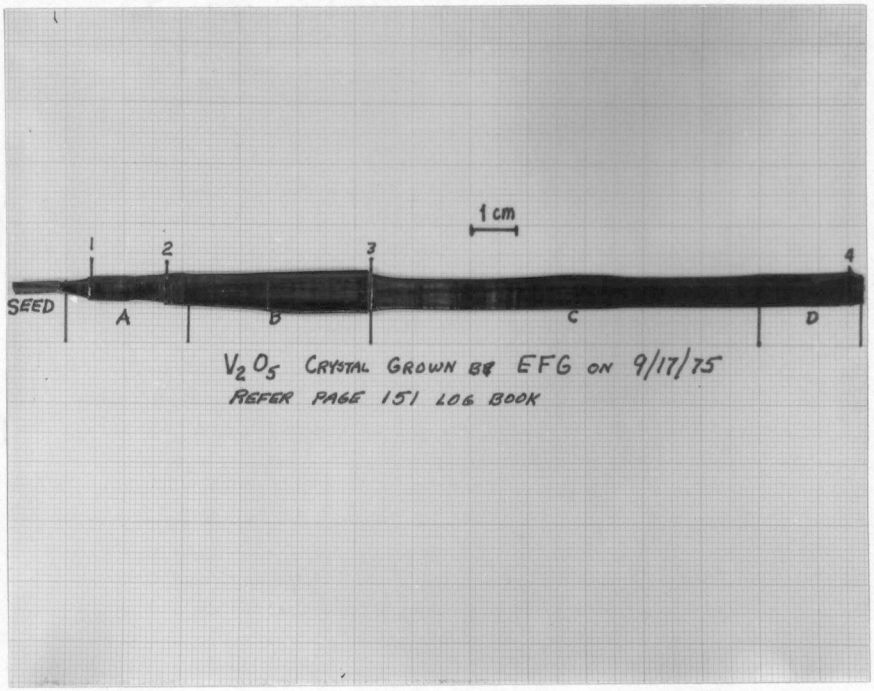


Figure 45. V_2O_5 sample 151, side view.

TABLE VI

CORRELATION OF THE DENOTED REGIONS OF V_2O_5 SAMPLE 151 SHOWN IN FIGURE 45 WITH THE GROWTH VELOCITIES AND DISTANCES GROWN IN THOSE SECTIONS

Section	Growth Velocity (cm/hr)	Distance Grown (cm)
A	4.00	2.20
B	10.00	3.18
C	10.00	6.72
D	15.00	1.70

fashion. The portion of the meniscus film from which the faceted edge of crystal 151 was growing was clearly observable and different in shape from the meniscus film feeding the remaining portion of the crystal. The film in the neighborhood of the faceted edge was thicker than the remaining film. It was estimated to be approximately 1 mm in thickness, whereas the remaining film was at most only 0.5 mm thick.

Also, the shape of the meniscus at the faceted edge indicated that it was contacting the die with an angle less than that of the film that was observed during growth with edges not exhibiting faceting.

The meniscus film was very thin during the steady-state portions of all growth runs and it was quite difficult to observe its shape. Film thickness was estimated to be on the order of 0.2 to 0.5 mm when fully wetted stable growth was achieved.

LiF Shaped Crystals

Lithium fluoride was chosen as a candidate material for edge-defined, film-fed growth for several reasons. Its crystal structure is cubic and it has an α-factor[24] in the range $0.63 \leq \alpha \leq 1.26$, which implies that it may be expected to solidify in a metallic like manner. This is useful since the V_2O_5 crystals grown by EFG solidified in a faceted fashion

quite unlike a metal and a comparison of the effect of solidification modes on the process is of interest. Liquid LiF readily wets commercial purity nickel as demonstrated earlier and does not react appreciably with the nickel. Therefore, minimum problems were expected in regards to establishing a meniscus film across the entire nickel die surface. Lithium fluoride in the solid state is quite transparent to ultraviolet and infrared radiation.[29] It was thus expected that the growing crystal would act as an effective heat sink since heat from the meniscus film would be removed from the solid-liquid interface both by conduction and radiation through the crystal. The increased heat removal capacity of the material implies an enlarged capability for high growth rates. Some physical constants of LiF of interest are given in Table VII.

The first lithium fluoride sample grown was a tube shaped sample designated 182; see Figure 46. The tube sample was grown using a circular tube die. Correlation between the denoted regions in Figure 46 and their velocities of growth and distances grown is given in Table VIII.

The establishment and spreading of the meniscus film over the entire die surface occurred with ease. First, a small area of film was established between the die and the LiF seed crystal. This film suddenly spread across the area from the inside radius to the outside radius of the die surface located

TABLE VII

SOME PHYSICAL AND THERMODYNAMIC PROPERTIES OF LiF

Property	Symbol	Value	Units	Reference
Density of Solid	ρ_s	2.635	g/cm^3	25
Density of Liquid	ρ_ℓ	1.81	g/cm^3	30
Melting Point	T_m	842	°C	25
Heat of Fusion	ΔH_f	4100	cal/g. mole	25
Spec. Vol. Increase upon Melting	$\Delta \overline{V}_f$	45.6	%	
Molecular Weight	M.W.	25.94	a.m.u.	25
Color		Colorless		25
Surface Energy	γ	263 (at 1120°K)	dynes/cm	31

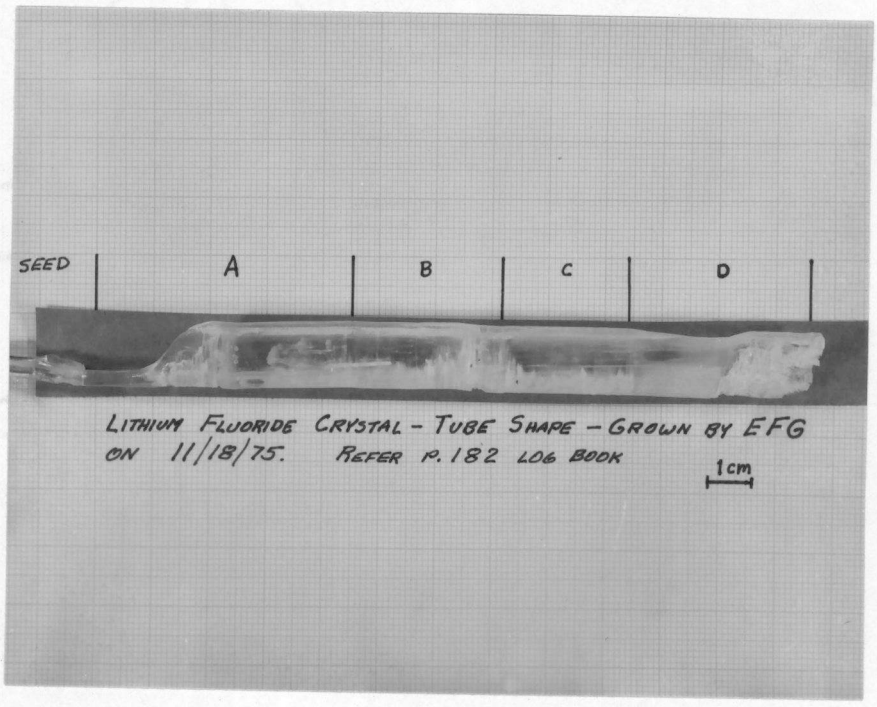


Figure 46. Lithium fluoride tube shaped sample 182.

TABLE VIII

CORRELATION OF THE DENOTED REGIONS OF LiF TUBE SHAPED SAMPLE 182 SHOWN IN FIGURE 46 WITH THE GROWTH VELOCITIES AND DISTANCES GROWN IN THOSE SECTIONS

Section	Growth Velocity (cm/hr)	Distance Grown (cm)
A	2.50	4.50
B	5.00	2.65
C	7.00	2.25
D	10.00	3.30

under the seed. As crystal growth was initiated, the crystal began spreading around the circumference of the die in both directions away from the initial seed contact point. After approximately 2 cm of sample was grown, the two pincer like ends of the spreading crystal met at a point approximately 180° from the initial seed contact point on the circumference of the die and wetting was complete; see Figure 47. Almost immediately upon achieving complete wetting, the film under the seed began going unstable and receding away from the outer edge of the die. This instability in wetting was corrected by increasing the die temperature. With this increase in temperature the film reestablished itself in a stable fashion on the outside edge of the die. The initial operation of seeding and spreading is a very transient phase of the crystal growth sequence. As the top surface of the die becomes increasingly covered with spreading meniscus liquid, its temperature drops due to the increasing capacity for the growing crystal to draw heat from the die. The quality of the first few centimeters of crystal grown during spreading was poorer (i.e., lacking in edge definition) than the remainder which was grown under conditions closely approximating steady-state. Stable growth was maintained on the crystal at velocities of 2.50 cm/hr, 5.00 cm/hr and 7.00 cm/hr with only one section, the last 1.5 cm of growth at 5.00 cm/hr in zone B, demonstrating loss



Figure 47. Spreading of the sample 182 around the circumference of the tube shape die.

of stability. This instability was caused by the die temperature being too low and was corrected by increasing it. Also, the increase in growth velocity to 7.00 cm/hr at the start of zone C acted to increase the die temperature by increasing the generation rate of latent heat of fusion and by drawing hot liquid LiF up the capillary at a faster rate. When the velocity was changed to 10.00 cm/hr, the increase in die temperature caused by the aforementioned effects became excessive. The meniscus film became too thick and edge definition was lost on one side as the outside crystal surface receded from the die edge. An effort was made to regain steady-state growth by decreasing the die temperature; however an overadjustment was made and the die became too cold. This resulted in the loss of wetting on the opposite side of the die, even as the crystal rewetted the outside edge that had previously been too hot; see Figure 48.

A second LiF tube shaped sample, 204, was grown off the nickel tube shape die; see Figure 49. The correlation between the regions denoted in Figure 49 and the growth velocities and distances grown in those regions is given in Table IX. During the start of this run some of the LiF melt rose, by capillary action, up the space separating the die top and the surrounding heat shield. The newly seeded crystal spread over the outside edge of the die and began growing from that liquid. As more crystal was pulled upwards,

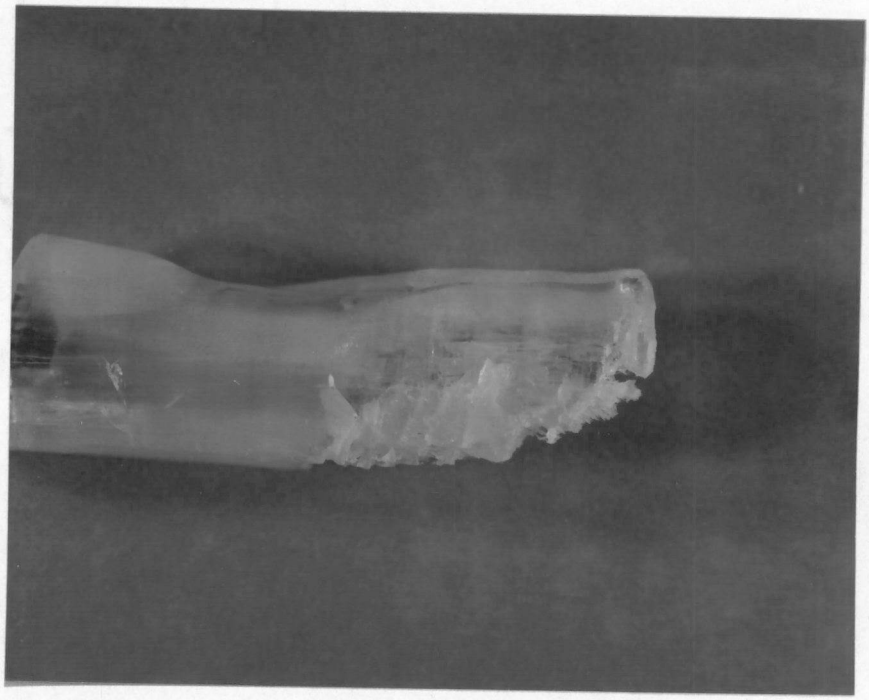


Figure 48. End section of LiF tube shaped sample 182 showing loss of stability.

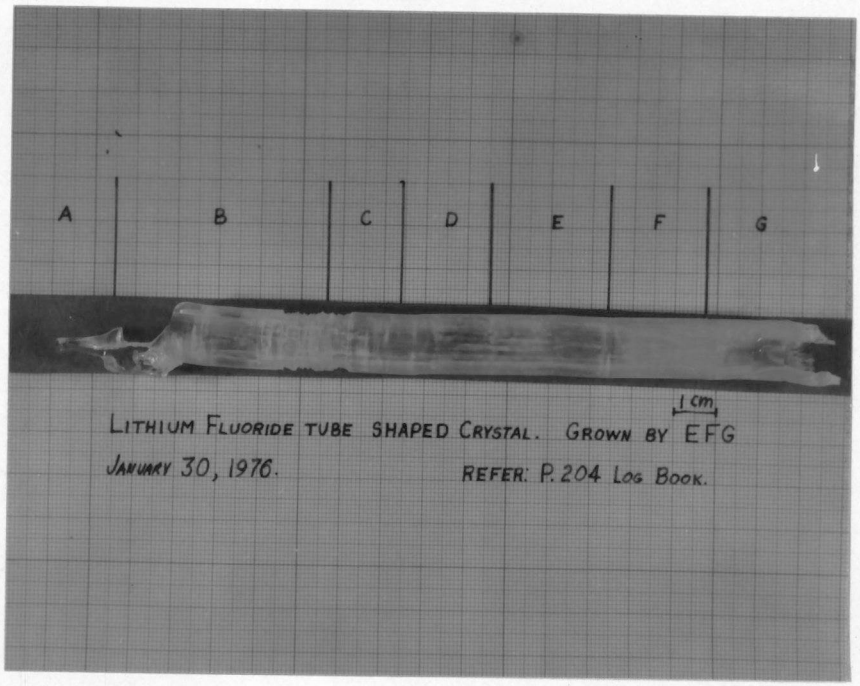


Figure 49. LiF tube shaped sample 204.

TABLE IX

CORRELATION OF THE DENOTED REGIONS OF THE LiF TUBE SHAPED SAMPLE 204 SHOWN IN FIGURE 49 WITH THE GROWTH VELOCITIES AND DISTANCES GROWN IN THOSE SECTIONS

Section	Growth Velocity (cm/hr)	Distance Grown (cm)
A	2.50	2.08
B	5.00	5.25
C	2.50	1.88
D	4.00	2.06
E	6.00	3.00
F	10.00	2.50
G	15.00	2.50

it spread out across the liquid in the gap between the die top and heat shield until it touched the heat shield. Subsequently the crystal froze to the heat shield and lifted it completely off the die assembly. Stable growth was maintained by increasing the die temperature to adjust for the heat loss increase caused by the absence of the heat shield. Stable growth was maintained for 2.5 cm at which point the meniscus film became very unstable. The liquid film exhibited great difficulty in maintaining complete wetting and edge definition was lost; see Figure 50. Stable growth was reestablished by increasing the die temperature and reducing the growth velocity from 5.00 cm/hr to 2.50 cm/hr which was a more manageable growth velocity. Stable growth was subsequently achieved and maintained at growth velocities of 4.00 cm/hr, 6.00 cm/hr and 10.00 cm/hr. When the growth velocity was increased to 15.00 cm/hr meniscus film thickness increased extensively on one side of the die. The outside edge of the crystal began losing contact with the die and steadily collapsed towards the inside die edge. An attempt to reestablish stable growth by reducing the die temperature failed as it caused a loss of wetting on the opposite side of the die due to excessive lowering of the die temperature; see Figure 51.

Both samples 182 and 204 exhibit through thickness cracks running parallel to the growth direction. These

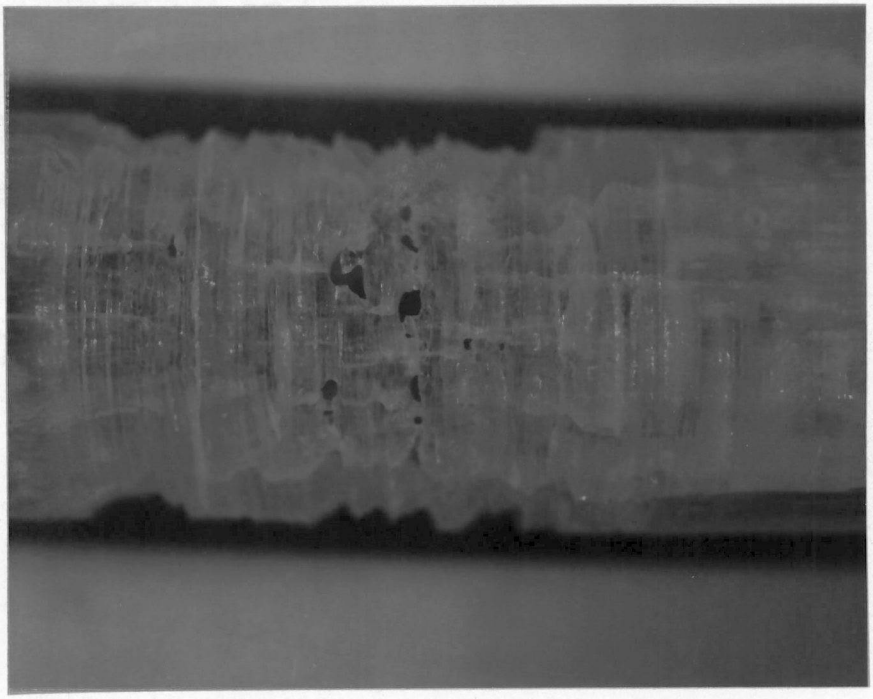


Figure 50. Area of LiF sample 204 showing massive instability.

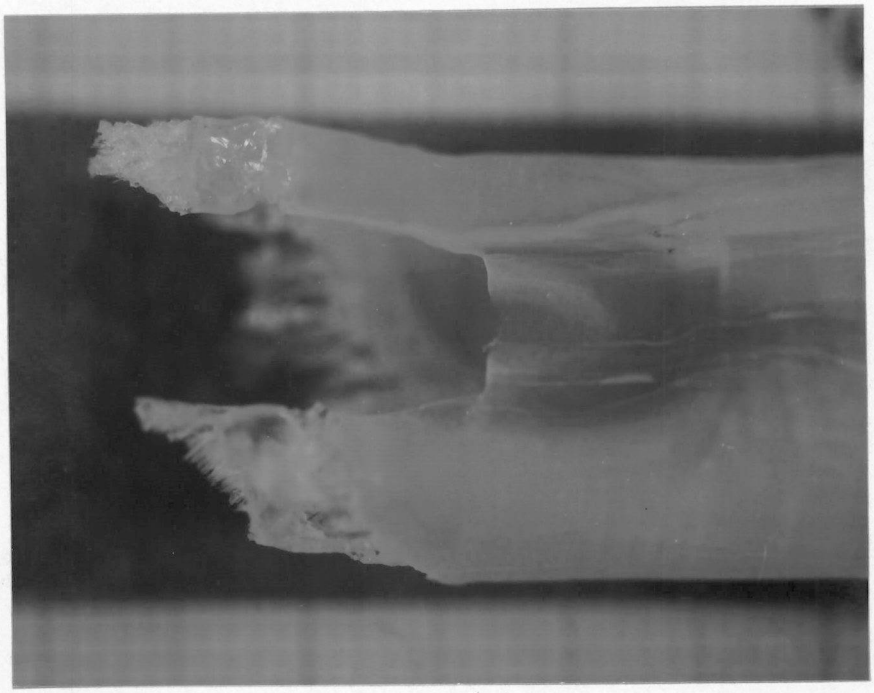


Figure 51. End section of LiF tube shaped sample 204 showing loss of stability.

cracks formed in the sample during the growth run and appear to be of a cleavage type. High residual stresses remain in the sample after growth is terminated as was evidenced by the occurrence of circumferential cleavage cracks induced by gentle handling of the sample during its removal from the EFG unit.

Liquid feed was never a problem with the growing of samples 182 and 204. In both cases described, the melt level in the crucible was never more than 2 cm from the top of the capillary die. Adequate liquid was observed to be in the capillary even after both growth runs were completed.

Two square cornered U-shaped channel samples of LiF were produced from the similarly shaped nickel die by the EFG process. The first LiF sample grown using the channel shape die is designated 246; see Figures 52 and 53. The correlations between the areas designated in Figure 52 and the growth velocities and distances grown is given in Table X.

During the growth of LiF sample 246 an excessive melt level resulted in liquid rising up between the heat shield and the die top. When growth was initiated on the die surface no edge definition was established as the seed also contacted the liquid in the space separating the die top and capillary. As it was pulled upwards, the growing crystal spread across the liquid, contacted the heat shield and froze

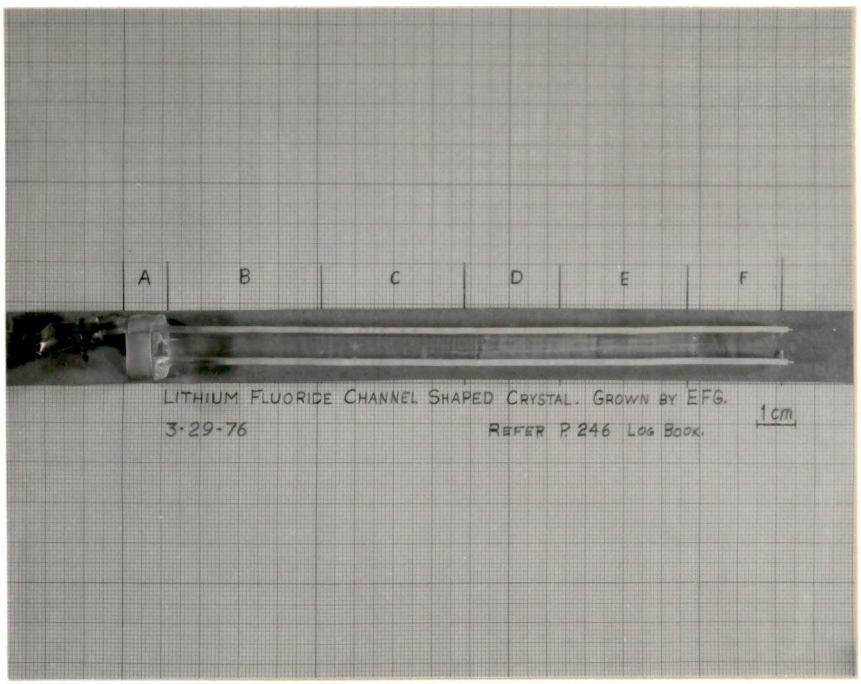


Figure 52. LiF channel shaped sample 246, full length view.

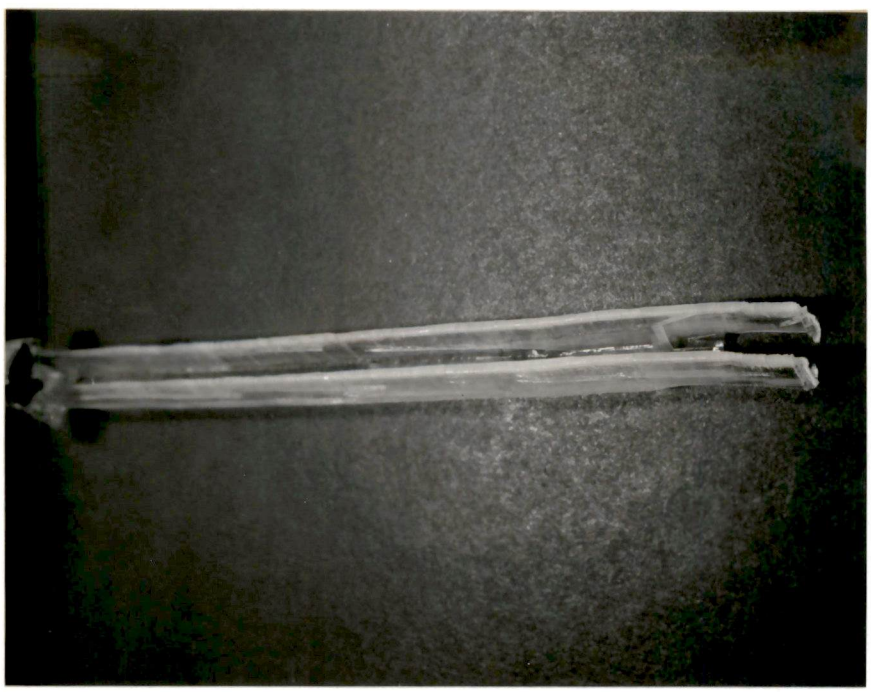


Figure 53. LiF channel shaped sample 246, perspective view.

TABLE X

CORRELATION OF DENOTED REGIONS OF LiF CHANNEL SHAPED SAMPLE 246 SHOWN IN FIGURE 52 WITH THE GROWTH VELOCITIES AND DISTANCES GROWN IN THOSE SECTIONS

Section	Growth Velocity (cm/hr)	Distance Grown (cm)
A	1.00	1.12
B	2.00	4.00
C	5.00	3.75
D	7.50	2.50
E	10.00	3.33
F	15.00	2.50

to it. The heat shield was subsequently lifted from the die. The die temperature was increased to compensate for the extra heat loss and stable growth was maintained without the shield. The sample was grown in a steady-state fashion at 2.00 cm/hr, 5.00 cm/hr, 7.50 cm/hr and 10.00 cm/hr with complete or nearly complete wetting and good edge definition. At 15.00 cm/hr growth velocity, the film on side 2, see Figures 54 and 55, became excessively thick with the side itself necking in the thickness direction and losing contact with the die. Attempts to reduce the film thickness of side 2 by reducing the die temperature resulted in sides 1 and 3 losing edge definition at ends A and D. The die became too cold at A and D for the meniscus film to continue wetting those areas. As a result, sides 1 and 3 began steadily regressing towards corners B and C. Side 2 lost contact altogether and the run was terminated shortly thereafter.

A second LiF sample of channel shape, designated 256, was grown off the channel shape nickel die, without a heat shield around the top. This sample was grown at a constant velocity of 2.50 cm/hr; see Figures 56 and 57. The crystal is of good optical quality and edge definition. As in the previous channel shaped crystal, LiF crystal 256 exhibited the greatest difficulty in maintaining edge definition at ends A and D. These ends are the areas of greatest heat

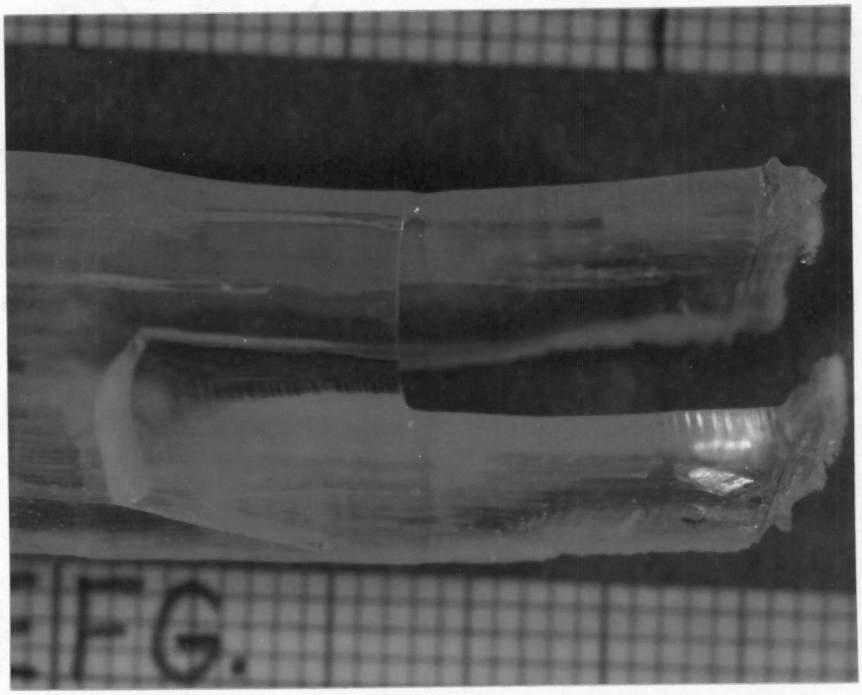


Figure 54. Loss of stability at end section of LiF channel shaped sample 246. V_p = 15.00 cm/hr.

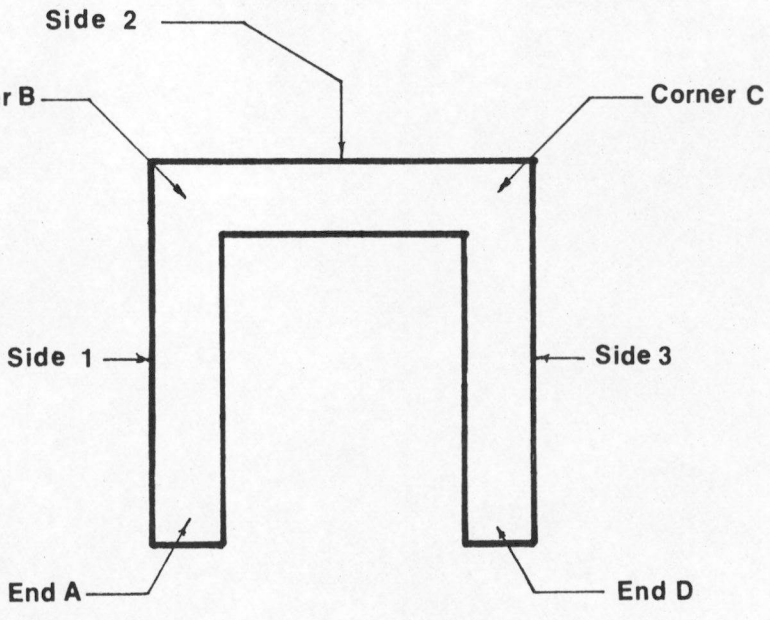


Figure 55. Schematic diagram of channel shaped sample cross section. Intended for reference purposes.



Figure 56. Full length view of LiF channel shaped sample 256.



Figure 57. Perspective view of LiF channel shaped sample 256.

loss and also where there is a lack of beveling from the capillary slot up to the growth surface. The first factor means that areas A and D tend to be lower in temperature than the rest of the die surface which is inhibitory to wetting. The second factor means that fluid flow to the film at areas A and D is more difficult than at other areas of the die. Hence it is harder to maintain a meniscus film to the edge of the die in the areas A and D than it is in other regions of the die surface.

Both channel shaped samples 246 and 256 exhibited cracking during growth. Sample 246 has several cracks of a cleavage type running parallel to the growth direction in each of its sides. These cracks are on the order of 7 cm in length. Sample 256 has only one cleavage crack in one of its sides and this crack was caused by residual stresses as it occurred after the crystal was grown. The only cracks that were formed in sample 256 during growth are around 2 cm in length, at a 45° angle to the growth axis and located in the section of the crystal where spreading was taking place. Both 246 and 256 exhibited a large amount of residual stress as was evidenced by the existence of many small cleavage cracks formed while handling the samples during their removal from the EFG unit. The residually formed cracks are primarily under 2 cm in length and oriented perpendicular to the growth axis.

Lack of liquid feed up the capillary slot to the meniscus film was not a problem in the case of either sample 246 or 256. The bulk liquid level was always within a 2 cm distance of the die top surface. Liquid was observed in the capillary at all time during both growth runs.

LiF/CaF_2 Airfoil Shaped Crystal

One sample, designated 233, was produced by the EFG process that was of LiF/CaF_2 eutectic composition (80.5 mole percent LiF); see Figures 58 and 59. Sample 233 was grown using the nickel airfoil shape die. The eutectic material was chosen as a candidate for EFG for two reasons. The first was to test the processes' ability to produce coupled, directionally aligned eutectic structure. The second reason was to study the characteristics of the solid-liquid interface indirectly by studying the morphology of the eutectic microstructure of a crystal grown by EFG. A small velocity perturbation of the growing interface will cause a change in the spacing of the eutectic lamellae[32] and leave a discernable trace of the solid-liquid interface position and shape. Thus, a controlled growth velocity change could be incorporated as a "perturbation" to demark the instantaneous shape and position of the interface. In this manner, study of the solid-liquid interface could be accomplished.

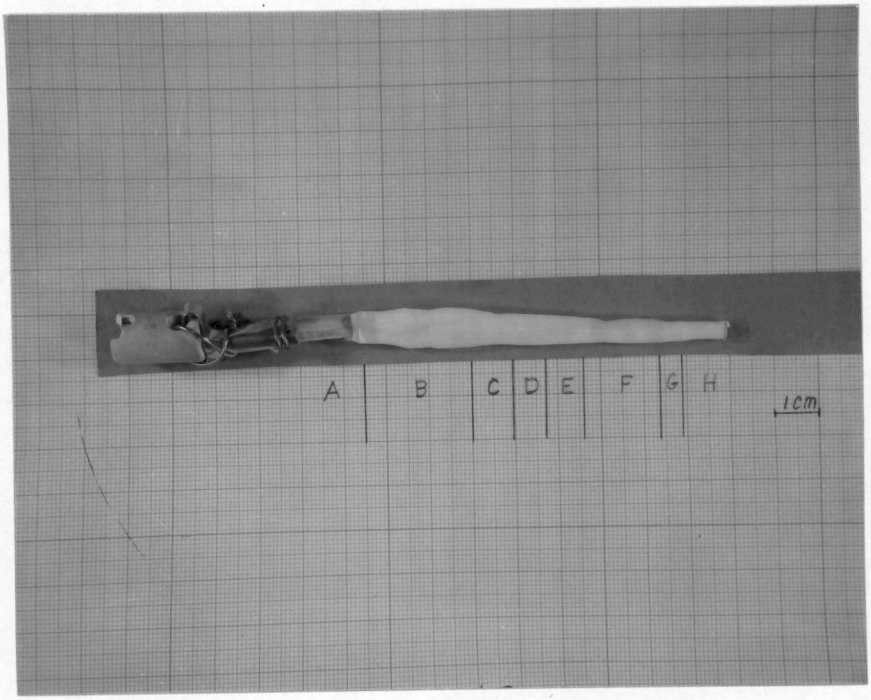


Figure 58. Full length side view of LiF/CaF_2 eutectic sample 233.

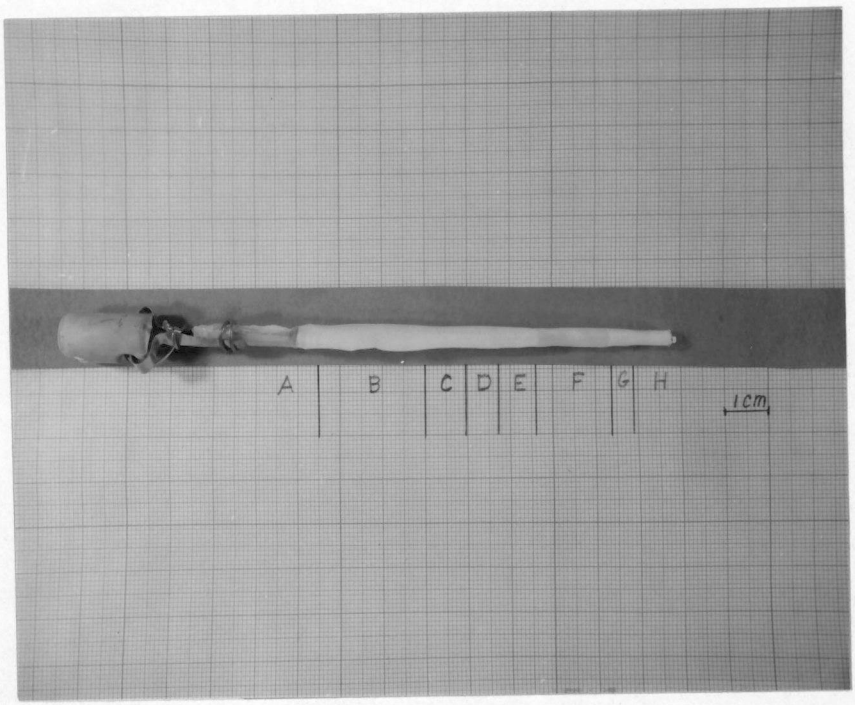


Figure 59. Full length edge view of LiF/CaF_2 eutectic sample 233.

The seed crystal used to initiate growth of the LiF/CaF_2 eutectic crystal was 100 percent LiF in composition. This was a slight hinderance at the outset of growth because the melting points of LiF and LiF/CaF_2 eutectic differ by 73°C (LiF: T_m = 842°C; LiF/CaF_2: T_m = 769°C). This lead to an initially high die temperature for growth of the eutectic in order to melt off a small portion of the seed crystal to establish contact with the liquid in the capillary. By careful adjustment of the die temperature and pull velocity a small amount of LiF/CaF_2 eutectic was solidified onto the seed and this temperature problem was abated.

Wetting and spreading across the die surface were the major problems during the growth of the LiF/CaF_2 eutectic sample. The sample never spread completely to the outside edge of the die. At its point of greatest coverage, the sample approximated the die shape but did not fully cover the die top surface. This shape degenerated into an oblong rounded rectangle as the run progressed. Initially the atmosphere was tank N_2 passed over copper turnings maintained at 350°C. In this atmosphere, the nickel surfaces appeared very clean and free of oxide. However, the wetting of the die surface by the eutectic liquid was very poor. Small amounts of air were introduced into the containment chamber until the die surface became visibly oxidized. The meniscus film was observed to spread over the oxidized surface with

greater ease than over the unoxidized surface of the nickel. Even so, the film was very active and its position unstable. It would, beginning at one position, spread a relatively large distance on the die and after maintaining the new position momentarily, would recede back to a position near to its start. This spreading and receding cycle was repeated frequently at sporadic intervals. The erratic behavior of the film dissipated as more crystal grew, increasing the coverage of the die surface and as the oxygen present in the atmosphere gas depleted with time. Air was repeatedly introduced into the chamber in an effort to induce more spreading. Consequently, the die became heavily oxidized. The heavy oxidation was not conducive to wetting of the die as was evidenced by the continually receding cross section of sample 233 after 2.5 cm of growth. Despite attempts to correct the situation by changing die temperature and growth rate, the sample continued to slowly neck in until the end of the run. Table XI correlates the regions of LiF/CaF_2 sample 233 denoted in Figure 58, page 115, by capital letters with the growth velocities and distances grown in those sections.

Even with the lack of full wetting, approximately 8 cm of eutectic sample was grown under near steady-state conditions. The microstructure in sections A through G of sample 233 is predominantly coupled lamellar eutectic

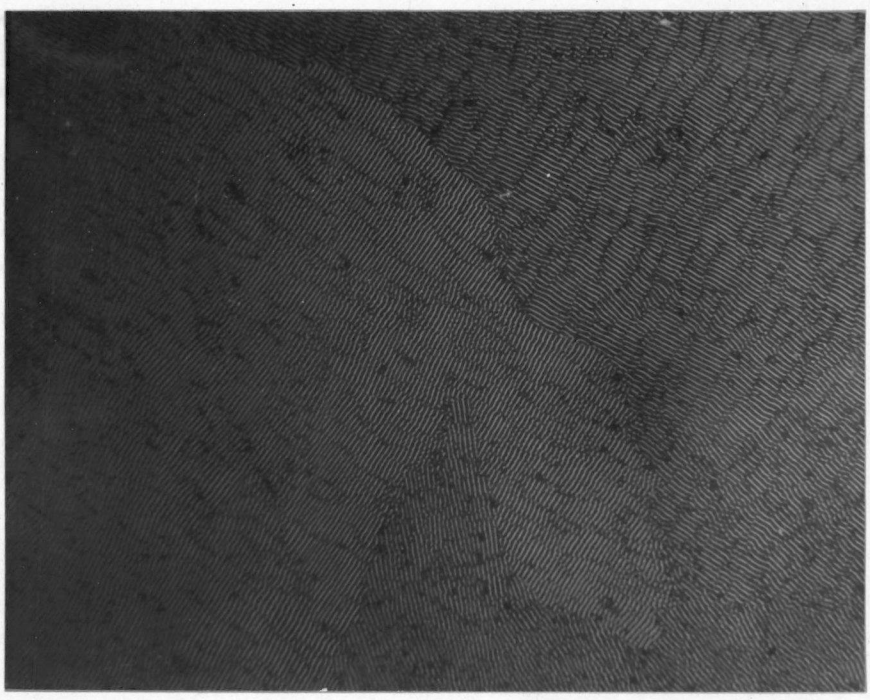
TABLE XI

CORRELATION OF THE DENOTED REGIONS OF LiF/CaF_2 EUTECTIC SAMPLE 233 SHOWN IN FIGURE 58 WITH THE GROWTH VELOCITIES AND DISTANCES GROWN IN THOSE SECTIONS

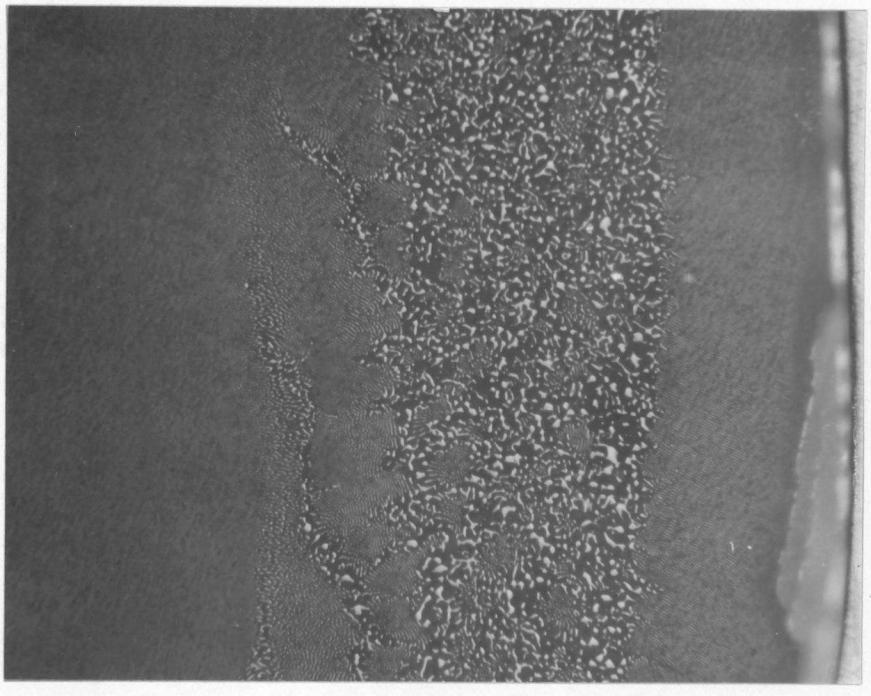
Section	Growth Velocity (cm/hr)	Distance Grown (cm)
A	1.00	0.40
B	2.00	2.50
C	2.50	0.96
D	3.00	0.75
E	4.00	0.87
F	1.50	1.77
G	5.00	0.50
H	10.00	1.00

aligned parallel to the direction of pull. Examples of this structure are shown Figures 60(a), 61(a), 62(a) and 63(a). Refer to Table XII for correlations between section, growth velocity and lamellar spacing. Also found in sections B, C, D, E, F and G are areas which exhibit a breakdown of the lamellar structure into a cellular structure; see Figures 60(b), 61(b), 62(b), and 63(b). In all sections of sample 233 exhibiting cellular growth, the region in which the cells are located is a band near to, but not at, the outer surface of the crystal. The microstructure of sample 233 directly at the outer surface of the crystal is lamellar eutectic. In general, the lamellae in this outer band are aligned at an angle, on the order of 20 to 30 degrees, to the direction of pull and are growing downwards and out towards the surface of the crystal; see Figure 64.

It is necessary to note at this point that the solid-liquid interface of the growing crystal was not entirely flat and parallel to the die top surface. Near the outside edge of the crystal, the solid-liquid interface curves upwards away from the die surface. This upward curvature is evident in the striations seen in a longitudinal section of the crystal at the point of velocity change from 1.00 cm/hr to 2.00 cm/hr in regions A to B; see Figure 65. The curvature effect at the spreading edge of the crystal is

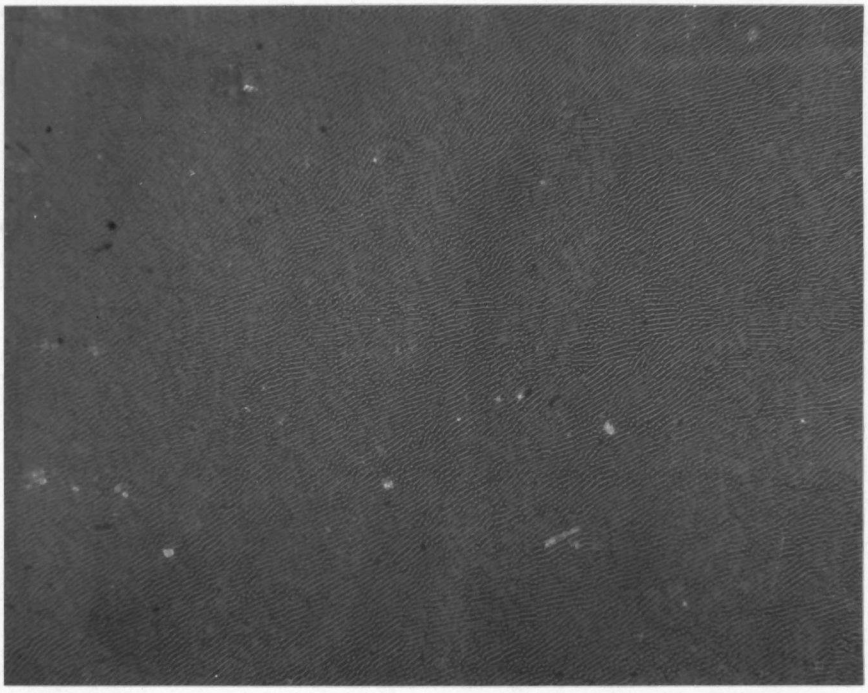


(a) Magnification: 200X

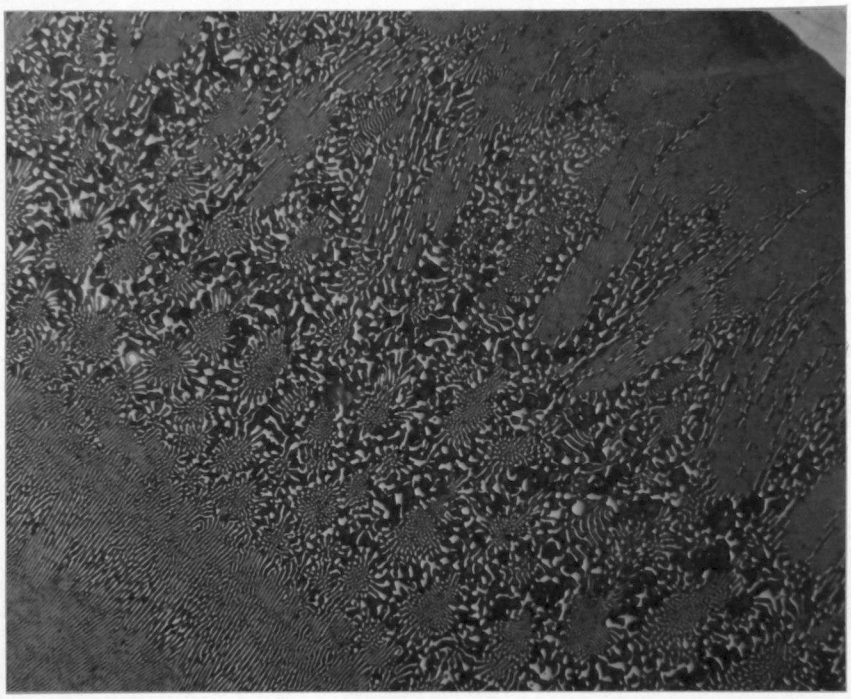


(b) Magnification: 100X

Figure 60. LiF/CaF_2 eutectic sample 233 microstructure, section B. (a) Transverse view showing lamellar structure. (b) Transverse view showing lamellar to cellular transformation.

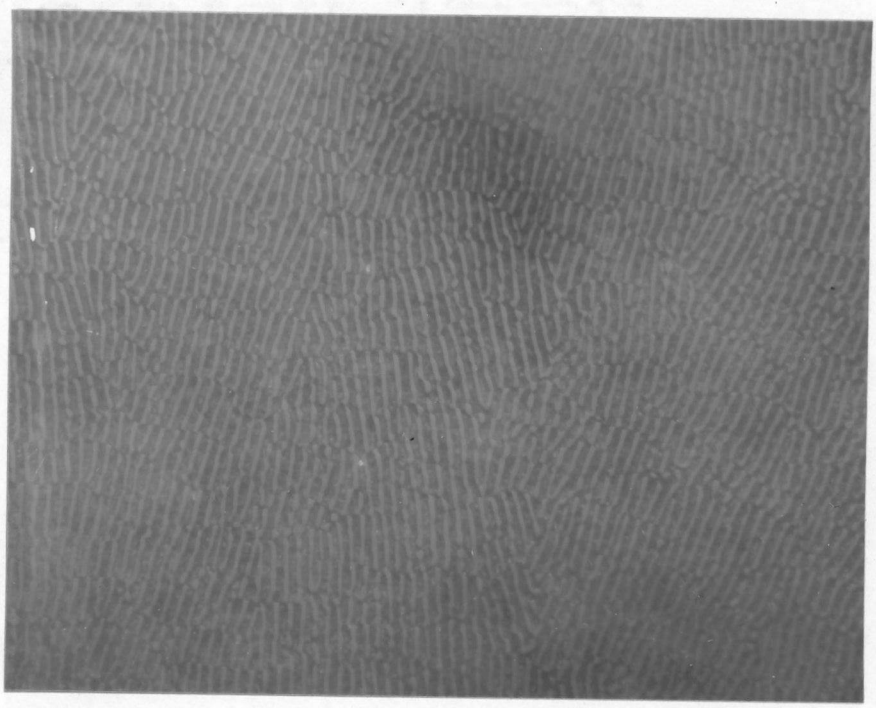


(a) Magnification: 200X

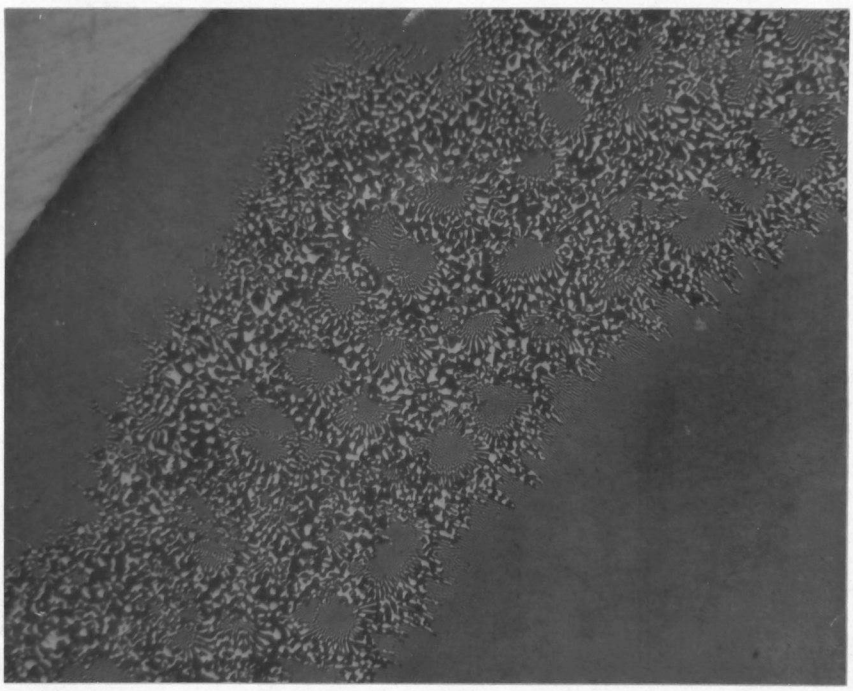


(b) Magnification: 140X

Figure 61. LiF/CaF_2 eutectic sample 233 microstructure, section C. (a) Transverse view showing lamellar structure. (b) Transverse view showing lamellar to cellular transformation.

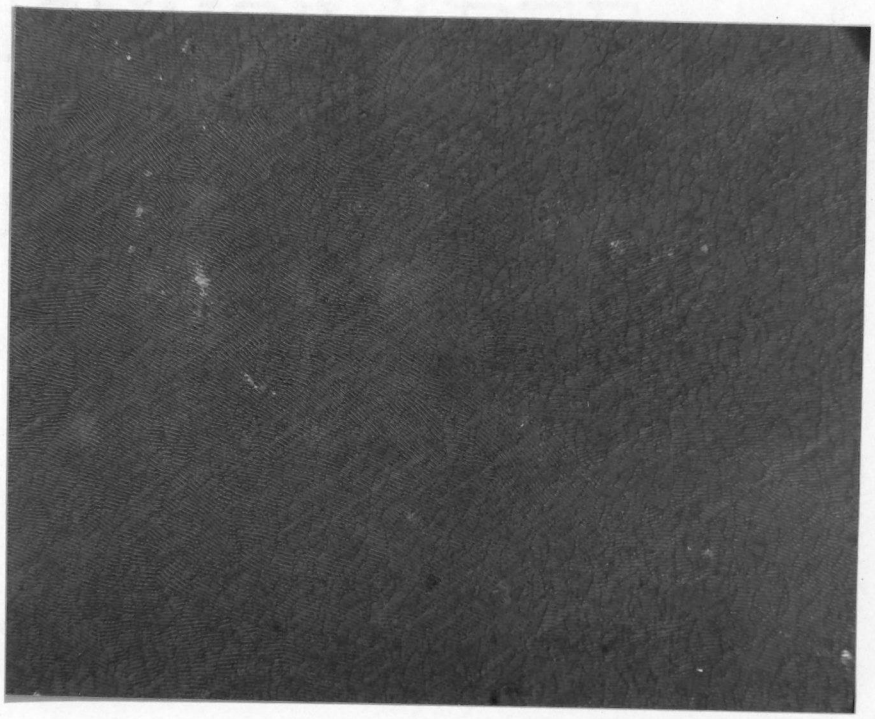


(a) Magnification: 690X

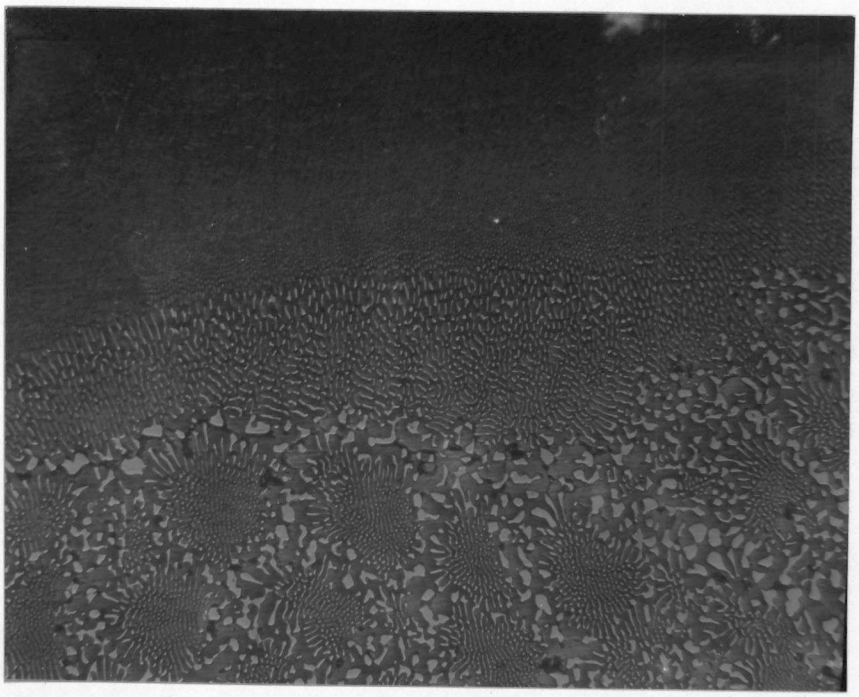


(b) Magnification: 100X

Figure 62. LiF/CaF_2 eutectic sample 233 microstructure, section D. (a) Transverse view showing lamellar structure. (b) Transverse view showing lamellar to cellular transformation.



(a) Magnification: 200X



(b) Magnification: 200X

Figure 63. LiF/CaF_2 eutectic sample 233 microstructure, section E. (a) Transverse view showing lamellar structure. (b) Transverse view showing lamellar to cellular transformation.

TABLE XII

CORRELATION OF GROWTH VELOCITY AND LAMELLAR SPACING

Section	Growth Velocity (cm/hr)	Lamellar Spacing (cm)
B	2.00	2.9×10^{-4}
C	2.50	2.8×10^{-4}
D	3.00	2.6×10^{-4}
E	4.00	2.5×10^{-4}
F	1.50	3.3×10^{-4}

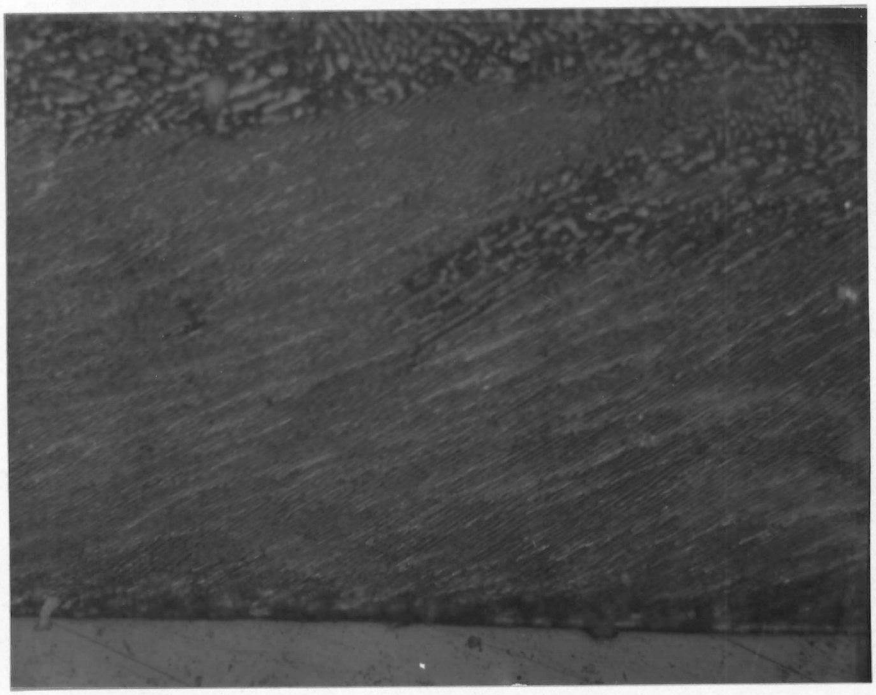
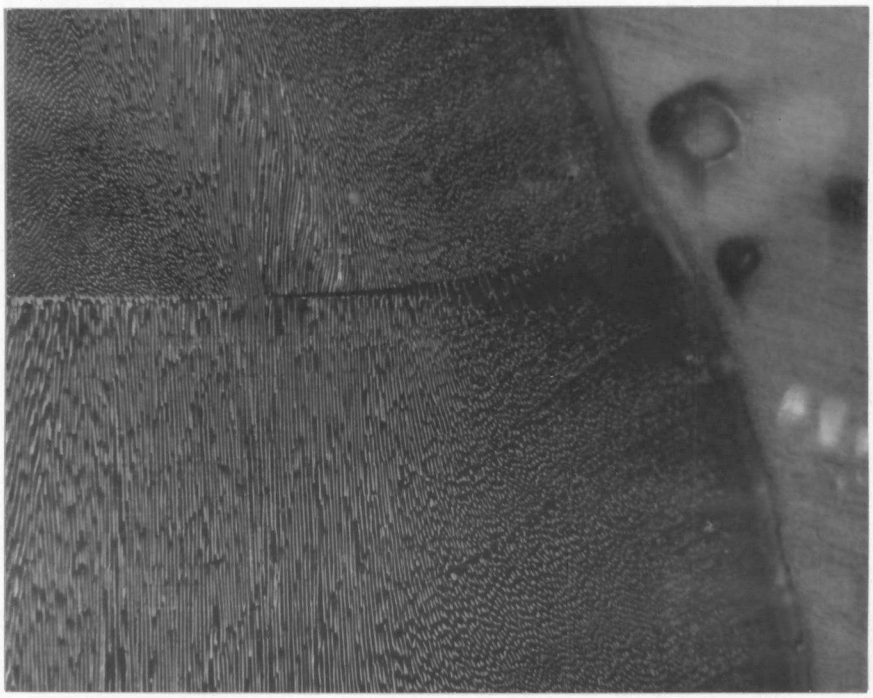


Figure 64. Longitudinal view of section G showing growth direction of lamellae in outer band of microstructure. Magnification: 200X $V_p \longrightarrow$



V_p

Figure 65. Longitudinal view of section A/B showing shape of solid-liquid interface through striations in the microstructure. Magnification: 100X

caused by the variation in die temperature with location. Heat can leave the die by radiation and conduction through the crystal only in the area covered by the sample itself. The remaining area of the die loses heat by radiation into the chamber, a less effective method than radiation/conduction through the crystal. Consequently, during spreading the die is at a higher temperature in the area not yet covered by crystal than it is in the area covered by spreading crystal. The edges of the sample reflect the transition in temperature from the cooler covered area to the hotter uncovered area by the displacement of the interface to a position further away from the die. Meanwhile at the center position of the solid-liquid interface, away from the end effects, heat from the die is effectively removed by radiation and conduction through the crystal. The interface is flat, parallel to the die surface, and the meniscus film thickness is less than that at the edges of the crystal.

For clarity in the continuing discussion of sample 233, a typical section of the crystal is schematically represented in Figure 66. Note in Figure 66 the representation of the shape of the solid-liquid interface, the positions and relative widths of the areas exhibiting cellular and lamellar growth, and the shape and extent of the meniscus film.

The cellular growth in sample 233 is always found in a region where the solid-liquid interface is curved; see

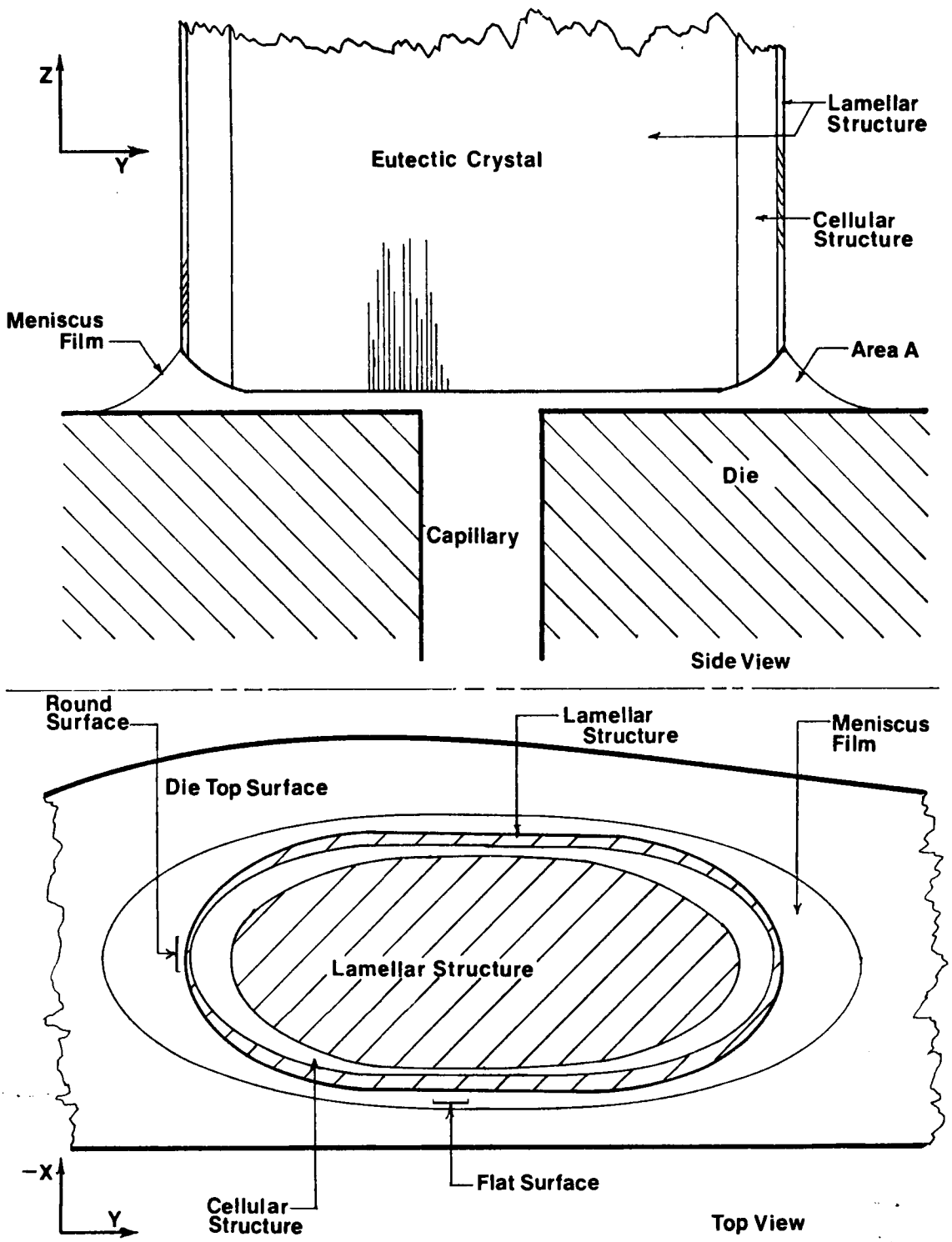


Figure 66. Schematic diagram of a LiF/CaF_2 eutectic crystal growing by EFG from an airfoil shape die.

Figure 67. The lamellar structure in the center region of the sample grows with a flat solid-liquid interface and is aligned parallel to the direction of pull; see Figure 68. However, the lamellar band of structure at the sample surface grows with a curved solid-liquid interface; see Figure 67. In explaining the above observations, consider the following. Both the band of cellular structure and the band of lamellar structure vary in width depending upon their circumferential position in a given cross section. Measurements of the cellular band width in the X-Y plane, see Figure 66, were taken from sections B, C, D, E and F. The width was measured both in an area of the band near a flat surface (i.e., radius of curvature is large), and in an area near a curved surface (i.e., radius of curvature is small); again see Figure 66. Also, measurements were taken of the lamellar band width in sections B, C, D, E and F. Areas near curved and flat surfaces in each region were measured. The results are given in Table XIII. The measurements indicate that the width of the cellular band increases with decreasing radius of curvature of the sample surface in the X-Y plane; see Figure 66. The width of the outer lamellar band decreases with decreasing radius of curvature of the sample surface in the X-Y plane. However, the results do not show a definite relationship between band width and growth velocity.

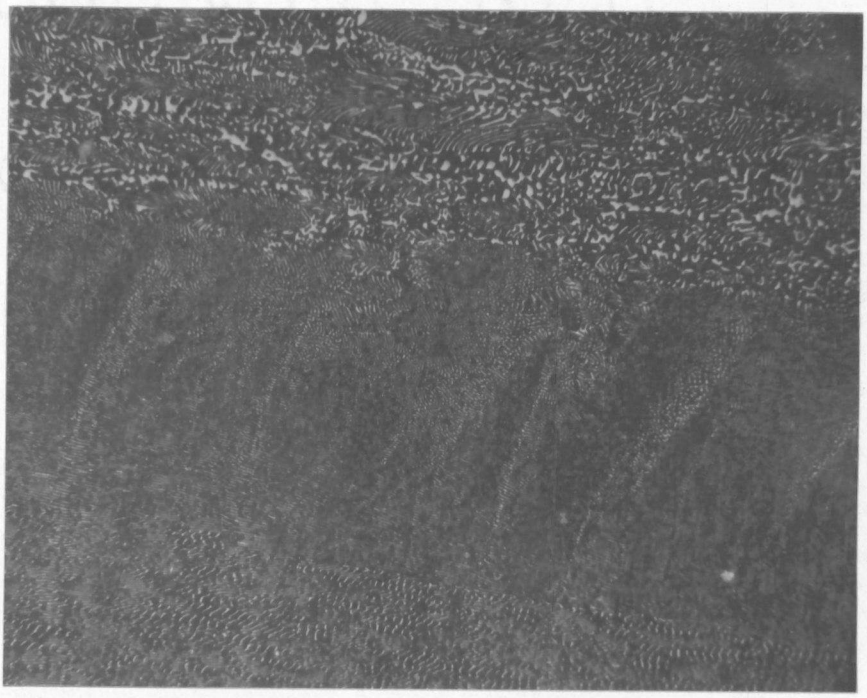


Figure 67. Longitudinal view of section B showing cellular structure existing at curved interface. Magnification: 100X $V_p \longrightarrow$

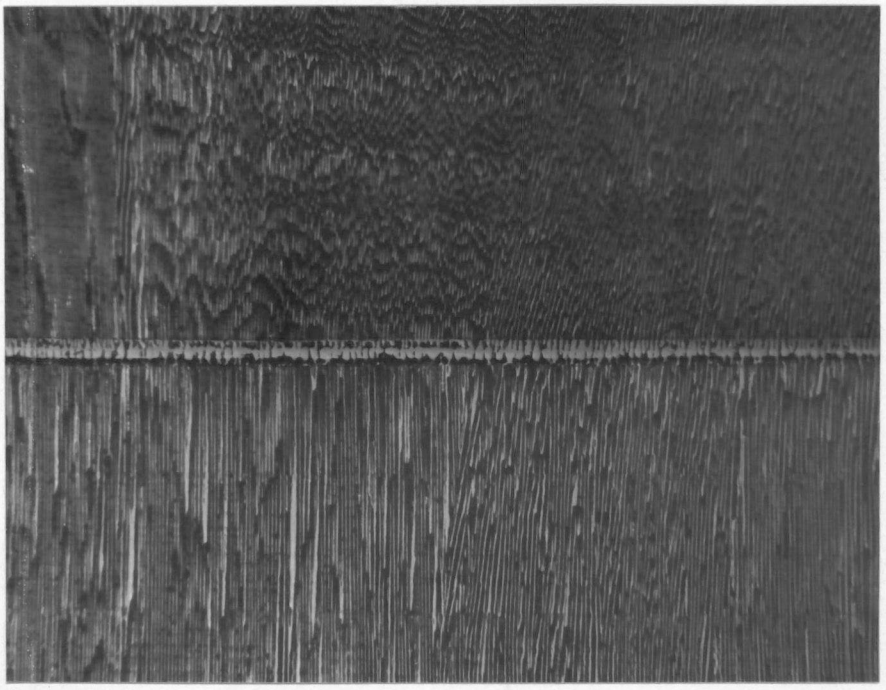


Figure 68. Longitudinal view of section A/B showing lamellar structure at flat interface. Magnification: 100X.

TABLE XIII

RESULTS OF WIDTH MEASUREMENTS OF CELLULAR AND LAMELLAR AREAS IN SAMPLE 233

Section	V_p (cm/hr)	Flat Surface		Curved Surface	
		Lamellar Band Width-cm	Cellular Band Width-cm	Lamellar Band Width-cm	Cellular Band Width-cm
B	2.00	0.051	0.027	0.063	0.003
C	2.50	0.073	0.022	0.078	0.017
D	3.00	0.064	0.024	0.075	0.005
E	4.00	0.055	0.020	0.085	0.004
F	1.50	no cells		0.049	0.010

Measurements were taken of the relative volume fractions of the LiF and CaF_2 phases present in the microstructure. It was found that the relative volumes of each phase were in good agreement with the theoretically calculated volume fractions for an alloy of LiF and CaF_2 at eutectic composition. It was concluded from this result that within the accuracy of the measurements, sample 233 is at eutectic composition. This measurement was made to rule out the possibility of the sample being off eutectic composition and that being off composition resulted in the lamellar to cellular breakdown of the structure at the existing thermal gradients and growth velocities.

From the preceding discussion it is evident that the lamellar to cellular structure breakdown observed in crystal 233 is a direct result of different growth directions existing at the curved solid-liquid interface. Similar lamella to rod transformations have been observed in eutectic alloys by Hunt and Chilton.[33] This transformation was later explained by Hunt[34] in terms of the changing growth directions at a curved interface and the relative interphase energies of the phases present. Clearly Hunt's analysis is applicable to the observations in this study which show the lamellar to cellular breakdown only in areas of curved growth interface and an increasing area of cellular structure occurring with increasing curvature.

However, the above does not explain the lamellar structure found at the surface of the sample which can be observed growing in an area where the growth interface is curved. This question will now be considered. It was observed during the growth of sample 233 that the meniscus film at the ends of the sample, where the radius of curvature is smallest, was on the order of 2 to 3 times the thickness of the film at the sides of the sample where the radius of curvature is largest. Also, the meniscus film at the rounded ends tended to spread further across the die than the film at the flat sides did. Both observations are shown schematically in Figure 66, page 128. The larger more exposed portion of the meniscus film at the rounded ends could be viewed readily during growth. Small particles of matter, probably bits of NiO broken free of the die surface, were observed to be in turbulent motion near the surface of that portion of the film which was visible at the rounded ends of the sample; see Figure 66, area A for location. The tuburlent motion in the above-mentioned portion of the meniscus film can tentatively be attributed to a combination of two fluid flow mechanisms. These mechanisms are (1) fluid flow induced by a pressure difference in the film caused by a variation in the radius of curvature of the film and (2) convective fluid flow caused by temperature gradients in the liquid film. Consider a solid-liquid-vapor junction of a crystal growing from a film

resting on a die such as the situation depicted schematically in Figure 69. Equation (1) is the general expression for the pressure difference across a curved interface. In the case shown in Figure 69, points A and B very near the surface of the film have pressures P_{1a} and P_{1b} associated with them. The pressure difference across the film in the neighborhood of point A can be expressed as

$$P_{1a} - P_2 = \gamma\left(\frac{1}{r_1^*} + \frac{1}{r_2^*}\right), \tag{43}$$

where P_2 is the atmospheric pressure, γ is the surface energy of the film, and r_1^* and r_2^* are the principal radii of curvature for the film near point A. Similarly, the pressure difference across the film near point B can be expressed approximately as

$$P_{1b} - P_2 = \gamma\left(\frac{1}{r_1} + \frac{1}{r_2}\right), \tag{44}$$

where r_1 and r_2 are the principal radii of curvature of the film near point B. From the observations made of the meniscus during the growth of sample 233 it appears that the region where turbulent flow was observed is one of double curvature. The film at the ends of the spreading crystal is concave in the Y-Z plane (i.e., longitudinal plane) and convex in the X-Y plane (i.e., transverse plane); see Figure 69. Taking

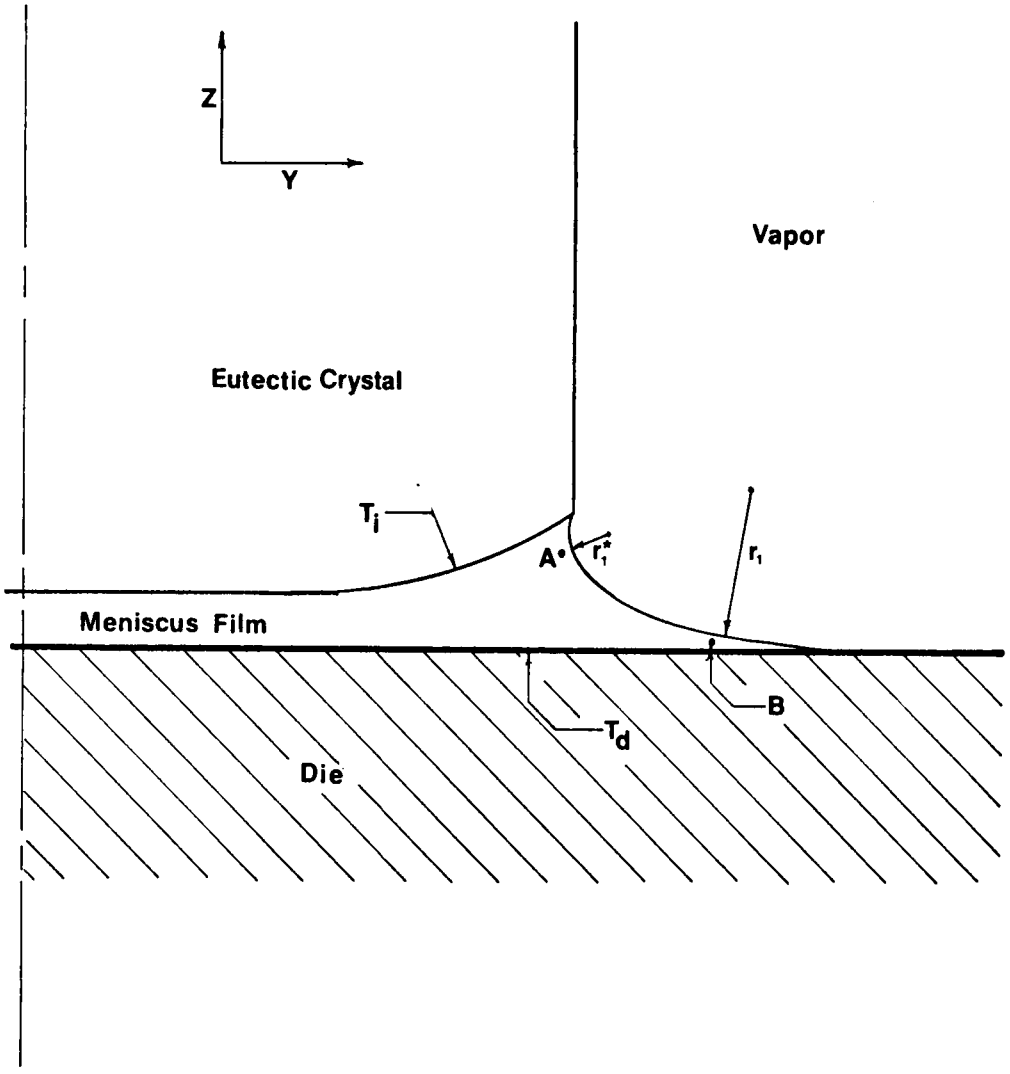


Figure 69. Schematic diagram of solid-liquid-vapor junction of a crystal growing from a film resting on a die.

the convex curvature as positive makes r_2^* and r_2 positive quantities and r_1^* and r_1 negative quantities. The pressure variation from point A to point B is of interest in regards to the turbulent flow observed. As an illustrative example, consider the following. Estimating that $r_2^* = 1.5$ mm, $r_2 = 2.0$ mm, $r_1^* = 0.1$ mm, $r_1 = 4$ mm and taking $P_2 = 1.013 \times 10^6$ dynes/cm^2 (1 atm.) and γ as a constant, equal to the surface tension of molten LiF, 263 dynes/cm^2,[35] equations (43) and (44) yield values for P_{1a} and P_{1b}. $P_{1a} = 0.988 \times 10^6$ dynes/cm^2, and $P_{1b} = 1.102 \times 10^6$ dynes/cm^2. Although the calculation is at best a rough estimate of the actual situation, it serves to demonstrate that there is a pressure drop from point B to point A in Figure 69 and therefore fluid flow from point B to A can indeed exist in the film. Thus, flow is induced by the variation in the curvature of the meniscus film.

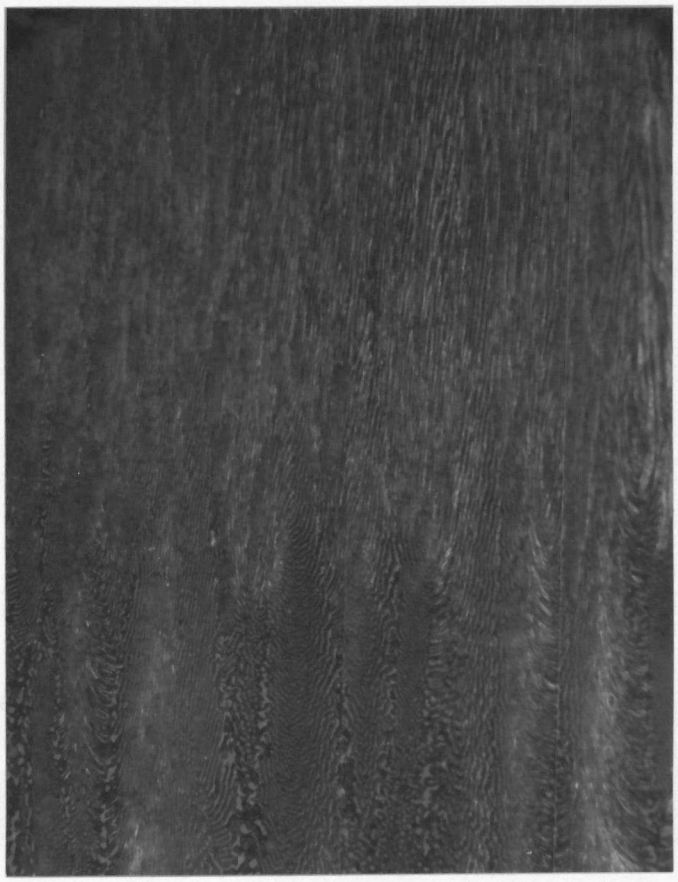
In addition there is the convective flow of fluid in this area of the film. The die temperature, T_d, is higher than the solid-liquid interface temperature, T_i, which means that the fluid bordering the die is less dense than that bordering the interface, a convective situation. Hence, there is a tendency for the fluid near the solid-liquid interface to flow downwards to the die surface and for the fluid near the die to flow upwards. In this manner a convective fluid flow cell may operate. If both the convective flow and the interface curvature induced flow

mechanisms were summed together, a flow region would result in the film at the edge of the growing crystal.

This region of turbulent flow in the meniscus apparently acts to even out the variations in the temperature gradient across the solid-liquid growth interface in the neighborhood of the solid-liquid-vapor junction. By doing so, the variation in growth direction at that portion of the interface is reduced to the point where coupled lamellar growth can take place, even though there is some curvature of the interface. Certainly such a mechanism would relate to the lamellar band present at the surface of crystal 233.

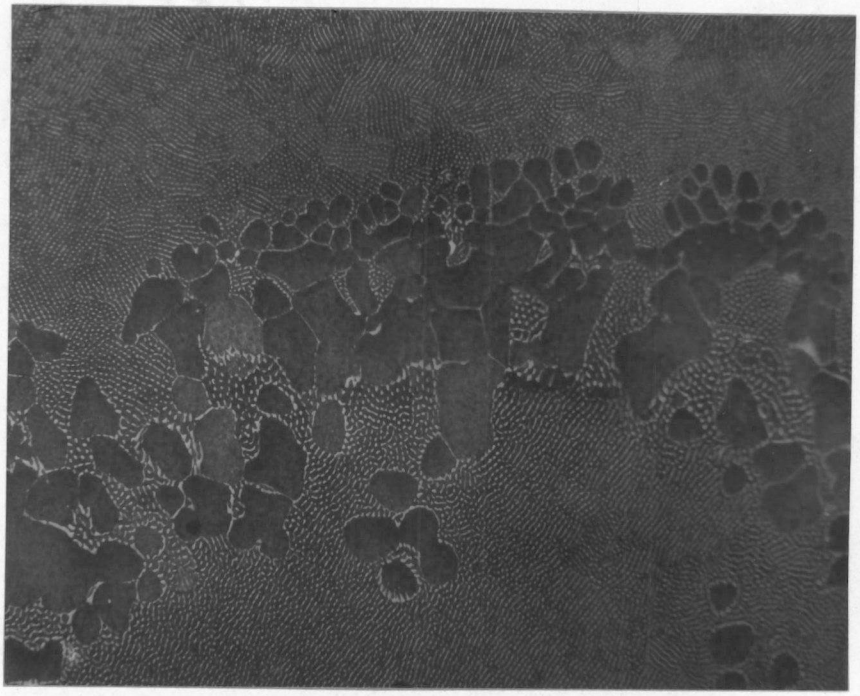
The lamellar structure was maintained at growth velocities up to and including 5.00 cm/hr. The last section of sample 233 was grown at 10.00 cm/hr and is characterized by a totally cellular structure. The growth interface completely breaks down at the point of the velocity change from 5.00 to 10.00 cm/hr; see Figure 70.

One other isolated region of lamellar to cellular transformation was observed in sample 233. This was a region around the circumference of the capillary hole found in section B grown at 2.00 cm/hr; see Figure 71. This breakdown of structure over the capillary hole was observed only in section B and in none of the other parts of sample 233. The microstructure indicates that the transformation occurred due to varying temperature gradients



V_p

Figure 70. Microstructure of sample 233 at growth velocity change of 5.00 cm/hr to 10.00 cm/hr. Magnification: 200X



(a) Magnification: 200X



(b) Magnification: 200X $\overrightarrow{V_p}$

Figure 71. Lamella to rod transformation in section B of sample 233. Area shown is over capillary hole. (a) transverse; (b) longitudinal.

at, and curvature of the solid-liquid interface in the neighborhood of, the capillary hole. As more crystal was grown, the interface apparently flattened out and the microstructure of the region over the capillary hole became indistinguishable from the lamellar structure found elsewhere in the crystal.

VII. DISCUSSION OF RESULTS

This investigation of the edge-defined, film-fed growth process brought to light some diverse aspects of the process. Discussed below are some conclusions and observations of particular interest.

1. The extent of die wetting and edge definition can be limited by the crystallographic orientation of the growing specimen if the material exhibits faceted growth upon solidification. This was clearly observed during the growth of the thin ribbon shaped V_2O_5 samples, which exhibited faceting and thus limited both spreading and edge definition.

2. When growing brittle materials the thermal stresses present during growth can be of a magnitude to cause severe cracking in the resulting material. Residual stresses remaining in the material after growth is completed are also quite high. This was evidenced by the multiple cracks forming in shaped LiF samples on removal from the EFG unit. It would be advisable to make the addition of an afterheater system when growing brittle materials which would maintain the temperature of the sample at an elevated level as it is pulled away from the die. This would lessen the thermal gradients present in the sample during growth and thereby eliminate thermally induced cracking. Also after the growth run is terminated, the sample could be slowly brought to

ambient temperature by controlling the afterheater temperature. This controlled cooling rate would minimize the thermally induced residual stresses in the material. However, increasing the temperature of the sample with an afterheater would probably limit the maximum velocity at which the sample could be grown by reducing the heat flow through sample from the freezing interface.

3. The process itself is capable of generating materials in complex shapes. Samples were produced with flat sides, curved sides, square inside and outside corners, and hollow cross sections. The sample shapes produced were thin ribbons, round tubes and square channels. Clearly the process is quite versatile with respect to shape production.

4. Precise temperature control of the die is a requisite for stable growth. This was demonstrated by the limited success in maintaining a stable growth interface in the V_2O_5 ribbon sample growth attempts until a fine control device was superimposed over the coarse controller of the Lepel power supply. It is also helpful to have a die of large thermal mass. This makes the die temperature less sensitive to small power input fluctuations. Hence, the growth interface is less subject to thermal perturbations induced by the die temperature fluctuations. The capillary die should be designed so that the temperature at all areas of the die top surface is constant. Small variations in

temperature did adversely affect the stable growth of crystals. The effect was not obvious until the velocity of pull reached 15.00 cm/hr when growing LiF crystals. This indicates that higher growth velocities require carefully designed dies that have very precise, constant surface temperatures. Accomplishing precise temperature control may be done in part with heat shields around the die top surface.

5. The temperature gradients in the meniscus film are large enough to allow coupled, directional growth of eutectic materials. Eutectic alloys exhibiting coupled growth should be exploited in further studies of the EFG process because the resulting microstructures reveal much information about the solid-liquid interface characteristics, temperature gradients at the interface, effects of fluid flow in the meniscus, and the effects of perturbations on the stability of the process.

6. The solid-liquid interface near the edges of the spreading crystal is curved upwards away from the die surface during the spreading phase of EPG for materials with a large capacity for removing heat from the interface. This curvature is due to the variation in die temperature during spreading. The shape of the interface during steady-state fully wetted growth was not determined. This point is of interest in that this investigation revealed a transformation from lamellae to cells at areas where the solid-liquid

growth interface exhibits curvature. The shape of the interface at the edge of a crystal fully wetting a die would reveal whether or not coupled lamellar structure can be maintained across the entire cross section of the growing crystal. Presumably a die fully wetted would have a more nearly constant temperature across its surface. Nevertheless, one would expect variations in heat flow and temperature at the edge of the die top surface and their effect on the microstructure of a eutectic is of interest.

7. The lamellar to cellular breakdown at the curved portions of the solid-liquid interface of eutectic sample 233 has been explained in terms of differing growth directions existing at the curved interface.

8. Present indications are that fluid flow in the spreading meniscus film edges is turbulent. This flow appears to stabilize the temperature gradients at the curved portions of the solid-liquid interface and enhance coupled growth in those regions when growing eutectic materials. However, very little can be determined for certain from the limited observations of this study. The mechanisms inducing this flow which were proposed are quite tentative at this point.

LIST OF REFERENCES

LIST OF REFERENCES

1. A. V. Stepanov, and A. L. Shakh-Budagon: ZhTF, 1959, vol. 29, p. 394; (Soviet Physics-Tech. Phys., 1959, vol. 4, p. 349).

2. A. V. Stepanov: ZhTF, 1959, vol. 29, p. 381; (Soviet Physics-Tech. Phys., 1959, vol. 4, p. 339).

3. E. von Gomperz: Z. Phys., 1922, vol. 8, p. 184.

4. V. M. Gol'dfarb, A. V. Donskoi, and A. V. Stepanov: Growth of Crystals, vol. 6B, p. 165, Consultants Bureau Inc., N. Y., 1968.

5. J. J. Brissot, and H. Raynaud: Electrochem. Tech., 1963, vol. 1, p. 304.

6. S. V. Tsvinski, and A. V. Stepanov: Soviet Phys.-Solid State, 1965, vol. 7, no. 1, p. 148.

7. C. E. Bleil: Jour. of Crys. Growth, 1969, vol. 5, p. 99.

8. H. E. LaBelle, Jr., and A. I. Mlavsky: Mat. Res. Bull., 1971, vol. 6 p. 571.

9. H. E. LaBelle, Jr.: Mat. Res. Bull., 1971, vol. 6, p. 581.

10. T. Young: Philosophical Trans., 1805, vol. 95, p. 65.

11. B. Chalmers, T. Surek, and J. C. Swartz: Progress Report No. NSF/RANN/SE/GI-37067X/PR/74/2, Harvard Univ., Cambridge, Mass., and Tyco Laboratories Inc., Waltham, Mass., July 1974.

12. G. F. Hurley: Second Quarterly Tech. Prog. Narrative, Contract No. NAS3-16790, Tyco Laboratories Inc., Waltham, Mass., August 1973.

13. G. F. Hurley: Report No. NASA CR-134808, Tyco Laboratories Inc., Waltham, Mass., April 1975.

14. Noel DeNevers: Fluid Flow, p. 164, Addison-Wesley Pub. Co., Reading, Mass., 1970.

15. R. B. Bird, W. E. Stewart and E. N. Lightfoot: Transport Phenomena, pp. 51-63, John Wiley and Sons, Inc., New York, 1960.

16. B. Chalmers, T. Surek et al.: Progress report No. NSF/RANN/SE/GI-37067X/PR/73/2, Harvard Univ., Cambridge, Mass., and Tyco Laboratories Inc., Waltham, Mass., September 1973.

17. B. Chalmers, H. E. LaBelle, Jr. and A. I. Mlavsky: Jour. of Crys. Growth, 1972, vol. 13/14, p. 84.

18. B. Chalmers, T. Surek et al.: Progress Report No. NSF/RANN/SE/GI-37067X/PR/73/4, Harvard Univ., Cambridge, Mass., and Tyco Laboratories Inc., Waltham, Mass., January 1974.

19. B. Chalmers, H. E. LaBelle, Jr. and A. I. Mlavsky: Mat. Res. Bull., 1971, vol. 6, p. 681.

20. T. Surek and B. Chalmers: Jour. of Crys. Growth, 1975, vol. 29, p. 1.

21. T. Surek: Scripta Metall., 1976, vol. 10, p. 425.

22. T. Surek: To Be Published, Jour. of Appl. Physics.

23. H. G. Bachmann, F. R. Ahmed and W. H. Barnes: Z. Kristall., 1961, vol. 115, p. 110.

24. K. A. Jackson: Liquid Metals and Solidification, p. 174, ASM, Cleveland, Ohio, 1958.

25. Robert C. Weast, ed., CRC Handbook of Chemistry and Physics, 50th ed., p. B-172, The Chemical Rubber Co., Cleveland, Ohio, 1969.

26. Ibid., p. B-264.

27. T. Allersma, R. Hakim, T. N. Kennedy and J. D. Mackenzie: Jour. of Chem. Phys., 1967, vol. 46, p. 154.

28. T. N. Kennedy, R. Hakim and J. D. Mackenzie: Mat. Res. Bull., 1967, vol. 2, p. 193.

29. M. A. Vasilyeva: Growth of Crystals, vol. 1, p. 191, Consultants Bureau Inc., N. Y., 1959.

30. G. J. Janz, A. T. Ward and R. T. Reeves: Technical Report U.S.-AFOSR No. 64-0039, Technical Bulletin Series, Rensselar Polytechnic Institute, Troy, N. Y., July 1974.

31. G. J. Janz: Molten Salts Handbook, p. 80, Acad. Press, N. Y., 1967.

32. G. A. Chadwick: Jour. Inst. of Metals, 1963-64, vol. 92, p. 13.

33. J. D. Hunt and J. P. Chilton: Jour. Inst. of Metals, 1962-63, vol. 91, p. 298.

34. J. D. Hunt: Jour. Inst. of Metals, 1966, vol. 94, p. 125.

VITA

John Harrison Respess was born in Chattanooga, Tennessee on January 9, 1951. He attended elementary schools in that city and was graduated from Brainerd High School in June of 1969. That same month he entered The University of Tennessee at Knoxville, and in August 1973 he received a Bachelor of Science degree in Metallurgical Engineering. In the fall of 1973 he accepted a graduate research assistantship at The University of Tennessee and began study towards a Master's degree. This degree was awarded in August 1976.

The author is a member of Tau Beta Pi, The American Society for Metals and The American Welding Society. Mr. Respess will be employed by the Otis Engineering Corporation after graduation.